

Topology, flat bands and magnetic fields in artificial electronic lattices

Jette J. van den Broeke

Topology, flat bands and
magnetic fields in artificial
electronic lattices

Printing: Proefschriftmaken || www.proefschriftmaken.nl

Cover: The cover is based on various figures presented in this thesis.

ISBN: 978-94-6423-497-8

Topology, flat bands and magnetic fields in artificial electronic lattices

Topologie, vlakke banden en magneetvelden in
kunstmatige elektronische roosters

(met een samenvatting in het Nederlands)

PROEFSCHRIFT

ter verkrijging van de graad van doctor aan de Universiteit
Utrecht op gezag van de rector magnificus, prof. dr. H.R.B.M.
Kummeling, ingevolge het besluit van het college voor
promoties in het openbaar te verdedigen op maandag
1 november 2021 des middags te 12.15 uur

door

Jette Janine van den Broeke

geboren op 13 december 1993
te Gouda

Promotoren: Prof. dr. C. de Morais Smith
Prof. dr. D. Vanmaekelbergh

This thesis was (partly) accomplished with financial support from the European Research Council (Horizon 2020 “FIRSTSTEP”, 692691).
Dit proefschrift werd mede mogelijk gemaakt met financiële steun van de Europese onderzoeksraad (Horizon 2020 “FIRSTSTEP”, 692691).

Contents

	Page
1 Introduction	1
2 General concepts	5
2.1 Artificial lattices	6
2.2 Interesting lattice features	18
2.3 Spin-orbit coupling and magnetic fields	22
3 Edge-dependent topology in Kekulé lattices	27
3.1 Introduction	28
3.2 Lattice realization	29
3.3 Finite size effects	32
3.4 Conclusion	34
Supplementary information	35
4 p Orbital flat band and Dirac cone in the electronic honeycomb lattice	45
4.1 Introduction	46
4.2 Results and discussion	47
4.3 Conclusions	54
4.4 Methods	54
Supplementary information	57
5 Spin-orbit gaps in the s and p orbital bands of an artificial honeycomb lattice	75
5.1 Introduction	76
5.2 The model	78
5.3 Honeycomb structures	81
5.4 Conclusion	85
Supplementary information	87
6 On the influence of electron spin in artificial lattices	91
6.1 Introduction	92
6.2 Magnetic muffin-tin model	93
6.3 Quantum well.	95
6.4 Subtracted spectra	97
6.5 Conclusion	99

Supplementary information 101

7 Conclusion **103**

Backmatter

Bibliography **107**

Samenvatting **117**

List of publications **122**

Acknowledgments **124**

Curriculum Vitae **127**

Introduction

Material science aims to create new compounds with specific features in order to overcome technological challenges. Although many natural materials have convenient properties, they are often "off target" for a certain application. One famous example is graphene, which is very thin, light, flexible, has excellent material strength, and displays a remarkable electronic conductance involving "massless" relativistic electrons [1]. The carbon atoms in graphene form a two-dimensional honeycomb lattice and intrinsic spin-orbit coupling could, in principle, open a topological gap hosting one-dimensional spin-filtered quantum channels at the edge of the crystal. However, in graphene the intrinsic spin orbit-coupling is much too small to observe this highly desired property [2, 3]. Although many attempts have been made to enhance the intrinsic spin-orbit coupling in graphene, like adding heavy atoms [4, 5], the results are not yet conclusive [6].

An alternative method to design systems that fit desired pre-defined requirements is to build an artificial lattice or quantum simulator. In this case, atom-like building blocks are positioned and connected with high precision, in such a way as to obtain the desired properties. This can be achieved in multiple ways, e.g., with cold atom systems [7], photonic systems [8] and acoustic systems [9], each with their own advantages and disadvantages. However, all these systems are not based on electronic excitations and, hence, do not directly simulate the electronic properties of materials.

One way to achieve an artificial electron lattice simulation is by creating artificial lattices that confine electrons. This can be accomplished in multiple ways, for example by coupling quantum dots [10, 11]. Alternatively, one can create a potential pattern in thin semiconductor films on top of two dimensional quantum wells using lithography [12–14]. Although these methods have produced preliminary results and have the potential to be adapted for large scale production, they are not yet very reproducible and precise. This is unfortunate, as designing and measuring with great accuracy is vital to reveal the possibilities of electronic lattices in a convincing way.

More precise artificial electronic lattices can be fabricated by using a scanning tunneling microscope (STM) to manipulate the position of atoms and molecules with atomic precision. The adatoms (or molecules) either repel or attract electrons of a two-dimensional surface gas; in either way electrons are confined in a two dimensional lattice, with a geometry that can be made "on demand". This method was pioneered by Gomes et al. in 2012 [15], using CO molecules on a Cu(111) surface. The Cu(111) surface hosts an effective two dimensional electron gas, on which the CO molecules were placed as scattering elements in a triangular pattern to confine the electrons in a honeycomb lattice. It was later demonstrated that the creation of artificial electron lattices with STM is possible with several different material platforms like chlorine vacancies in a chlorine monolayer on top of Cu(100) [16], and dangling bonds on a H-Si(100) surface [17]. The CO on Cu(111) platform has since been used to investigate square geometries [18], quasi crystal structures [19], and fractal systems [20] in artificial electron lattices. In this thesis, we seek to expand the range of possibilities for this type of artificial lattices and explore (crystalline) topology, flat bands, and magnetic fields in artificial lattices that can be created by atomic manipulation.

Magnetic fields break the time reversal symmetry of a system and can give rise to interesting (topological) phase transitions, such as in the quantum Hall effect [21]. So far, magnetic fields have only been indirectly studied in artificial lattices, by introducing lattice distortions to simulate magnetic effects [15]. Thus, time-reversal broken systems are not yet accessible in artificial lattices, making it impossible to study the topology of the quantum Hall effect in these systems.

Non-trivial topology can be extremely useful, as it provides unique quantum channels at the boundaries of the crystal that are protected by the symmetries of the system. This has led to numerous proposals to use topological materials for the construction of quantum computers [22, 23]. Additionally, a topological gap can lead to the creation of isolated topological flat bands [24]. Isolated flat bands are in general interesting phenomena, as the kinetic energy of the electrons is quenched, making interaction effects the dominant contribution. Such topological flat bands hold promise for new physics and applications due to the non local nature of the topology [25]. Moreover, it has been predicted that an isolated flat band is the driving factor behind unconventional superconductivity, in magic-angle twisted bi-layer graphene [25, 26].

This thesis is structured as follows; in chapter 2, we present the theoretical and experimental concepts underlying the work presented in this thesis. We start with the description of artificial lattices, how they are created, and how their electronic properties can be measured. Next, we investigate several interesting lattice features, like internal degrees of freedom and topology. Finally, we discuss how spin-orbit coupling can be included in the Schrödinger equation by taking the non-relativistic limit of the Dirac equation.

In chapter 3, we study the Kekulé lattice, which is a detuned, "dimerized" version of the honeycomb lattice for which edge states protected by crystalline topology have been predicted. We create four artificial lattices, with different ratios for the weak vs. strong hopping and boundary conditions to explore the topological phase diagram. Experimentally, we observe localized edge modes for the non trivial lattices, in line

with muffin-tin and tight-binding models for the system [27].

In chapter 4, we explore the honeycomb geometry in artificial lattices. We show that by playing with the size of the artificial sites and their coupling, the p orbitals of the system can be brought in the experimentally observable energy window. Additionally, we show that by introducing clusters of CO scatterers, the hopping parameters in the system can be manipulated to obtain a system with separated s and p orbitals and a flat p orbital band [28, 29].

In chapter 5, we include spin-orbit coupling into the muffin-tin framework, and investigate how this influences the electronic bands of the artificial honeycomb lattice. We find that intrinsic spin-orbit coupling opens up gaps both in the s and p orbitals. The gaps are much bigger and more robust to Rashba spin-orbit coupling for the p orbital bands. Investigating this gap further in the finite lattice, we find an in-gap localized state at the edge of the system, indicative of a quantum spin Hall state [30].

Finally, in chapter 6, we theoretically explore the influence of magnetic fields on quantum corrals which are isolated two-dimensional artificial atoms. We find that even with a non spin-polarized STM tip, it should be possible to observe Zeeman effect i.e. the coupling between the spin of the electrons and the magnetic field, in the orbitals of the two-dimensional artificial atom. Additionally, we find that the magnetic field couples to the angular momentum of the circular quantum corral solutions. Surprisingly, a similar effect is visible for square quantum corrals, even though they have no well defined angular momentum.

General concepts

In this chapter we review the fundamental concepts underlying the results presented in this thesis. We start with the concept of artificial lattices. We discuss surface states on metals, how surfaces can be imaged and prepared atom by atom on a metallic surface using scanning tunneling microscopy, explore the concept of artificial atoms and how these can be combined to form lattices. We then discuss the ways we can model artificial lattices. Next, we introduce the concept of topology in lattices, and discuss crystalline topology and the quantum spin Hall effect. Additionally, we investigate how spin-orbit coupling can be used to create isolated flat bands, and their possible applications. Finally, we finish this chapter with the introduction of the Dirac equation and take its non relativistic limit to obtain the Zeeman and spin-orbit corrections to the Schrödinger equation.

2.1 Artificial lattices

In this thesis, we study the possibilities and limits of artificial lattices, specifically electronic lattices build on the Cu(111) surface, by placing CO molecules on dedicated positions on the surface. These artificial electronic lattices are two dimensional, and are based on the principle that the surface state of copper acts as an effective two dimensional electron gas that is scattered by the CO molecules acting as potential barriers. We will therefore start by investigating surface states, with a particular focus on the copper (111) system.

2.1.1 Surface states

At the surface of a material, there is a transition from the band structure of the bulk material to the vacuum. This change in potential at the surface gives rise to surface states, as described for nearly free electrons by Shockley in 1939 [31] and for tightly bound electrons by Tamm in 1932 [32]. As copper is best described from the free electron perspective; we will follow Shockleys approach here.

Shockley found that, for a potential that is only periodic in a finite range, as in Fig. 2.1(a), there are two types of solutions. First there is the bulk solution, that is similar to the fully periodic solution in the infinite material, and decays exponentially into the vacuum, see Fig. 2.1(b). This is the solution we would naturally expect to find. However, he also found another solution, that is localized at the surface and decays exponentially both into the vacuum and into the bulk (Fig. 2.1(c)).

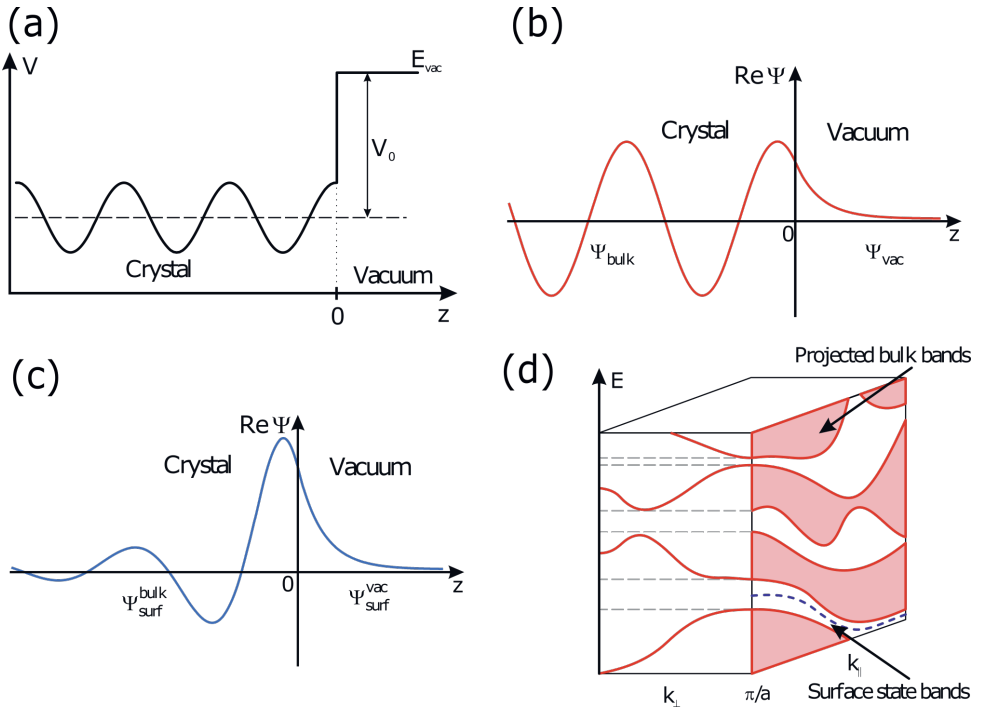


Figure 2.1: Shockley states. (a) A sketch of the potential near the surface. (b), (c) The bulk and surface solution, respectively, to the Schrödinger equation for the potential in (a). (d) Schematic depiction of a Shockley surface state in a three dimensional material. (a-d) are adapted from Ref. [35].

For three dimensional materials, due to in-plane electronic coupling, this solution can become a parabolic surface band, as is the case for Cu(111) around the Fermi energy. Although copper is a metal and does not have a band gap, it does have a (indirect) gap in the band structure projected along the momentum perpendicular to the surface k_{\perp} , that the surface state falls into, as shown schematically in Fig. 2.1(d). It is thus possible to effectively describe the surface state of Cu(111) as a two dimensional electron gas with effective mass $m^* = 0.42m_e$, with m_e the electron mass [33]. There is, however, limited scattering to the bulk due to impurities like step edges, phonon, and electron scattering events, resulting in a broadening of 24 meV [34].

2.1.2 STM measurements

The scanning tunneling microscope (STM) developed by Binnig and Rohrer in 1981 [36, 37] is an extremely useful instrument to measure surface phenomena. In an STM, an atomically sharp tip is positioned close to the surface of interest without making contact. If now a potential difference V is created between the tip and sample, a tunneling current that scales exponentially with the distance between the sample and tip can be observed. For a schematic overview of the STM setup see

Fig. 2.2(a). As STM allows for an extremely precise control of the relative position of the tip and sample using piezo electric elements. This principle can be used to image the surface with atomic resolution. Furthermore, by creating a local potential next to a surface adatom, this adatom can be moved along the surface and positioned with atomic precision.

In more detail, there are three main ways in which the STM can be used. First of all, there is the constant current mode that can be used to observe the height profile of the surface. In this mode, there is a feedback mechanism between the height control and the tunneling current, keeping the current constant by varying the height as the tip moves over the sample. By keeping track of the changes made in the position of the tip, a topographic image of the sample surface can thus be created.

Secondly, one can use the STM to measure the local density of states in the sample. Here, instead of keeping the current steady and varying the tip sample distance, the derivative of the tunneling current with respect to the bias voltage is measured. To understand how this works, we first investigate the tunneling current more closely. As described by Bardeen [38], the tunneling current from a tip with states Ψ_i to a sample with states Ψ_j is given by

$$I_{T \rightarrow S} = \frac{2\pi e}{\hbar} \sum_{i,j} f(E_i) [1 - f(E_j)] |M_{ij}|^2 \delta((E_i - E_j) - eV), \quad (2.1)$$

where e is the electron charge, f is the Fermi-Dirac distribution and E_i, E_j are the energies of the states Ψ_i, Ψ_j , respectively. A schematic overview of the energies in the system is given in Fig. 2.2(b). Tunneling occurs between states at both sides of

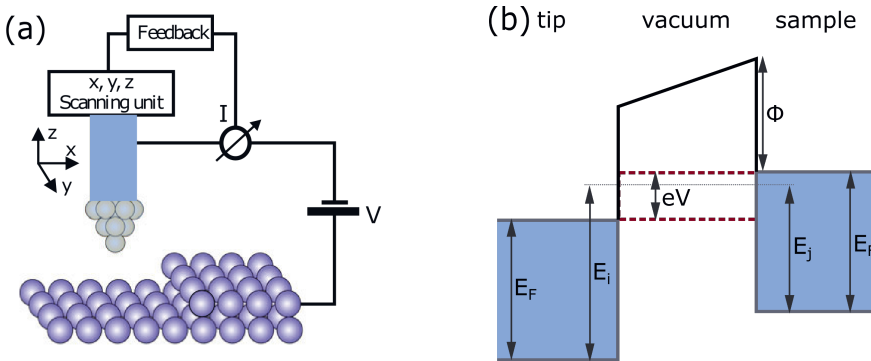


Figure 2.2: STM (a) schematic overview of the STM setup. Adapted from Ref. [35]. (b) Schematic representation of the energies involved in the tunneling problem

the barrier of the same energy. Finally, there are the tunneling matrix elements M_{ij} that describe the coupling between tip and sample and are given by,

$$M_{ij} = \frac{\hbar}{2m} \int (\Psi_j \nabla \Psi_i^* - \Psi_i^* \nabla \Psi_j) \cdot d\mathbf{S}, \quad (2.2)$$

where the integration is over any surface in the vacuum between the sample and tip. The tip used to obtain the results in this thesis is metallic, and its apex can

be approximated as a spherically symmetric s orbital, while the bulk of the tip is neglected. This approximation, in combination with the assumption of low temperatures and small bias voltages, as first done by Tersoff and Hamann [39, 40], leads to a simplified form of M_{ij} and tunneling current I ,

$$I \propto eV \rho_T(E_F) \sum_j |\Psi_j(\mathbf{r})|^2 \delta(E_j - E_F). \quad (2.3)$$

Here, $\rho_T(E_F)$ is the density of states of the tip at the Fermi energy E_F and \mathbf{r} is the position of the tip in the plane of the sample. Although the dependence of the tunneling current on the tip sample distance is not obvious here, we can see that it is indeed exponential by remembering from the previous section that the surface state wave functions squared $|\Psi_j|^2$ scale exponentially with the distance to the surface.

The formula in Eq. 2.3 can be extended to larger bias voltages that are still lower than the work function Φ of both tip and sample to get [41],

$$I \propto \int_{E_F}^{E_F+eV} \rho_T(E - eV) \rho_S(\mathbf{r}, E) dE, \quad (2.4)$$

with $\rho_S(\mathbf{r}, E)$ the local density of state of the sample. Thus, under the assumption of a constant density of states of the tip, we have,

$$\frac{dI}{dV}(V) \propto \rho_S(\mathbf{r}, E_F + eV). \quad (2.5)$$

In order to measure this derivative, a lock-in amplifier is used to modulate the bias voltage with the time t according to

$$V(t) = V_0 + V_{mod} \cos(\omega_{mod}t), \quad (2.6)$$

where V_{mod} , ω_{mod} are the modulation amplitude and frequency, respectively. Thus, the first order Taylor expansion of the current is,

$$I(V) = I(V_0) + \left. \frac{dI}{dV} \right|_{V_0} (V - V_0) = I(V_0) + \left. \frac{dI}{dV} \right|_{V_0} V_{mod} \cos(\omega_{mod}t). \quad (2.7)$$

Thus, for known V_{mod} , all that is left to do is measure the amplitude of the current variation I_{mod} to obtain the local density of states in the sample. A schematic depiction of the measurement is given in Fig. 2.3.

2.1.3 Adatom manipulation

The last use for the STM that we discuss here is the manipulation of adatoms or small molecules on the surface. This was first done by Eigler and Schweizer at IBM in 1989 [42], when they patterned xenon atoms on a substrate of nickel to form the IBM logo. It was later discovered that an atomically precise manipulation process is possible for many combinations of adatoms and surfaces [43–46]. As we will be considering the manipulation of CO molecules on top of the Cu(111) surface in this thesis, we will explore this system in more detail. CO is chemisorbed to the Cu(111) surface with the carbon atom pointing down on top of a surface copper atom [47].

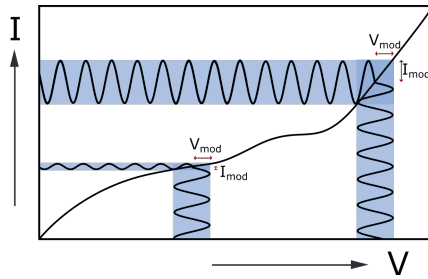


Figure 2.3: Schematic representation of the measurement of the variation in current I_{mod} as a function of bias voltage V .

Although the CO molecules are not mobile below 40 K [48], the position of the molecule can be adapted by using an STM tip, as was first done by Bartels et al. in 1997 [49]. Here, the CO molecule was transferred from the Cu(111) surface to the tip apex, after which the tip was moved to a desired position and the CO was once again placed on the Cu(111) surface. An alternative manipulation technique is to position the STM tip above the molecule, decrease the junction resistance (move the tip closer to the molecule), and then moving the tip sideways to the preferred position, until finally the tip is retracted again [44]. The tip does not break the bond between the CO molecule and the surface, but applies forces on the molecule to drag it along the surface. This lateral manipulation procedure of CO on Cu(111) is used for the results presented in this thesis.

Once adatoms/molecules are on a surface, they affect the surface state. One possible effect is that the adatom attracts electrons of the surrounding state, resulting in an effective potential well. This is for example the case with In adatoms on InAs(111)A [50]. CO on copper is of a different type, it scatters the electrons on the surface. Hence, COs on appropriate positions form a landscape of potential barriers that can define a lattice of artificial atoms sites (see below). In addition, the scattering results in an increased coupling between surface and bulk states. This results in a reduction in the lifetime of the surface electrons, leading to a larger broadening of measured energy peaks. The total broadening is estimated to be around 40-80 meV depending on how many CO molecules there are per surface area [15]. This is in contrast to the 24 meV broadening on pure Cu(111) [34].

On bare Cu(111), the phase coherence length L_ϕ is measured to be around 660 Å at 77 K [51]. The presence of CO molecules reduces the phase coherence length of the surface electrons. Even so, it still allows for the observation of standing wave patterns on the nm scale. This is especially true for the experiments described in this thesis, which were performed at $T = 4\text{K}$.

2.1.4 Quantum corrals

With the option to manipulate individual atoms, came the possibility to make a quantum corral. For this, the adatoms were patterned in the shape of a circle, effectively trapping surface electron waves in a circular quantum well. In 1993, the first quantum corral was created by Crommie et al. [52], who patterned 48 iron atoms

in a ring on the Cu(111) surface, shown in Fig. 2.4(a). Much later, it was shown that it is also possible to build a quantum corral with CO on Cu(111) [53]. In both these experiments, the observed local density of states matches with the analytically known quantum well solutions. For an infinite quantum well, the wave functions $\phi_{n,l}$ and corresponding energies $E_{n,l}$ are given by [54],

$$\phi_{n,l}(\mathbf{r}) \propto J_{|l|}\left(\frac{j_{|l|,n}r}{a}\right)e^{il\theta}, \quad E_{n,l} = \frac{\hbar^2 j_{|l|,n}^2}{2ma^2} \quad (2.8)$$

where $J_{|l|}$ is the $|l|$ th Bessel function, $j_{|l|,n}$ is the n th zero of $J_{|l|}$, and a is the quantum well radius. The first three quantum well solutions, and their corresponding measured quantum corral states are shown in Fig. 2.4(b).

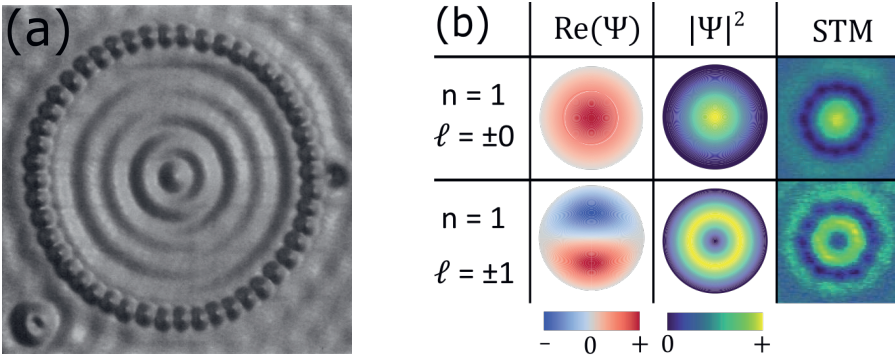


Figure 2.4: The quantum corral. (a) Spatial image of the first quantum corral, adapted from Ref. [52]. (b) comparison of the quantum well solutions (left and middle column) and the local density of states of the corresponding quantum corral states measured using STM (right column), adapted from Ref. [53].

Just like atomic wave functions, quantum well solutions are quantized states with discrete energies. Although the precise radial shape of the wave function is different, both have the same angular symmetry (in two dimensions), and therefore the same degeneracy stemming from the angular part of the wave function. Hence, we will refer to the $(n = 1, l = 0)$ and $(n = 1, l = \pm 1)$ solutions as *s*-type and *p*-type, respectively. The similarity is even more clear when studying the way two quantum corrals behave when they are coupled. In this case, the quantum corrals behave as two artificial atoms to form bonding and anti-bonding states [53].

2.1.5 Building an artificial lattice

Extending the idea of connecting artificial atoms together to form an artificial atomic molecule, we can combine many of these artificial atoms to form a lattice. As the atomic sites need to be electronically coupled, the scatterers are generally not present between the sites. Thus, we get a structure where the scatterers form an anti lattice to the artificial electronic lattice. This was shown for the first time by Gomes et al. [15], who created an artificial version of graphene. As graphene has a honeycomb lattice, a triangular anti-lattice of CO molecules was patterned on top

of the Cu(111) surface state, as shown in Fig. 2.5(a). Indeed, Gomes et al. found a V-shaped density of states, a characteristic signature of a Dirac cone, as shown in Fig. 2.5(b).

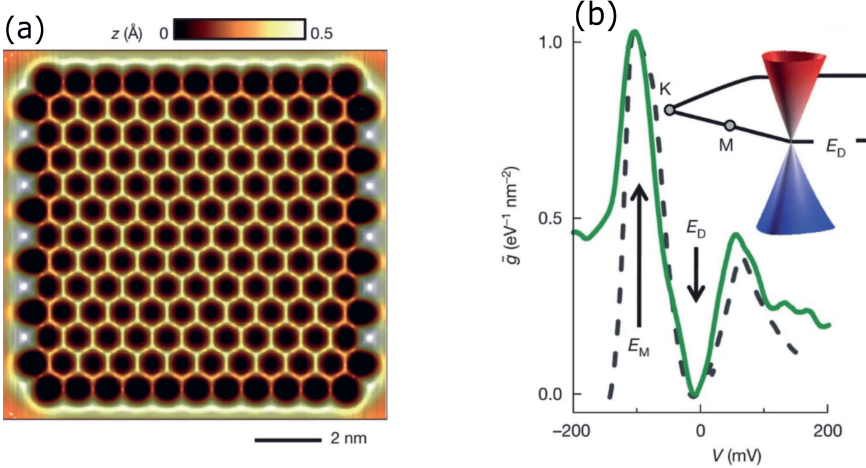


Figure 2.5: Artificial graphene (a) topograph of the artificial lattice. The black spots indicate CO locations. Adapted from Ref. [15]. (b) The green line shows the measured averaged local density of states close to the center of the lattice sites of the artificial graphene. The dotted line indicates the tight-binding prediction. Adapted from Ref. [15].

Although the symmetry of the triangular anti-lattice in the work of Gomes et al. matches the underlying symmetry of the Cu(111) lattice, this does not have to be the case. As shown by Slot et al. [18], it is also possible to create a simple square or Lieb lattice, that does not match the symmetry of the underlying substrate lattice.

2.1.6 Muffin-tin calculations

In order to predict and interpret the experimental results of artificial lattices, it is very useful to build a theoretical model of the system. One valuable tool for this is the muffin-tin model, as first proposed for artificial lattices by Park and Louie [55]. In this framework, the surface state is described as a two dimensional electron gas with an effective mass m^* , and scattering adatoms are incorporated as disk shaped protrusions, with diameter d and height h in the potential V . Thus, a plot of the potential landscape $V(\mathbf{x})$ will look similar to an inverted muffin tin (see Fig. 2.6), to which the model owes its name. Now, we can write down the time-independent two-dimensional one-electron Schrödinger equation for the muffin-tin model,

$$\frac{-\hbar^2}{2m^*} \nabla^2 \Psi + V(\mathbf{x}) \Psi = E \Psi. \quad (2.9)$$

Thus, once we have determined the value of m^* , d and h , all that remains is to solve Eq. 2.9 for the appropriate lattice design. For complicated finite designs, it is not practical to do this analytically. We therefore need to solve the problem numerically.



Figure 2.6: The muffin tin owned by the author of this thesis, turned upside down.

In order to numerically solve Eq. 2.9, we first discretize the system. For a better understanding, we will start with a one dimensional system. Instead of $\Psi(\mathbf{x})$ being a continuous function of \mathbf{x} we now define a n points grid on our system $x_1 \cdots x_n$ defined as $x_{i+1} = x_i + dx$. Thus, the points have a spacing dx between them. The numerical spatial derivative of $\Psi(x_i)$ is then given by

$$\Psi'(x_i) = \frac{\Psi(x_{i+1}) - \Psi(x_{i-1}))}{2dx}. \quad (2.10)$$

Thus, for a system with periodic boundary conditions $\Psi(x_n + dx) = \Psi(x_1)$ we have,

$$\Psi' = \begin{pmatrix} \Psi'(x_1) \\ \Psi'(x_2) \\ \Psi'(x_3) \\ \vdots \\ \Psi'(x_n) \end{pmatrix} = \frac{1}{2dx} \begin{pmatrix} 0 & 1 & 0 & \cdots & -1 \\ -1 & 0 & 1 & \cdots & 0 \\ 0 & -1 & 0 & \cdots & 0 \\ \vdots & \vdots & \vdots & \ddots & \vdots \\ 1 & 0 & 0 & \cdots & 0 \end{pmatrix} \begin{pmatrix} \Psi(x_1) \\ \Psi(x_2) \\ \Psi(x_3) \\ \vdots \\ \Psi(x_n) \end{pmatrix} = \mathbf{D}\Psi, \quad (2.11)$$

where we have defined a derivative matrix \mathbf{D} . Extending to two dimensions, we define a two dimensional grid $\mathbf{x}_{ij} = dx(i\hat{\mathbf{e}}_1 + j\hat{\mathbf{e}}_2)$ using the orthogonal unity vectors $\hat{\mathbf{e}}_1$, $\hat{\mathbf{e}}_2$, and $i, j \in \{1, 2, \dots, n\}$. The derivative in the $\hat{\mathbf{e}}_1$ direction becomes,

$$\Psi' = \begin{pmatrix} \Psi'(x_{11}) \\ \Psi'(x_{21}) \\ \Psi'(x_{31}) \\ \vdots \\ \Psi'(x_{12}) \\ \Psi'(x_{22}) \\ \vdots \end{pmatrix} = \mathbf{I}_n \otimes \mathbf{D} \begin{pmatrix} \Psi(x_{11}) \\ \Psi(x_{21}) \\ \Psi(x_{31}) \\ \vdots \\ \Psi(x_{12}) \\ \Psi(x_{22}) \\ \vdots \end{pmatrix} = \mathbf{D}_1 \Psi, \quad (2.12)$$

where \mathbf{I}_n is the n dimensional identity matrix, and we have defined the derivative in the $\hat{\mathbf{e}}_1$ direction \mathbf{D}_1 . Similarly, we have the derivative in the direction of $\hat{\mathbf{e}}_2$, $\mathbf{D}_2 = \mathbf{D} \otimes \mathbf{I}_n$. Finally, we can define the potential V . We would like the operator V working on our discretized wave function $\Psi(\mathbf{x}_j)$ to give $V(\mathbf{x}_{ij})\Psi(\mathbf{x}_{ij})$. This can be

done by multiplying $V(x_{ij})$ with the n^2 dimensional identity matrix,

$$\mathbf{V} = I_{n^2} \begin{pmatrix} V(x_{11}) \\ V(x_{21}) \\ V(x_{31}) \\ \vdots \\ V(x_{12}) \\ V(x_{22}) \\ \vdots \end{pmatrix}. \quad (2.13)$$

Thus the discrete Hamiltonian is

$$H = \frac{-\hbar^2}{2m^*} (\mathbf{D}_1^2 + \mathbf{D}_2^2) + \mathbf{V}. \quad (2.14)$$

As the Hamiltonian has a second order spatial derivative, we need to apply the derivative matrices \mathbf{D}_1 and \mathbf{D}_2 twice. Hence, the derivative matrices \mathbf{D}_1 and \mathbf{D}_2 have been squared in Eq. 2.14. When studying the artificial lattices of the previous section, Eq. 2.14 can become a very large matrix. Therefore, the eigenvalues are not exactly calculated but instead approximated numerically. Although we are interested in the lowest energy eigenvalues of the system, algorithms used for matrix diagonalization are generally most efficient at calculating the eigenvalues with the highest magnitude. This problem can be solved by using the inverted matrix equation. More precisely, instead of solving the eigenvalue equation $H\Psi = \lambda\Psi$, we can solve $H^{-1}\Psi = \frac{1}{\lambda}\Psi$. In this equation, the largest magnitude eigenvalues correspond to the smallest $|\lambda|$. An additional improvement of the efficiency of the diagonalisation can be made by using the fact that most of the matrix does not contain any information and is zero. These types of matrices are called sparse matrices. The Arnoldi algorithm [56] is specialized for these type of matrices. However, for real symmetric matrices, or Hermitian matrices such as the one in Eq. 2.14, the efficiency can be further improved using the Lanczos algorithm. [57, 58]. For this thesis, the Lanczos algorithm was implemented using the build-in algorithm in the program Mathematica [59] for chapter 3 and 4, and using the Python Scipy package [60] for chapter 5 and 6.

Once the wave functions and energies of the system have been calculated, we would like to compare the results to outcomes of STM measurements. Thus we need to calculate the LDOS. In a system without scattering, the LDOS is given by:

$$LDOS(\mathbf{x}, \epsilon) = \sum_{\epsilon'} |\Psi_{\epsilon'}(\mathbf{x})|^2 \delta(\epsilon - \epsilon'), \quad (2.15)$$

where we have denoted the eigenenergies of the system and their corresponding wave functions as ϵ' and $\Psi_{\epsilon'}(\mathbf{x})$, respectively. However, due to the scattering of electrons in experimental samples, a broadening is introduced in the peaks of the LDOS, and the delta function $\delta(\epsilon - \epsilon')$ in Eq. 2.15 is replaced by a Lorentzian,

$$L(\epsilon - \epsilon') = \frac{b}{(\epsilon - \epsilon')^2 + \left(\frac{b}{2}\right)^2}, \quad (2.16)$$

where b is the broadening.

2.1.7 Periodic muffin-tin

Instead of solving Eq. 2.9 for a finite system, as in the previous section, we will now investigate a periodic system. In this case, we have a periodic potential V and we can calculate the band structure of the system. This technique is very useful to understand the behavior of a finite system, as it allows us to investigate features like band gaps, flat bands and Dirac cones in a much more direct manner.

We first Fourier transform the wave function:

$$\Psi(\mathbf{x}) = \frac{1}{\sqrt{A}} \sum_{\mathbf{k}} e^{i\mathbf{x}\cdot\mathbf{k}} \Psi(\mathbf{k}), \quad (2.17)$$

where the area $A = L^2$, with L the system size in which the wave function is periodic, and $\mathbf{k} = \frac{2\pi}{L}(l_x, l_y)$ and l_i range from $-\infty$ to ∞ . Next, we Fourier transform the potential V ,

$$V(\mathbf{x}) = \sum_{\mathbf{K}} e^{i\mathbf{K}\cdot\mathbf{x}} V_{\mathbf{K}}, \quad (2.18)$$

where \mathbf{K} are the reciprocal lattice vectors. Applying these transformations to Eq. 2.9, the resulting equation also has to hold for a single Fourier component \mathbf{q} ,

$$\frac{\hbar^2}{2m} q^2 \Psi(\mathbf{q}) + \sum_{\mathbf{K}} V_{\mathbf{K}} \Psi(\mathbf{q} - \mathbf{K}) = E_q \Psi(\mathbf{q}). \quad (2.19)$$

As only wave functions of the shape $\Psi(\mathbf{q} - \mathbf{K})$ appear in this equation, we get a system of equations for each \mathbf{q} ,

$$\frac{\hbar^2}{2m} (\mathbf{q} - \mathbf{K}')^2 \Psi(\mathbf{q} - \mathbf{K}') + \sum_{\mathbf{K}} V_{\mathbf{K}-\mathbf{K}'} \Psi(\mathbf{q} - \mathbf{K}) = E_{\mathbf{q}-\mathbf{K}'} \Psi(\mathbf{q} - \mathbf{K}'), \quad (2.20)$$

where we have performed a transformation $\mathbf{K} \rightarrow \mathbf{K} - \mathbf{K}'$ in the second term on the left side of the equation. In principle, Eq. 2.20 defines an infinite set of equations, and can therefore not be solved numerically. However, we are only interested in the lowest bands. If $V_{\mathbf{K}}$ becomes exponentially small for large values of K^2 , we can therefore make a cutoff in the values of \mathbf{K} that we take into account. We can then solve the system of equations for arbitrary \mathbf{q} in the Brillouin zone. In classical muffin-tin calculations, the potential is fully periodic and the Fourier transformed potential is analytically known [61]:

$$V_{\mathbf{K}} = \frac{\pi d}{A |\mathbf{K}|} J_1 \left(|\mathbf{K}| \frac{d}{2} \right) V_0. \quad (2.21)$$

Here, d is the diameter of the muffin-tin potential disks, V_0 is the height of the potentials, and J_1 is the first Bessel function. Indeed, we see that $V_{\mathbf{K}}$ becomes small for large \mathbf{K} .

Thus, we now do not only have the possibility to calculate the wave function maps $\Psi(x, y)$ as in the previous section, but we can now also calculate the energy dispersion of the periodic lattice $E_{\mathbf{q},n}$.

2.1.8 Tight binding

Finally, we would like to compare the results for artificial lattices with their atomic versions. By making this comparison, we can check whether the artificial lattices indeed mimic atomic systems, as expected. For atomic systems, many predictions are made and toy models are investigated, using the tight-binding theory. In this framework, electrons are approximated to be closely bound to the atomic core, and the wave functions for isolated atoms located at each atomic site i are taken as a basis $|\Psi_{il}\rangle$, where l indicates the single-atom orbital. Thus, the time-independent Schrödinger equation becomes,

$$\mathbf{H}|\Psi_{il}\rangle = E|\Psi_{il}\rangle, \quad (2.22)$$

where \mathbf{H} is the full Hamiltonian of the system, and $|\Psi_{il}\rangle$ is a vector in the isolated atomic orbital basis. Thus, we would need to compute and solve the matrix $\langle\Psi_{il}|\mathbf{H}|\Psi_{jk}\rangle = H_{il,jk}$, where i, j, k, l range over all sites and orbitals of the lattice.

Often, the theory is simplified by only considering the non interacting part of the Hamiltonian and setting $H_{il,jk}$ to zero if site i and j are not equal or (next) nearest neighbors. Many of the matrix elements $H_{il,jk}$ are symmetry-related and in a large part independent of the specific material, as a general basis is used. These material independent parts have first been calculated for the lowest couple of orbitals by Slater and Koster [62]. The material-dependent magnitude of the elements is usually fitted to results from other sources, such as experimental measurements or density functional theory calculations.

In the description above, the assumption has been made that $|\Psi_{il}\rangle$ form an orthogonal basis; in other words, we assume that the orbital overlap elements, $s_{ijkl} = \langle\Psi_{il}|\Psi_{jk}\rangle = \delta_{ij}\delta_{lk}$. Although this is true for atomic orbitals on the same site, it is generally not the case for atomic orbitals on different sites. This orbital overlap is often neglected. However, it turns out to be of vital importance when trying to fit artificial lattice results to tight-binding theory. In order to incorporate the orbital overlap correctly, we solve the generalized eigenvalue equation,

$$\mathbf{H}|\Psi_{il}\rangle = E\mathbf{S}|\Psi_{il}\rangle. \quad (2.23)$$

Here, \mathbf{S} is the orbital overlap matrix.

To see how the STM measurements, muffin-tin calculations, and tight-binding calculations discussed in the previous sections compare, we consider results for the Lieb lattice from Ref. [18]. The Lieb lattice has three non equivalent sites in a square unit cell, as shown in Fig. 2.7(a). Thus, a tight-binding band structure of the lattice has three bands if only s orbitals are considered, as shown in Fig. 2.7(b). Here, the corresponding lowest three muffin-tin bands are also displayed. We see that although the two band structures match closely for the first band, the results are less similar for the second two. This is due to the influence of higher energy (p) orbital bands, that are naturally included in the muffin-tin approximation but not in the tight-binding model. For the finite system, a comparison of the local density of states measured using STM and the simulated results using muffin-tin and tight-binding methods is shown in Fig. 2.7(c-e).

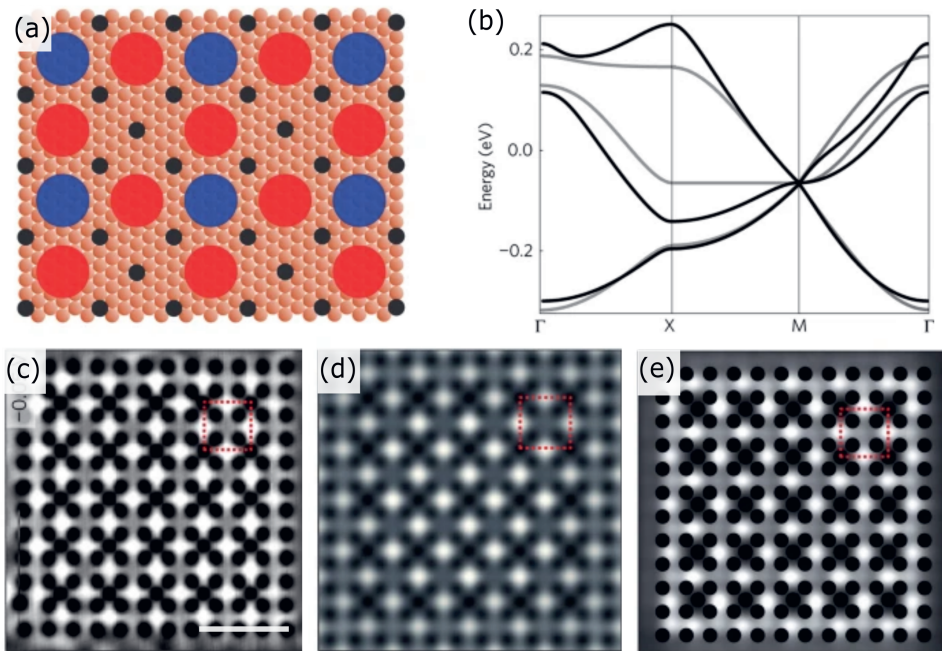


Figure 2.7: The artificial Lieb lattice as build in Ref. [18]. (a) Schematic overview of the locations of the CO molecules (black) on the Cu(111) lattice (brown). The artificial lattice sites are indicated by the red and blue dots. (b) Calculated band structure for the design in (a) using periodic muffin-tin (black) and tight-binding (gray) methods. (c) Differential conductance map at -0.05 V taken above the artificial lattice. (d), (e) Muffin-tin, tight binding simulated local density of states at -0.05 eV. (a-e) are adapted from Ref. [18].

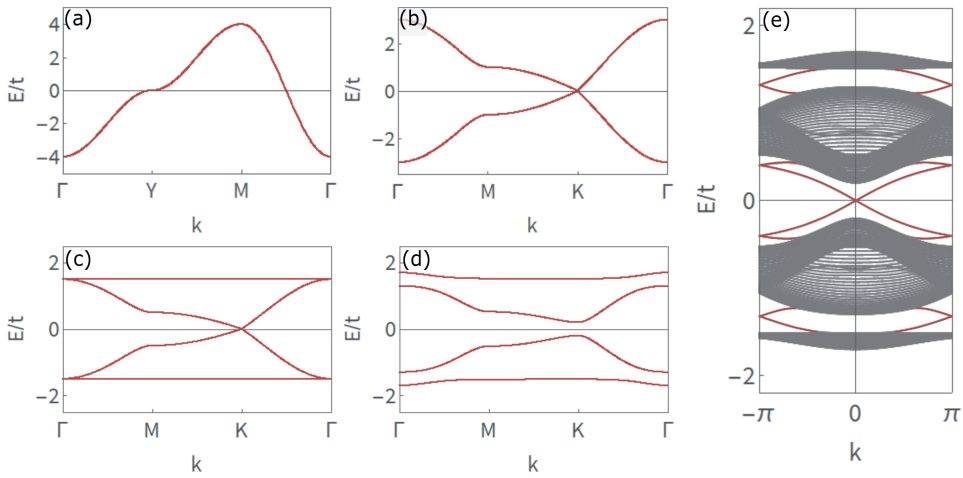


Figure 2.8: Tight-binding band structures with different electronic degrees of freedom. (a) The simple square lattice, with one s orbital at each site. (b), (c) Honeycomb lattice, with two sites in each unit cell, and one s orbital, two p orbitals per site (and no s orbital), respectively. (d) Honeycomb lattice with two p orbitals per site and intrinsic spin-orbit coupling. (e) Same as (d) but in the ribbon geometry, instead of a fully periodic lattice. The edge state dispersion is indicated in red.

2.2 Interesting lattice features

Artificial lattices can mimic many features that are present in atomic systems. The advantage of artificial systems is that several parameters, like onsite energy and hopping can easily be adapted, allowing for detailed studies of many interesting phenomena. In this section we will investigate some of these features, their basic principles, and their possible applications.

2.2.1 Electronic internal degrees of freedom

Besides their location on the lattice, electrons have additional degrees of freedom. One degree of freedom is the spin, and in case of electrons tightly bound to an atom, there is also the orbital degree of freedom. Finally, it can happen that there are multiple sites in the same unit cell, generating a sublattice freedom. If there was only one degree of freedom, there would only be one energy band, as is the case for the spinless tight-binding model of the simple square lattice shown in Fig. 2.8(a). Adding an additional site to each unit cell, we can get a honeycomb band structure with two bands, as for graphene which has two bands, see Fig. 2.8(b). We can then introduce multiple orbitals in the system, like the degenerate p_x , p_y orbitals (here, we ignore the s orbital), which results in one additional band for each orbital, at each site, totaling four bands, as in Fig. 2.8(c). If we next introduce spin to the lattice, this doubles the amount of bands, but if the inversion symmetry is preserved, the bands are degenerate. Relativistic spin-orbit effects result in a band opening at

Γ and K , as can be observed from looking at the fully periodic band structure in Fig. 2.8(d). If we investigate a ribbon geometry, on the other hand, the inversion symmetry is broken at the surface. In this case, spin polarized edge modes appear in the spin-orbit induced band gaps at each edge, see Fig. 2.8(e). It turns out that the appearance of these edge modes is no coincidence, and their presence is guaranteed by the topology of the system.

2.2.2 Topology

Mathematically, topology is the study of properties of geometric objects that are conserved under continuous transformations. This conservation is quantified by so-called topological invariants that can change value only when the object is changed in a non-continuous way. A famous example is the amount of holes in a doughnut. If we continuously transform the shape of the doughnut to, for example, a coffee mug with a handle, the amount of holes will not change. Hence, the number of holes is a topological invariant. In addition to geometrical shapes, it is also possible to define topological invariants for wave functions. These invariants are protected by the band gap and the symmetry of the system, and thus do not change as long as the band gap remains open and symmetries are unbroken [63]. This is especially interesting because of the bulk boundary correspondence, linking the topological invariant to the protection of edge states on the boundary of the topological material. This leads to edge states that are pinned at the middle of the gap (for one dimensional systems), or cannot be gapped (for two and three dimensional systems) as long as the topological invariant is unchanged. As the topology is determined by the crystal structure and/or other bulk properties of the material, this yields a remarkably strong protection.

In one dimension, a well known topological system is the Kitaev chain [64]. In this superconducting system, the particle-hole symmetry can lead to the protection of Majorana boundary modes, that have been predicted to be an ideal building block for quantum computing. Many attempts have been made to experimentally realize these majorana particles. However, the results remain contested [65].

For two-dimensional crystals, the edge states are one-dimensional in-gap edge states with a dispersion, prevented from becoming gapped by the topology of the system. A well known example is the quantum Hall effect. The quantum Hall effect is the quantum version of the classical Hall effect, where a magnetic field perpendicular to a conducting surface gives rise to a voltage difference that is transverse to the current running through the sample. In the quantum Hall effect, the edge modes become quantized, as set by the topology of the bulk, leading to quantized values of the Hall conductivity. This was first measured in 1980 [21] and was in 2018 used to redefine the kilogram in terms of Planck's constant [66].

2.2.3 Quantum spin Hall effect

In the quantum Hall effect there is a magnetic field that breaks time-reversal symmetry. If the time reversal symmetry is preserved, however, a different kind of edge state can appear. Indeed, in the presence of spin-orbit coupling, time-reversal symmetry can give rise to the quantum spin Hall effect.

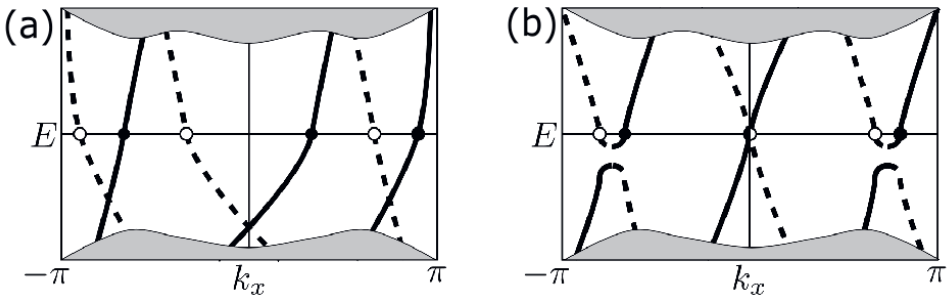


Figure 2.9: Time reversal symmetric edge states (a) three pairs edge states in the bulk gap. (b) Two state pairs have become gapped. (a,b) are adapted from Ref. [63].

The time-reversal operator T reverses the direction of time, giving the transformation $x \rightarrow x$ and $p \rightarrow -p$, and reversing the spin of the electrons. When the Hamiltonian H of a system is time-reversal symmetric, this means that T commutes with the Hamiltonian, $T^{-1}HT = H$. Thus, a state $|\Psi\rangle$ has the same energy as $T|\Psi\rangle$. However, the two states cannot be the same, as they have opposite spin. This effect is known as Kramers degeneracy [67]. In the absence of spin-orbit coupling, Kramers degeneracy is guaranteed by the degeneracy between up and down spins. When spin-orbit coupling is present though, spin degeneracy is not required and the effect becomes non trivial.

If the time-reversal symmetric system is insulating and has an uneven amount of pairs of edge modes (note, this is only possible if spin degeneracy is broken), Kramers degeneracy makes it impossible to continuously remove the edge states without closing the gap. This can most easily be seen by studying the example in Fig. 2.9(a). Here, we see three pairs of edge states in a time-reversal symmetric system. As shown for two of the pairs of edge modes in Fig. 2.9(b), pairs of crossing edge modes can become gapped in a continuous way if their time mirrored variant also becomes gapped. If the pair is its own image under time-reversal symmetry, however, as for the remaining edge mode in Fig. 2.9(b), this is not possible as the gap would need to open up at $k_x=0$, which would violate Kramers degeneracy. Thus, it is not possible to continuously change the band structure in such a way that you go from an odd number of pairs of edge states to an even one or vice versa. Therefore, the parity of the edge modes is protected and the corresponding topological invariant can only have two different values.

Thus, the time-reversal symmetry protects two modes with opposite spin propagating in opposite directions. This so-called spin Hall effect was first proposed by Kane and Mele, who predicted the existence of these states for graphene [2]. Later, Bernevig et al. proposed an alternative realization of the quantum spin Hall effect, this time in HgTe quantum wells [68]. Soon after, the predicted edge state conductance was observed [69].

Unfortunately, the spin-orbit coupling induced gap in graphene turned out to be far too small to allow for the detection of the effect in the graphene system. One way to still detect the quantum spin Hall effect in honeycomb structures is to consider

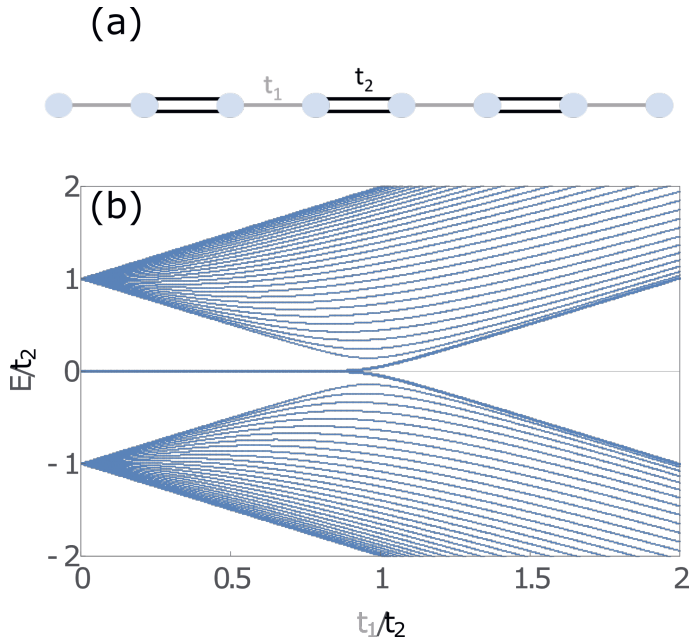


Figure 2.10: SSH chain. (a) Schematic diagram of the SSH chain. The sites are connected through two alternating hopping strengths, t_1 and t_2 . (b) Energies of a 62 site SSH chain as a function of t_1/t_2 .

in-plane p_x and p_y orbitals, as was done for the band structure in Fig. 2.8(d,e). Although these orbitals are not accessible for graphene, they can be highly relevant for artificial lattices, as we will see in chapter 4, and have been shown to exhibit a much larger topological gap than out-of-plane p_z orbitals with the same amount of spin-orbit coupling [24, 70, 71].

2.2.4 Crystalline topology

A different class of topological materials not yet discussed here are crystalline topological insulators. For these materials, the crystalline symmetry protects the topology and edge modes. Although this symmetry is generally easier to break, these systems are also much easier to create, especially in artificial lattices. In order to illustrate the concept of crystalline topology, we present here the best known example, the Su-Schrieffer-Heeger (SSH) chain [72].

The SSH chain is a one dimensional model that has two sites in each unit cell. The sites are either connected through an intra cell hopping, t_1 or through a hopping between unit cells, t_2 , as in Fig. 2.10(a). This lattice has chiral symmetry, meaning that the sites can be divided in two groups A and B , without any connection between sites of the same group. We can thus write the tight-binding Hamiltonian as

$$H = \begin{pmatrix} 0 & T \\ T^\dagger & 0 \end{pmatrix}, \quad (2.24)$$

where T describes the connection between A and B sites. In this form, we can see that for the chiral symmetry operator,

$$C = \begin{pmatrix} 1 & 0 \\ 0 & -1 \end{pmatrix}, \quad (2.25)$$

we have $C^{-1}HC = -H$. Thus, for an eigenstate $|\Psi\rangle$ of H with energy E ,

$$HC|\Psi\rangle = CC^{-1}HC|\Psi\rangle = -CH|\Psi\rangle = -EC|\Psi\rangle. \quad (2.26)$$

Therefore, there is for each eigenstate of H with energy E an eigenstate with energy $-E$, resulting in a symmetric energy spectrum. In case $t_1 \ll t_2$, we have an effective symmetric dimer system, with two isolated sites at the edges of the system, generating two zero-energy states. Surprisingly, even when we move away from the $t_1 \ll t_2$ limit, these states remain pinned at zero, as shown in Fig. 2.10(b). This is due to the chiral symmetry, requiring the edge states to couple in order to move away from zero energy, which is prevented by the spatial separation of the edge modes. Let us now increase t_1 towards t_2 . Once we reach the $t_1 = t_2$ point, the bulk gap closes and the protection of the edge states vanishes, leading to a regime without edge states for $t_1 > t_2$. Thus, we get protected zero modes as a consequence of the chiral symmetry of the lattice. Besides chiral symmetry, there are many other crystal symmetries or combinations of them, that can lead to the protection of edge states, like in the Kekulé lattice, which can have edge states protected by a combination of chiral and mirror symmetry that we will discuss in chapter 3.

2.3 Spin-orbit coupling and magnetic fields

In order to study magnetic fields and spin-orbit coupling in artificial lattices, the muffin-tin framework described in section 2.1 needs to be adapted. As the theory is based on the Schrödinger equation, we will investigate here how the Schrödinger equation can be extended. Integration of these additions to the Schrödinger equation into the muffin-tin framework will be discussed in detail in chapter 6 for the magnetic field and in chapter 5 for the spin-orbit coupling. In order to include the magnetic field into the Schrödinger equation, we will start with investigating the magnetic vector potential.

2.3.1 Magnetic vector potential

The magnetic vector potential, \mathbf{A} , is a vector potential defined such that its curl is equal to the magnetic field \mathbf{B} ,

$$\mathbf{B} = \nabla \times \mathbf{A}. \quad (2.27)$$

\mathbf{A} is not unique. We can transform,

$$\mathbf{A} \rightarrow \mathbf{A} + \nabla f, \quad (2.28)$$

to generate the same magnetic field. Here, f is any continuously differentiable scalar function. This non uniqueness gives a degree of freedom in the system, known as gauge invariance. If we want to fully define \mathbf{A} , it is necessary to choose a gauge.

In the presence of a non-zero magnetic vector potential, the conjugate variable for a particle of mass m to the position, \mathbf{p} is no longer given by $m\mathbf{v}$, with \mathbf{v} the velocity. Instead we have that $\mathbf{p} = m\mathbf{v} + q\mathbf{A}$, with q the charge of the particle. However, the Hamiltonian of the system is the same as the one for a particle without a magnetic field $H = \frac{1}{2}m\mathbf{v}^2 + V$, with V the potential energy. If we still want to write the Hamiltonian in terms of \mathbf{p} , it becomes,

$$H = \frac{1}{2}(\mathbf{p} - q\mathbf{A})^2 + qV. \quad (2.29)$$

Thus, we have effectively done a transformation:

$$\mathbf{p} \rightarrow \mathbf{p} - q\mathbf{A}. \quad (2.30)$$

2.3.2 From Schrödinger to Dirac

Although we have now incorporated a magnetic field into the Hamiltonian, we still do not have any spin dependent terms. This is unfortunate, as we would expect a strong enough magnetic field to couple to the spin of the electron. We therefore turn to a full relativistic description, where the inclusion of spin-dependent terms appear naturally. In the Schrödinger equation, time and space derivatives appear in different orders:

$$i\hbar\partial_t\Psi = H_0\Psi = \left(\frac{-\hbar^2}{2m}\nabla^2 + V\right)\Psi, \quad (2.31)$$

where we have shortened $V(\mathbf{x})$ to V for notation simplicity and defined H_0 . The asymmetry in derivatives is a problem, as we turn to relativistic physics where space and time are treated as a whole. We therefore need the space and time derivatives to appear with the same order to make the equation relativistic.

A good starting point for this relativistic approach is the relativistic energy equation,

$$E^2 = \mathbf{p}^2 c^2 + m^2 c^4. \quad (2.32)$$

Following the same structure as the Schrödinger equation, this would give,

$$-\hbar^2\partial_t^2\Psi = -\hbar^2 c^2\nabla^2\Psi + m^2 c^4\Psi. \quad (2.33)$$

This equation is known as the Klein Gordon equation [73, 74]. It is second order in both time and space. Therefore, a wave function at a set time does not fully define the future of the system. An even bigger problem with this equation is that it can give negative probabilities.

These problems were first solved by Dirac in 1928 [75]. He found a way to factorize the Klein Gordon equation, to get an equation linear in both space and time. For this, one needs to find α and β such that

$$\mathbf{p}^2 c^2 + m^2 c^4 = (\alpha_j p_j c + \beta m c^2)^2, \quad (2.34)$$

where a summation over the three spatial components j is implied. Thus, we get

$$\alpha_j^2 = \beta^2 = 1, \alpha_i \alpha_j + \alpha_j \alpha_i = 0 \text{ and } \beta \alpha_j + \alpha_j \beta = 0. \quad (2.35)$$

These equations only have a solution if α_j and β are at least four by four matrices:

$$\alpha_j = \begin{pmatrix} 0 & \sigma_j \\ \sigma_j & 0 \end{pmatrix}, \beta = \begin{pmatrix} I & 0 \\ 0 & -I \end{pmatrix}. \quad (2.36)$$

Here, I is the two by two identity matrix and σ_j are the Pauli matrices. Using these, we get the Dirac equation

$$i\hbar\partial_t\Psi = c\boldsymbol{\alpha}\mathbf{p}\Psi + \beta mc^2\Psi. \quad (2.37)$$

Here, we indeed have a linear equation in both time and space that is consistent with Eq. 2.33, as desired. However, Ψ is now a four component vector, although we would have expected at most two components, one for spin up, and one for spin down. Additionally, this equation gives negative energy solutions.

The most conventional explanation of this phenomenon interprets the four vector as consisting of both an electron, and a positron. According to hole theory, the negative energy states coming from the Dirac equation are almost all filled creating a Dirac sea. The positron is then a hole in the otherwise filled sea of negative energy states.

2.3.3 Relativistic correction to the Schrödinger equation

In non-relativistic physics, we generally do not encounter any positrons. Indeed, if we go to the non-relativistic limit, we can bring back the purely electron image. However, to get the full picture, we first add the magnetic vector potential: $\mathbf{p} \rightarrow \mathbf{p} - q\mathbf{A}$ and add the potential energy V to the relativistic Dirac equation 2.37. Additionally, we use a separation of variables to go to the time-independent Dirac equation with ε the energy,

$$\varepsilon\Psi = c\boldsymbol{\alpha}(\mathbf{p} - q\mathbf{A})\Psi + \beta mc^2\Psi + V\Psi. \quad (2.38)$$

We can now split the above equation in two parts by writing $\Psi = \begin{pmatrix} \Psi_e \\ \Psi_h \end{pmatrix}$ and using Eq. 2.36 to get,

$$\varepsilon\Psi_e = c\boldsymbol{\sigma}(\mathbf{p} - q\mathbf{A})\Psi_h + mc^2\Psi_e + V\Psi_e, \quad (2.39)$$

$$\varepsilon\Psi_h = c\boldsymbol{\sigma}(\mathbf{p} - q\mathbf{A})\Psi_e - mc^2\Psi_h + V\Psi_h. \quad (2.40)$$

In the non relativistic case, we have that $\varepsilon - V \approx mc^2$. Using this in Eq. 2.40, we get

$$2mc^2\Psi_h = c\boldsymbol{\sigma}(\mathbf{p} - q\mathbf{A})\Psi_e. \quad (2.41)$$

Substituting this into Eq. 2.39, we obtain

$$(\varepsilon - mc^2)\Psi_e = \frac{1}{2m} (\boldsymbol{\sigma}(\mathbf{p} - q\mathbf{A}))^2 \Psi_e + V\Psi_e, \quad (2.42)$$

which is the Pauli equation [76]. In order to state this in a more recognizable form, we can first define $\varepsilon - mc^2 = E$, with E the non relativistic energy. Next, we use that $(\boldsymbol{\sigma} \cdot \mathbf{u})(\boldsymbol{\sigma} \cdot \mathbf{v}) = \mathbf{u} \cdot \mathbf{v} + i\boldsymbol{\sigma}(\mathbf{u} \times \mathbf{v})$ to write

$$E\Psi_e = \frac{1}{2m} \left[(\mathbf{p} - q\mathbf{A})^2 - q\hbar\boldsymbol{\sigma} \cdot \mathbf{B} \right] \Psi_e + V\Psi_e, \quad (2.43)$$

where \mathbf{A} and \mathbf{B} are related through Eq. 2.27. It is important to note here that the cross product of $(\mathbf{p} - q\mathbf{A})$ with itself is non zero due to the operator character of \mathbf{p} .

In Eq. 2.43, we have recovered the Schrödinger equation with a magnetic field, and a coupling between the magnetic field and the spin of the electron. Unfortunately, there still is no coupling between the spin and orbital momentum of the electron. In order to obtain this contribution, we need to do a more precise calculation. For simplicity, we will not consider the magnetic field contribution here, and set $\mathbf{A} = 0$.

We again start with Eq. 2.40, where we have rearranged the terms and used that $\varepsilon = E + mc^2$,

$$\Psi_h = \frac{1}{2mc^2 + E - V} c\boldsymbol{\sigma}\mathbf{p}\Psi_e. \quad (2.44)$$

Now, instead of doing the zeroth order approximation that $2mc^2 + E - V \approx 2mc^2$ we will do a first order Taylor approximation in $E - V$,

$$\frac{1}{2mc^2 + E - V} \approx \frac{1}{2mc^2} \left(1 - \frac{E - V}{2mc^2}\right). \quad (2.45)$$

Using this in Eq. 2.44 and substituting into Eq. 2.39, we obtain

$$E\Psi_e = \boldsymbol{\sigma}\mathbf{p} \frac{1}{2m} \left(1 - \frac{E - V}{2mc^2}\right) \boldsymbol{\sigma}\mathbf{p}\Psi_e + V\Psi_e. \quad (2.46)$$

As \mathbf{p} and V do not commute, $[\mathbf{p}, V] = -i\hbar\nabla V$, we get

$$E\Psi_e = \frac{1}{2m} \left(1 - \frac{E - V}{2mc^2}\right) (\boldsymbol{\sigma} \cdot \mathbf{p})^2 \Psi_e - \frac{i\hbar}{4m^2c^2} (\boldsymbol{\sigma} \cdot \nabla V) (\boldsymbol{\sigma} \cdot \mathbf{p}) \Psi_e + V\Psi_e. \quad (2.47)$$

Finally, we use that $E - V \approx E_{\text{kin}} = \frac{\mathbf{p}^2}{2m}$ to write,

$$E\Psi_e = H_0\Psi_e + \frac{\mathbf{p}^4}{8m^3c^2}\Psi_e - \frac{i\hbar}{4m^2c^2} (\nabla V \cdot \mathbf{p} + i\boldsymbol{\sigma}(\nabla V \times \mathbf{p})) \Psi_e, \quad (2.48)$$

where H_0 is the Hamiltonian from Eq. 2.31. Here, we see three additional terms. The first one $\frac{\mathbf{p}^4}{8m^3c^2}\Psi_e$ is the first relativistic correction to the kinetic energy. The second term $-\frac{i\hbar}{4m^2c^2} (\nabla V \cdot \mathbf{p}) \Psi_e$ is the Darwin term. The last term $-\frac{i\hbar}{4m^2c^2} (i\boldsymbol{\sigma}(\nabla V \times \mathbf{p})) \Psi_e$ is the spin-orbit coupling.

2.3.4 Spin-orbit coupling

Spin-orbit interaction is the coupling between the spin of a particle and its motion in a potential V . If V is spherically symmetric, as for single atom systems,

$$\nabla V = \frac{\partial V}{\partial r} \hat{\mathbf{r}} = \frac{1}{r} \frac{\partial V}{\partial r} \mathbf{r}, \quad (2.49)$$

where r is the radial coordinate. Thus, we get for the spin-orbit coupling H_{SO} ,

$$H_{SO} = \frac{\hbar}{4m^2c^2} (\nabla V \times \mathbf{p}) \boldsymbol{\sigma} = \frac{\hbar}{4m^2c^2} \frac{1}{r} \frac{\partial V}{\partial r} (\mathbf{r} \times \mathbf{p}) \boldsymbol{\sigma} \propto \mathbf{S} \cdot \mathbf{L}, \quad (2.50)$$

where S and L are the spin and angular momentum operators respectively. H_{SO} is highly relevant to understand the energy spectra of individual atoms, as it can give significant shifts in energy levels. This effect is usually referred to as intrinsic spin-orbit coupling.

For larger systems, the potential is generally not spherically symmetric and incorporation of spin-orbit coupling is more complicated. One often used approach to calculate the effect of spin-orbit coupling in crystals is to include the effects into a tight-binding approximation [2, 77]. Although this works relatively well to understand the qualitative effect of spin-orbit coupling, quantities such as gap sizes are difficult to estimate and have to be obtained through fitting to other results. Alternatively, in density-functional theory, the interacting many body ground state can often be accurately approximated with inclusion of the spin-orbit term [78]. Unfortunately, density functional theory is not very well suited for quick calculations with relatively large systems such as the artificial lattices described in this thesis.

Edge-dependent topology in Kekulé lattices

This chapter is based on the following publication:

S. E. Freeney*, J. J. van den Broeke*, A. J. J. H. van der Veen, I Swart & C. Morais Smith, *Edge-dependent topology in Kekulé lattices*, **Physical Review Letters**, vol. 124, no. 23 (2020)

*Both authors contributed equally, S. E. Freeney performed the experiments and J. J. van den Broeke did the theoretical calculations.

The boundary states of topological insulators are thought not to depend on the precise atomic structure of the boundary. A recent theoretical study showed that for topological crystalline insulators with given bond strengths, topological states should only emerge for certain edge geometries. We experimentally probe this effect by creating artificial Kekulé lattices with different atomically well-defined edge geometries and hopping ratios in a scanning tunneling microscope. Topological edge modes are found to only appear for specific combinations of edge geometry and hopping ratio.

3.1 Introduction

A common assumption concerning topological states of matter is that their existence should be insensitive to any detail, except the topology of the bands. This is indeed the case for the quantum Hall [79–81] and quantum spin Hall [2, 68, 69] effects, which are triggered by a magnetic field and strong spin-orbit coupling, respectively. However, theory predicts that the edges of topological crystalline insulators are important [82, 83]. The reason is that the topological invariant depends on the choice of unit cell, which also determines the edge geometry. To establish the relation between edge geometry and the existence of protected boundary states in topological crystalline insulators experimentally, it is essential to work with systems that have atomically precise edges.

Electrons in engineered potentials can be used to study the electronic properties of a large variety of systems [15, 18–20, 84]. Importantly, it is possible to control the hopping strength between different sites [15, 85]. Vacancies in a chlorine monolayer on Cu(100) have been coupled together to realize topologically non-trivial domain-wall states in 1D Su Schrieffer Heeger (SSH) chains [16]. In addition, the manipulation of Fe atoms on the superconducting Re(0001) surface led to a topological superconductor [86, 87]. Recently, the carbon-monoxide (CO) on Cu(111) platform was used to create a so-called higher-order topological insulator [88]. This platform is therefore ideally suited to experimentally address the relation between the geometric structure of topological crystalline insulators and the emergence of non-trivial states.

We investigate this relation by focusing on the Kekulé lattice, see Fig. 3.1. The lattice consists of a triangular array of hexagonal molecules with intra-hexagon bond strength t_0 (light blue lines), connected to each other by bonds of strength t_1 (navy lines). Gapless edge modes appear when the edge is connected only via weak bonds

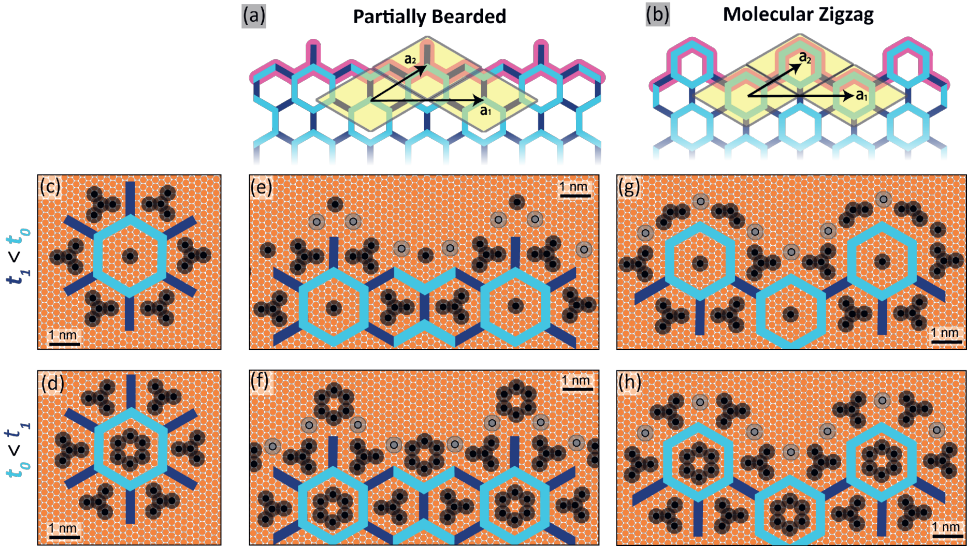


Figure 3.1: (a) and (b) give the geometries of the partially bearded and molecular zigzag edges. The light blue and navy lines indicate the intra- and inter-hexagon hopping parameters, respectively. The edges are highlighted in pink. The unit cell is defined by one yellow rhombus. \mathbf{a}_1 , \mathbf{a}_2 indicate lattice vectors. The edge is formed by translation along \mathbf{a}_1 . (c) and (d) depict configurations of CO molecules that lead to hopping regimes $t_1 < t_0$ and $t_0 < t_1$, respectively. (e-h) show the configurations of CO molecules to realize the partially bearded and molecular zigzag edges in both hopping regimes. The gray circles represent additional CO molecules that reduce the interactions with the surrounding 2D electron gas.

to the rest of the lattice. This topological crystalline system is protected by sublattice and mirror symmetry [89, 90].

Here, we experimentally show that the same Kekulé structure may be trivial or topological, depending on the termination of the sample. The experimental observations are corroborated by theoretical calculations using muffin-tin and tight-binding approaches for the specific experimental realization, as well as investigations of the underlying crystalline symmetries protecting the topological phase.

3.2 Lattice realization

To experimentally realize Kekulé lattices with atomically well-defined edges, we pattern the surface of a Cu(111) crystal with CO molecules, such that the surface state electrons form the desired structure [15]. All experiments were performed using a commercially available Scienta Omicron low temperature Scanning Tunneling Microscope (STM). Details of the procedures are given in the supplemental material, see also [18, 20, 88].

We generate finite lattices with two different hopping parameter ratios and two different edge terminations (bearded and molecular zigzag [89]). The geometry of the lattices is shown in Fig. 1(a) and Fig. 1(b). The leftmost column in Fig. 3.1

shows the precise positioning of the CO molecules on Cu(111) for a single Kekulé unit cell. Our designs are adjusted compared to those in Refs. [15, 91] to minimize next-nearest neighbor hopping and to reduce building complexity. For $t_0 < t_1$, the repulsive potential introduced by the central six CO molecules diminishes the strength of t_0 (light blue). In contrast, for $t_1 < t_0$, there is less repulsion about the single central scatterer. Additionally, for $t_0 < t_1$, each triangularly shaped collection of four CO molecules reduces the bond strength between hexagons. For the $t_1 < t_0$ case, these tetramers are rotated by 60° . This allows for a stronger t_0 , while simultaneously impinging on the connection between hexagons, decreasing t_1 . We built triangular lattices to have the same edge geometry on all sides. Symmetry is locally preserved at the edges, including at the corners, where there is local resemblance to the edges. Interactions with the surrounding 2D electron gas were minimized by adding additional CO molecules, see supplemental material.

To verify that the configuration of CO molecules leads to the appropriate hopping regime, and to find the hopping parameters, the band structures calculated within the tight-binding were matched to those calculated using the muffin-tin method [18, 20, 88]. Besides the hopping parameters t_0 and t_1 , orbital overlap and next-nearest neighbor (NNN) hopping were included in the tight-binding model. Detailed information is given in the supplemental material. We find $t_1 = 0.7t_0$ and $t_0 = 0.67t_1$ for the configurations shown in Fig. 3.1(c) and 3.1(d), respectively. This confirms that the designs result in the desired parameter regime.

Although the orbital overlap deforms the band structure and is therefore of vital importance to understand the experimental results, it was numerically verified that it does not break the topological protection of the edge states in the Kekulé lattice. The NNN hopping however, breaks chiral symmetry. It was found that most NNN hopping parameters were small ($\leq 0.02 t_0$) due to the clustered CO structure. Only the NNN hopping within the hexagon for the $t_1 < t_0$ design ($0.2t_0$) is larger, as there is only one CO in the middle of the hexagons. Therefore, we expect that the chiral symmetry is weakly perturbed for that case.

Two different types of termination have been investigated for each lattice: the partially bearded edge and the molecular zigzag edge [89]. Fig. 3.1 shows both their geometric structure, as well as the configuration of CO molecules needed to realize these edges in both parameter regimes.

Two lattices with $t_1 < t_0$ are shown in Fig. 3.2(a) and Fig. 3.2(b). They have the same bulk but are terminated with a partially bearded and molecular zigzag edge, respectively. Differential conductance spectra of bulk and edge sites of both lattices are shown in the middle panels of Fig. 3.2(a) and Fig. 3.2(b) (locations indicated by the colored dots in Fig. 3.2(a) and Fig. 3.2(b)). The spectra of bulk and edge sites of the molecular-zigzag terminated lattice are similar, *c.f.* black and blue curves in the middle panel of Fig. 3.2(b). In contrast, the local density of states (LDOS) of bulk and edges sites of the lattice with the partially bearded edge are markedly different. The spectrum of bulk sites (indicated in black) shows two peaks associated with the valence (at $V = -0.15$ V) and conduction bands ($V = 0.05$ V), separated by a gap. In contrast, the spectrum of the edge site (indicated in red) shows a large peak positioned at the energy of the bulk gap. The experimentally observed features are reproduced in the tight-binding (lower curves in the middle panels of Fig. 3.2(a)

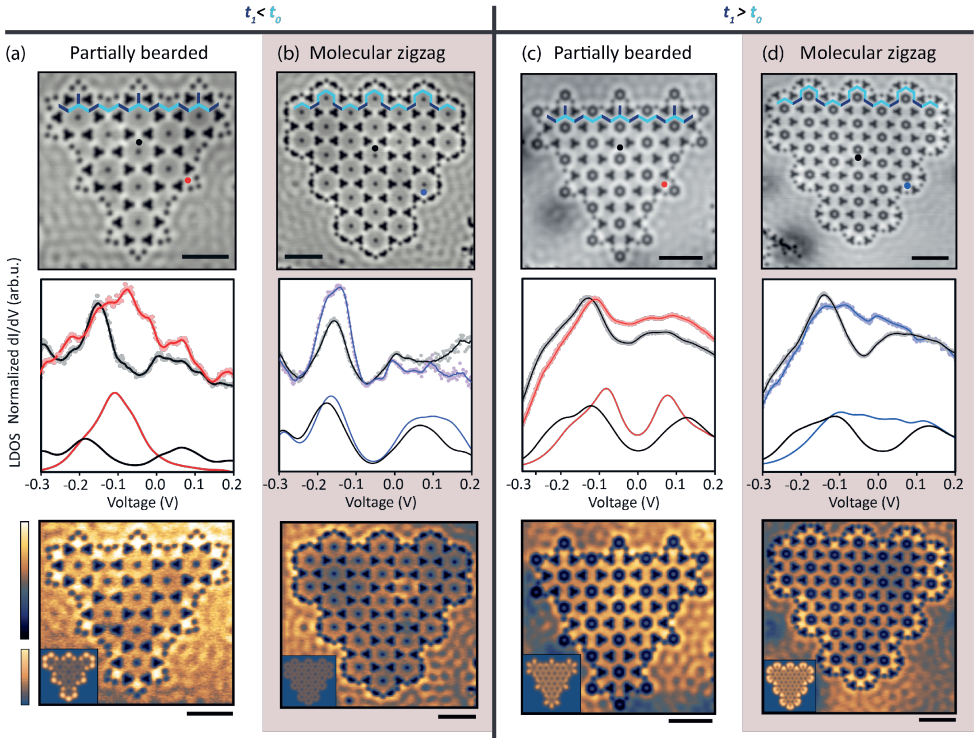


Figure 3.2: (a) Top: STM topograph of a Kekulé lattice with partially bearded edges and in the $t_1 < t_0$ regime ($V_{gap} = 100$ mV, $I_{set} = 10$ pA). Navy and light blue colors indicate bonds as depicted in Fig. 3.1. Middle: experimental differential conductance spectra acquired at bulk (black) and edge (red) sites, normalized by spectra taken on Cu(111). Positions where spectra were acquired are indicated by colored dots in the top panel. The bottom curves depict the LDOS calculated using tight-binding. The bottom panel shows a differential conductance map acquired at a voltage close to the middle of the bulk gap ($V = -65$ mV). The inset shows the tight-binding LDOS map. (b) same as (a), but now for a lattice with a molecular zigzag edge. Settings for the topograph: $V_{gap} = 100$ mV, $I_{set} = 100$ pA. (c) and (d) are the same as (a) and (b) but now for the opposite regime of hopping parameters, *i.e.* $t_1 > t_0$. Scan parameters for the topographs in (c) and (d): $V_{gap} = 100$ mV and $I_{set} = 30$ pA. Differential conductance maps were acquired at -20 mV and the LDOS was calculated at -20 meV. Scale bars (black) are 5 nm.

and Fig. 3.2(b)) and muffin-tin simulations, see supplemental material. For the calculated LDOS, a broadening of 80 meV was added to account for the coupling between surface and bulk states [18, 20, 29, 88].

The spatial extent of the in-gap state is probed by taking differential conductance maps at energies corresponding to the middle of the gap (approximately the onsite energy of the system). By comparing the maps, shown in the bottom panels of Fig. 3.2(a) and Fig. 3.2(b), it is immediately clear that the bearded edge features a well-defined edge localized mode, whereas the lattice with molecular zigzag

edges in the same hopping regime does not. Again, the experimental features are reproduced in the simulations, see the insets in the bottom panels of Fig. 3.2(a) and Fig. 3.2(b). This edge localized state is robust with respect to the introduction of defects, see supplemental material.

These results support the theoretical prediction based on calculation of the topological invariant (the mirror winding number) [89] that the edge mode at the partially bearded edge is topological when $t_1 < t_0$.

The situation is reversed when the hopping strengths are inverted. Fig. 3.2(c),(d) show topographs and LDOS spectra for the Kekulé lattice in the opposite regime of hopping parameters, $t_0 < t_1$. In this case, for the partially bearded edge lattice (Fig. 3.2(c)), the experimental spectra at different edge positions match the behavior of the spectrum in the bulk of the crystal (Fig. 3.2(c), middle panel): there is a dip in the experimentally measured LDOS around $V = -20$ mV for all positions, implying trivially insulating behavior throughout. At the molecular zigzag edge (Fig. 3.2(d)) for the same $t_0 < t_1$ case, there is a markedly higher LDOS at the edge positions at energies corresponding to the bulk gap (Fig. 3.2(d), middle panel). The differential conductance maps confirm that for this parameter regime, the molecular zigzag terminated lattice features a topological edge mode. The theoretical spectra and maps agree with the experimental data, see inset in Fig. 3.2(d).

From these results, we conclude that non-trivial edge modes in topological crystalline insulators in a given regime of hopping parameters only emerge for specific edge geometries. The topological protection occurs at the Γ point and remains robust as long as the bulk states do not mix with the edge states in the middle of the bulk gap. Our experimental broadening is small enough that we do not expect it to influence the topological protection.

3.3 Finite size effects

Finally, we turn our attention to finite-size effects. We first study how edge states are protected in the ribbon geometry, and then investigate how these features change for the finite structures built experimentally. Kariyado et al. [89] found that the mirror winding number protects the zero energy crossing of the edge modes in the Kekulé system. The calculation of this invariant requires both reflection symmetry M_y (the mirror plane intersects the middle of the unit cell and is perpendicular to the edge) and chiral symmetry. Therefore, both symmetries need to be present to protect the edge states. This has been confirmed by Noh et al. [90] by numerically adding perturbations to the Hamiltonian. In case of armchair terminated Kekulé lattices, the M_y symmetry is broken and the edge modes become gapped.

When a system can be divided in two subsystems that only couple to each other and never to themselves, the system possesses chiral symmetry. The chiral symmetry leads to a spectrum that is symmetric around zero energy. This means that zero modes can only move away from zero energy in pairs. If there are more sites of one subsystem than of the other on the edge, but not in the rest of the structure, this can result in zero modes on the edge, as in graphene ribbons with a zigzag termination [92, 93]. The edge geometry considered here contains equally many sites of each sublattice. Thus, chiral symmetry alone does not enforce the existence

of edge states. To understand the protection of zero modes in the system, we should therefore also consider the reflection symmetry M_y . At the Γ point in the Brillouin zone, M_y commutes with the Hamiltonian. Hence, the Hamiltonian needs to have the same eigenstates as M_y , and states which are even and odd under M_y cannot mix. This mechanism prevents two zero modes on the edge of a Kekulé ribbon to mix, thus pinning them at zero energy due to the chiral symmetry.

The Kekulé lattices realized here have (approximate) chiral symmetry, since the NNN hopping is small. The M_y symmetry is preserved locally. In the experimental designs, the lattice sites are locally affected by the same environment as they would be in an infinitely long ribbon, as illustrated in Fig. 3.3(a). However, the global mirror symmetry present in the ribbon is broken in the finite lattice: the boundary is not fully periodic due to modulations to form the corner. Moreover, the lattice is relatively small; thus the momenta are not continuous and a state with zero momentum (the Γ point) does not need to exist. By performing tight binding calculations on finite molecular zigzag terminated lattices, we determine the evolution of the energy levels upon tuning the ratio t_0/t_1 . Fig. 3.3(b) shows this for a lattice with the same size as the experimental system. The in-gap energy levels obtained for a fixed ratio of t_0/t_1 are continuous lines for infinite systems, but become discrete dotted lines (coarse-grained) for finite sized systems. The smaller the system, the larger the distance between the dots. Nevertheless, the spreading and the number of edge states do not change with the size of the system as shown in the supplemental material. Due to hybridization of the edge modes in this finite size system, the edge modes move away from zero energy before the phase transition at $t_0 = t_1$. For larger systems, the edge modes remain close to zero energy for a longer parameter range, as shown in the supplemental material. Note that since the edge states here

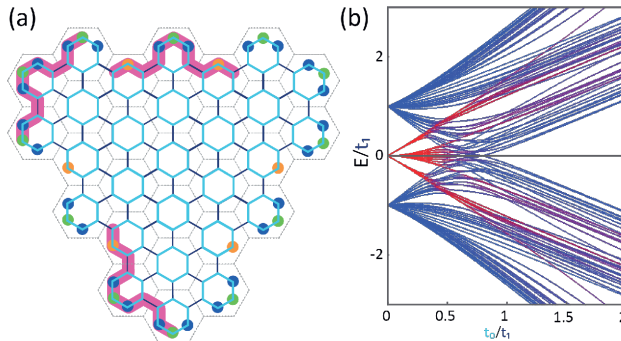


Figure 3.3: (a) Illustration of the finite molecular-zigzag terminated lattice. Green represents protruding sites that couple weakly to two blue sites, orange represents sites sitting in a “cove” at the edge of the lattice. The sections shown in pink have the same local environment. (b) Energy spectrum as a function of t_0/t_1 . The spectrum is shown for the system size used in the experiments with 28 hexagons in total. The coloring of the points signifies the localization of the states. Fully edge localized states appear red, bulk localized states appear blue. The color value was determined for each point by summing over the tight binding wave function edge (bulk) components squared to get the red (blue) contribution.

are dispersive, they span the entire bulk band gap.

3.4 Conclusion

In conclusion, by studying Kekulé lattices with two different bulk structures and two types of edge termination, we investigated the influence of the boundary shape on the existence of non-trivial edge modes in topological crystalline insulators. We found that for the same bulk, the existence of non-trivial edge modes depends on the termination of the sample.

The detection of 1D edge modes in this finite-size 2D system is remarkable. In translational invariant ribbons, the mirror and chiral symmetries pin the edge modes to zero energy at the Γ point in the Brillouin zone. However, here we investigate a finite and relatively small system, without translational symmetry and for which a Brillouin zone cannot be defined. Furthermore, in the $t_1 < t_0$ regime chiral symmetry is not strictly enforced due to a non-zero NNN hopping, and the mirror symmetry is not globally preserved. This suggests that the edge modes are remarkably robust to weak symmetry breaking and finite-size effects. Finally, this work highlights the potential of using artificial lattices to study topological states of matter.

Supplementary information

Experimental methods

Atomic manipulation, scanning tunnelling microscopy and spectroscopy were performed using a commercially available Scienta Omicron LT-STM. A Cu(111) surface was prepared to atomic flatness by repeated cycles of sputtering with Ar⁺ and annealing at approximately 550°C. Carbon monoxide was then deposited onto the Cu(111) surface within the cooled microscope head at a pressure of 1.3×10^{-8} mbar for 1 minute to achieve a coverage of roughly 0.5 CO molecules per nm². Following this, the microscope head was kept at constant UHV (in the range of 10-11 mbar) and at a temperature of 4.5 K during construction of the lattices and measurements. An STM tip was cut from platinum-iridium wire, which was conditioned insitu by repeatedly dipping the tip into the surface and/or applying voltage pulses between tip and sample. This procedure leaves the tip with a randomly shaped apex made from copper atoms, and the process was considered complete when the tip satisfactorily performed the desired task (either atom manipulation, imaging or spectroscopy). STM topographs were acquired in constant current mode. Plane subtraction was performed on the topographs. Atom manipulation was performed with a bias voltage of 20 mV and constant current maintained with a feedback loop ranging from 10 nA to 60 nA depending on the condition of the tip. Differential conductance spectra and maps were acquired in constant height mode with bias modulation provided by a lock-in amplifier. The amplitude of the modulation was 10 mV r.m.s at a frequency of 273 Hz. Integration time for signal acquisition was 50 ms at the lock-in amplifier for spectra and 20 ms for each pixel in the differential conductance maps.

Data processing

The differential conductance spectra were processed by averaging over numerous sites of equivalent type or repeated measurements within the same site, then dividing this average by the average of many spectra on bare Cu(111). The purpose of the division by spectra on bare Cu(111) is to eliminate LDOS contributions from the tip and from the copper itself. Fig. S3.1 shows an example of average dI/dV spectra acquired with the same tip on bare Cu(111) and at a position in the edge. Certain aberrations are common in both datasets, for example the dip at 0V. These are features of the tip. In the normalised data, these features have been removed. Processing of the differential conductance maps included alignment of the forward and backwards scans, then averaging the two. A small amount of Gaussian blurring was

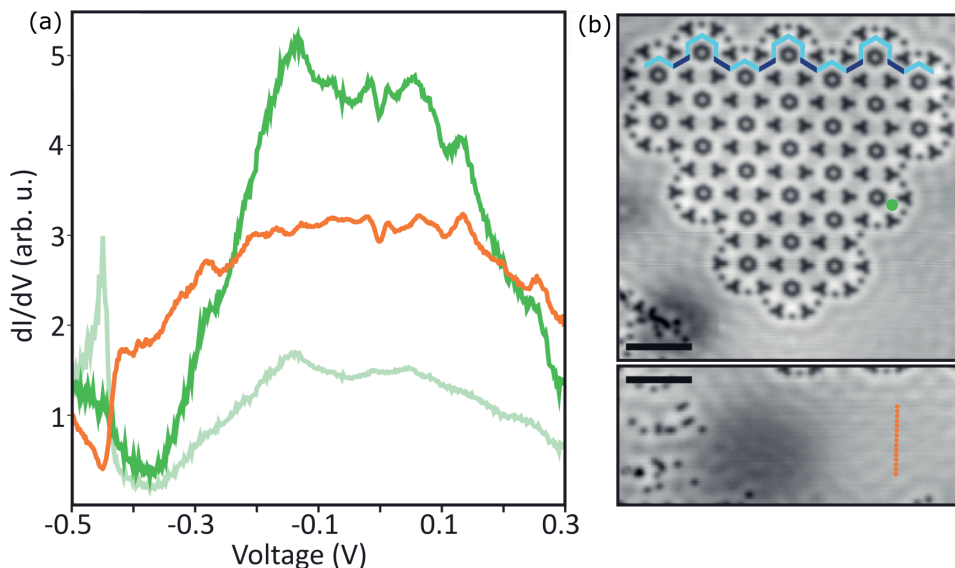


Figure S3.1: Data normalisation. (a) Bright green: dI/dV acquired on an edge site, averaged over several measurements. Orange: dI/dV averaged over numerous positions on bare copper. Pale green: Normalised and averaged dI/dV at the edge site. (b) Positions where spectra were taken marked in corresponding colours. Scale bar is 5 nm.

applied to reduce the appearance of noise in each map, except for the trivial partially bearded edged lattice, for which this was not necessary. The "sky" color map, which is perceptually uniform, was used from the freely available open source program Gwyddion [94] (with which all experimental image processing was performed).

Theoretical methods

Tight binding: Finite-size tight binding calculations were performed to simulate the experimental LDOS spectra and maps. To maximise the accuracy with which we could describe the experimental results, not only the nearest neighbour (NN) hopping parameters were taken into account, but also the orbital overlap and next nearest neighbour (NNN) hopping. To start with, the tight binding parameters are unknown, which presents an obvious difficulty when trying to model experiments. To estimate these parameters, band structures were calculated using a periodic tight binding model, and using the muffin-tin approximation (described in the next section). The tight binding parameters were adjusted until the band structure calculated from it matched that from muffin-tin. These parameters were then inserted into the finite-size tight binding model to produce LDOS spectra and maps, which ultimately parallel the experimental observations.

To produce realistic spectra and maps from the finite-size tight binding model, several things were taken into account. The first effect is the broadening of the

peaks in the experimental differential conductance spectra, arising dominantly from the finite lifetime of surface electrons. The presence of CO molecules allow an additional means by which the surface electrons can enter bulk states, which decreases the lifetime of surface electrons and broadens the LDOS. The extent of the broadening depends on the concentration of CO molecules in the immediate vicinity of the measurement; the more CO molecules per unit area, the larger the broadening. Here, we use a broadening of 80 meV [18, 20, 88]. Without broadening, the local density of states (LDOS) for an energy ϵ is determined by the wave function Ψ and given by

$$\text{LDOS}(x, y, \epsilon) = \sum_i |\Psi_{\epsilon_i}(x, y)|^2 \delta(\epsilon - \epsilon_i), \quad (\text{Supplementary Equation 1})$$

where i iterates over the energies. The broadening can be described by replacing the delta function in Supplementary Equation 1 by a Lorentzian. The LDOS is now described by

$$\text{LDOS}(x, y, \epsilon) = \sum_i |\Psi_{\epsilon_i}(x, y)|^2 \frac{b}{(\epsilon - \epsilon_i)^2 + (\frac{b}{2})^2}. \quad (\text{Supplementary Equation 2})$$

where $b = 0.08$ eV in this setup. A second significant effect is orbital overlap, which describes the non-zero overlap between the orbitals of neighboring sites. This leads to the generalised eigenvalue equation $H\Psi = ES\Psi$, where H is the Hamiltonian, E is the energy, and S is the overlap matrix. In order to limit the number of parameters to match and to avoid overfitting, we only considered NN overlap. Thus, there are two orbital overlap parameters for each design: the orbital overlap of two sites in the same hexagon, and overlap between sites of two different hexagons. If all orbitals are orthogonal, the generalised eigenvalue equation reduces to the standard eigenvalue equation, $H\Psi = E\Psi$.

Finally, NNN hopping was also included. This again gives two extra parameters, NNN hopping within and between hexagons. The magnitude of both NNN parameters in the $t_1 > t_0$ lattice are small due to the use of clusters of CO molecules. In the $t_0 > t_1$ design, however, a single CO molecule is used in the centre of the hexagon, resulting in a non-negligible intra-hexagon NNN hopping of $0.2 t_0$.

LDOS maps were obtained from the tight binding eigenvectors Ψ_ϵ with energy ϵ according to:

$$\begin{aligned} \text{LDOS}(x, y, \epsilon) &= \sum_{\epsilon'} \left| \sum_i \exp[-(x - x_i)2.15a] \right. \\ &\quad \left. \times \Psi_{i,\epsilon}(x, y) \right|^2 L(\epsilon - \epsilon'), \end{aligned}$$

where a is the lattice constant of the Kekulé lattice, L is the Lorentzian broadening function, i enumerates the sites and x_i is the position of site i .

Muffin-tin: The CO molecules in each lattice were approximated as disk shaped "protrusions" in an otherwise constant 2D potential landscape. This is the foundation of a muffin-tin calculation. For the calculations done here, a disk diameter of 0.6 nm

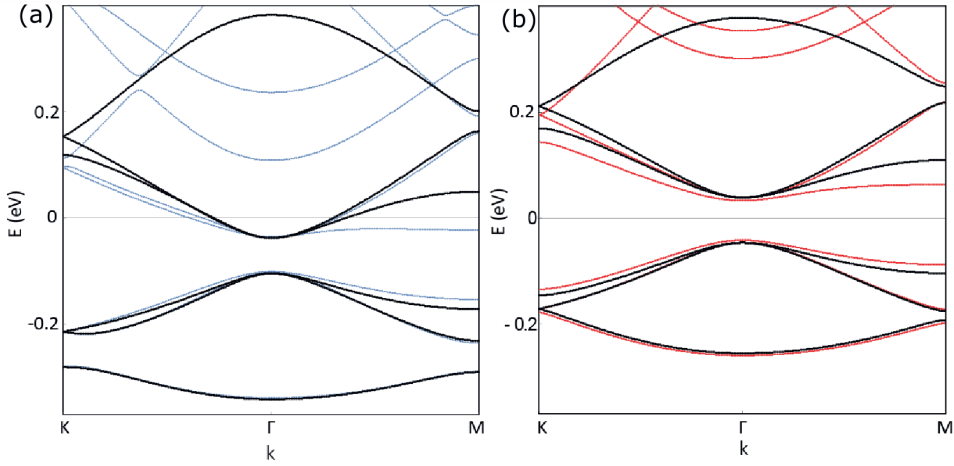


Figure S3.2: Band structure for the periodic Kekulé lattice. (a) $t_1 < t_0$ and (b) $t_0 < t_1$. The tight binding fit is displayed in black, and the muffin-tin band structure in colour (blue and red, respectively).

(based on observation from STM scans) and a potential height of 0.9 eV were used to describe the CO molecules, as used by Slot et al. [18].

The periodic tight binding Hamiltonian was expanded up to the 5th Fourier component in the plane wave basis, making use of Bloch's theorem. This was then solved numerically using the analytically known Fourier components of the muffin-tin potential [61]. The resulting band structures were then used to identify the tight binding parameters (see Fig. S3.2), where the muffin-tin band structure and the corresponding tight binding match are shown for both designs used).

When comparing muffin-tin and tight binding derived band structures, the low energy bands match each other well. For the bands at higher energy, the match becomes less accurate due to the interference with p -bands that are not included in the tight binding description, but are present in the muffin-tin model. The tight binding parameters that were obtained from this procedure are displayed in Table S3.1.

Design	t_0	t_1	t_{n_0}	t_{n_1}	s_0	s_1	e
$t_1 < t_0$	-0.13 eV	$0.7 t_0$	$0.2 t_0$	$0.02 t_0$	0.2	0.12	-0.105 eV
$t_0 < t_1$	$0.67 t_1$	-0.13 eV	0	0	0.1	0.15	-0.005 eV

Table S3.1: Tight binding parameters obtained by matching to muffin-tin band structures. Here, e is the on-site energy, t_0 and t_1 are NN hopping parameters, t_{n_0} and t_{n_1} are NNN hopping parameters, and s_0 and s_1 are orbital overlaps, each of them intra- and inter-hexagon, respectively.

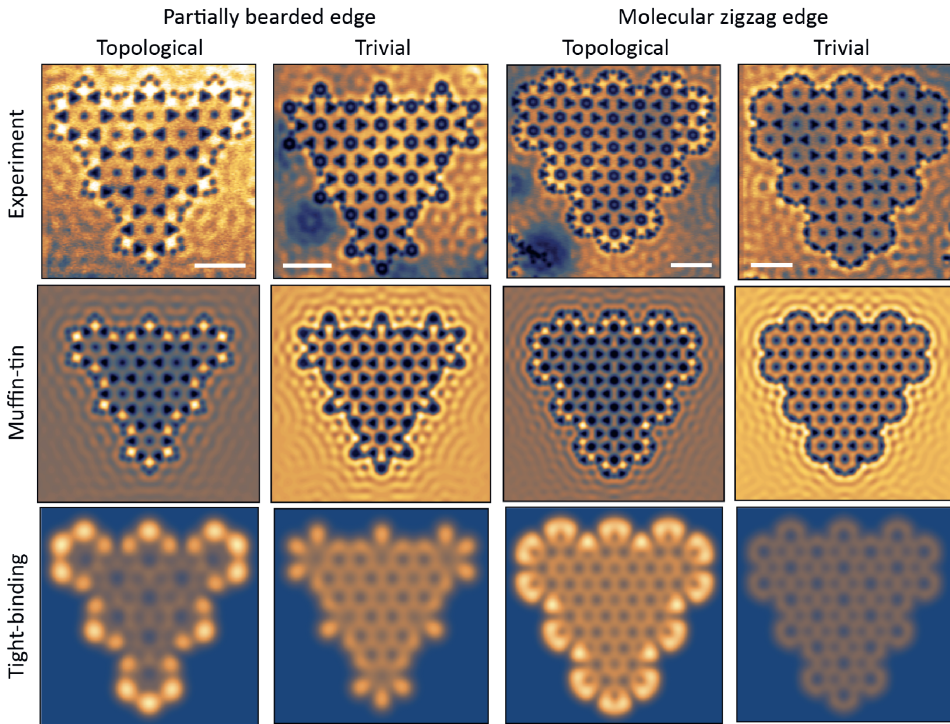


Figure S3.3: Comparison of LDOS maps. Local density of states maps at the gap energy for both edge types obtained experimentally (top row), with muffin-tin (centre row) and with tight binding (bottom row). Scale bars in white indicate 5 nm.

The experimental results (LDOS spectra and maps) were also simulated using the muffin-tin model. For a finite system, we numerically solved the non-interacting Schrödinger equation for the muffin-tin potential. A flat potential landscape surrounds each lattice, and the edges of the defined area are given by von Neumann boundary conditions. After including broadening in the same way as for the tight binding model described above, we find that the muffin-tin results closely match the experimental findings, as shown in Fig. S3.3 for the local density of states maps and in Fig. S3.4 for the local density of states spectra. In these figures, tight binding results have also been included for comparison. Spectra on additional edge sites are also included compared to those shown in the main text.

Limiting interactions with the surrounding 2DEG

At the edge of artificial lattices built by confining the surface state of a metal, there can be significant broadening as a result of the states within the lattice interacting with the surrounding free surface state. Minimizing this interaction can be achieved

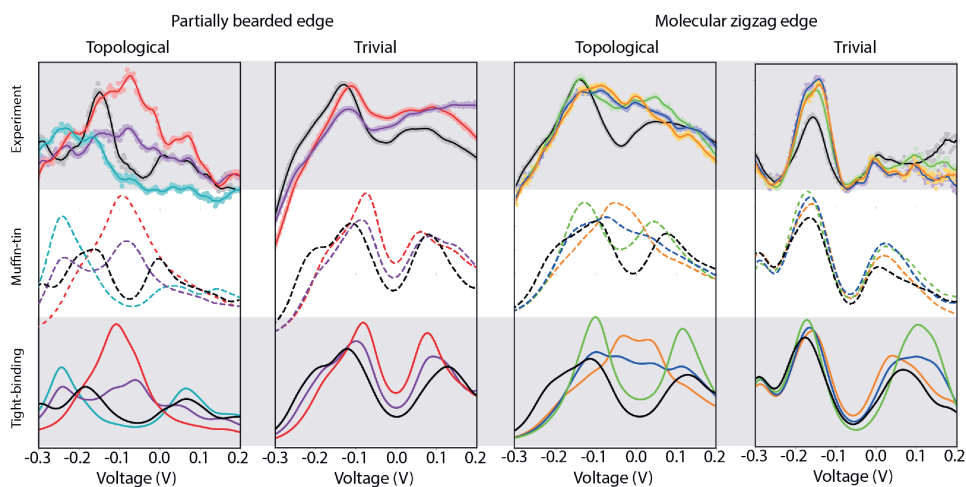


Figure S3.4: Comparison of LDOS spectra. Local density of states spectra for both edge types obtained experimentally (top row), theoretically using a muffin-tin calculation (middle row) and with tight binding (bottom row). The y axis in each plot is the local density of states in arbitrary units. Each colour refers to a type of site, as illustrated in the STM topographs.

by placing additional CO molecules at the boundaries of the structure. However, care should be taken because the positioning of CO molecules outside their regular anti-lattice may change the on-site energy of edge sites, which could lead to a spurious modulation of the spectrum. In order to find suitable positions to place the “blocker” CO molecules, several potential designs were calculated for each of the four lattices using muffin-tin, and those that yielded the best fit to the tight binding predictions were chosen. An example using the molecule zigzag edge for $t_0 < t_1$ is shown in Fig. S3.5. Here, multiple blocker positions (and an edge with no blocking) are shown alongside the corresponding muffin-tin spectra. The broadening is plain to see in the LDOS calculated for the design with no blocking (Fig. S3.5(a)) – no clear similarities to the tight binding calculated LDOS are seen. When blockers are introduced too far away as in Fig. S3.5(b), familiar behaviour is observed, except the on-site energy of the edge sites are shifted to lower energies because the edge states are less confined. Upon repositioning the blocker-CO molecules one Cu(111) atom distance closer (Fig. S3.5(c)), the on-site energies of the sites are shifted towards higher energies. Finally in Fig. S3.5(d), after shifting the blockers one site closer still, the on-site energy becomes approximately comparable to the bulk minimum. Thus, this was the design chosen for our investigation. Similar calculations were performed for the three remaining lattices to find the best position for CO blockers.

Defects at the edges

One of the most exciting aspects of topological insulators is the resilience of the edge modes to non-symmetry breaking defects. To test this, we introduce CO molecules

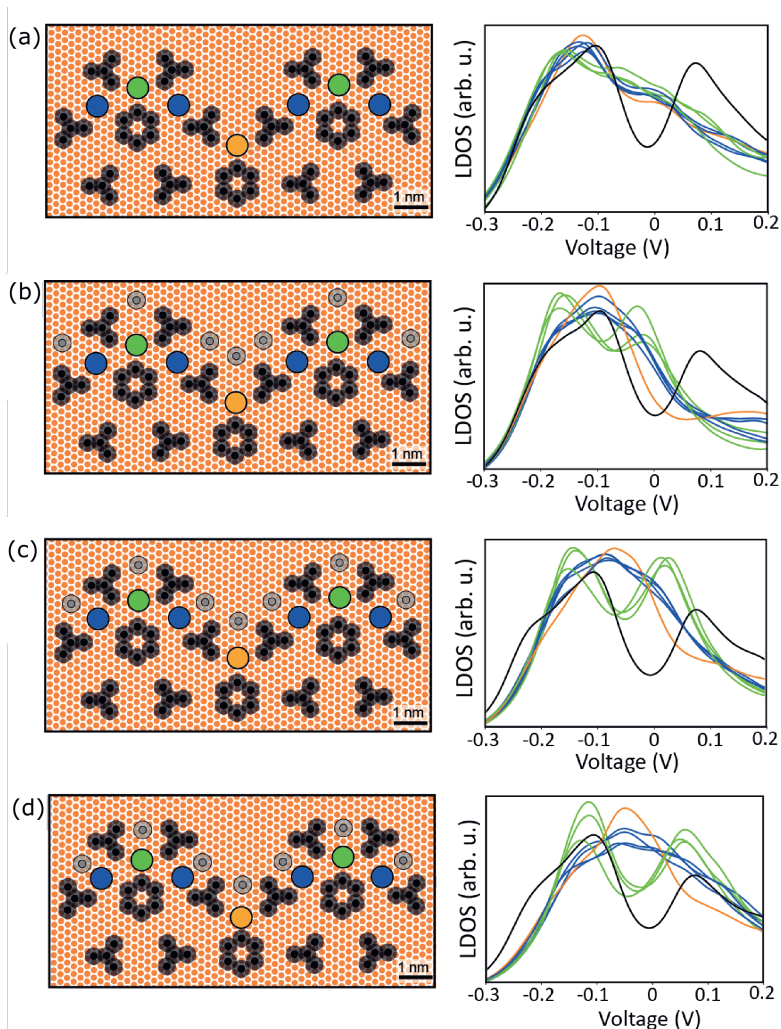


Figure S3.5: The effect of protective “blocker” CO molecules. The left column shows positions of CO molecules (black circles) on the Cu(111) surface (orange dots) to form the molecule zigzag edge of the Kekulé lattice. Grey dots represent CO molecules that are used to shield the electronic states in the lattice from unwanted interactions with the surrounding 2DEG. The spectra were calculated on the dots of corresponding colour, except the black line, which was calculated for the bulk. A spectrum was taken for equivalent sites at the corner and edges, thus there are multiple spectra of each colour. (a) The lattice with no blocking CO molecules and the corresponding spectra. (b) Blocking at distant positions, leading to a shift of the edge modes to lower energy. (c) An improvement on (b), where the blocking CO molecules are shifted one Cu(111) atom distance closer. (d) The final design used in our investigation, where the CO molecules are pushed one additional site closer and the on-site energy of the edge mode is comparable to the energy of the bulk gap.

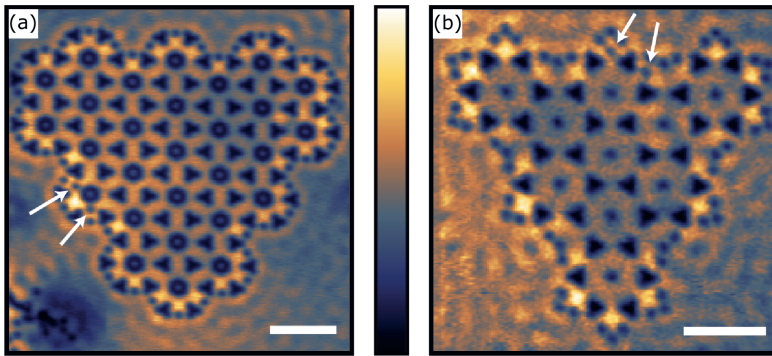


Figure S3.6: **Defects in edges.** Experimental differential conductance maps showing the effect of defects in the edge modes of the lattices. Brighter pixels represent higher LDOS. White arrows point to the defects. Scale bars represent 5 nm. (a) The molecular zigzag edge with $t_0 < t_1$ (acquired at -40mV). (b) The partially bearded edge with $t_1 < t_0$ (acquired at -65mV).

into the edge to behave as defects. Fig. S3.6 shows experimental differential conductance maps, where defects have been introduced. Sites on opposite sides of the defect should only couple very weakly via the defect, possibly affecting the shape of the edge. By examining Supplementary Figure 5, it can be seen that the edge modes still exist despite the defects, even in close proximity to them, thus substantiating the topological character of the edge.

Larger lattices

Upon increasing the system size, the states become more dense, compare Fig. S7 and Fig. 3.3(b). The finite size of the system leads to hybridization, thus moving the zero-energy modes away from zero in parameter space: while the zero modes already deviate from zero energy at roughly $t_0/t_1 = 0.7$ in Fig. 3.3(b), in Fig. S7, they remain close to 0 up to a larger value, about $t_0/t_1 = 0.9$.

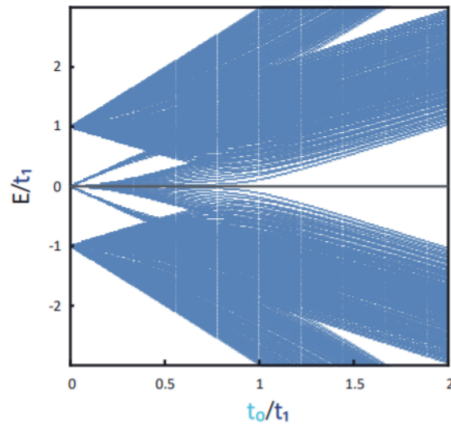


Figure S3.7: Energy spectrum as a function of t_0/t_1 for a finite size system of 163 hexagons with same corner and edge geometry as in the experiments.

p Orbital flat band and Dirac cone in the electronic honeycomb lattice

This chapter is partially based on the following publications:

T. S. Gardenier*, J. J. van den Broeke*, J. R. Moes, I. Swart, C. Delerue, M. R. Slot, C. Morais Smith & D. Vanmaekelbergh, *P orbital flat band and Dirac cone in the electronic honeycomb lattice*, **ACS Nano**, vol. 14, no. 10 (2020)

M. R. Slot, S. N. Kempkes, E. J. Knol, W. M. J. Van Weerdenburg, J. J. van den Broeke[†], D. Wegner, D. Vanmaekelbergh, A. A. Khajetoorians, C. M. Smith & I. Swart, *p-Band engineering in artificial electronic lattices*, **Physical Review X**, vol. 9, no. 1 (2019)

*Both authors contributed equally, T. S. Gardenier performed the experiments and J. J. van den Broeke did the theoretical calculations.

[†] J. J. van den Broeke did the theoretical calculations for the honeycomb geometry.

Theory anticipates that the in-plane p_x , p_y orbitals in a honeycomb lattice lead to potentially useful quantum electronic phases. So far, p orbital bands were only realized for cold atoms in optical lattices and for light and exciton-polaritons in photonic crystals. For electrons, in-plane p orbital physics is difficult to access since natural electronic honeycomb lattices, such as graphene and silicene, show strong s - p hybridization. Here, we report on electronic honeycomb lattices prepared on a Cu(111) surface in a scanning tunneling microscope that, by design, show (nearly) pure orbital bands, including the p orbital flat band and Dirac cone.

4.1 Introduction

The electronic properties of two-dimensional solids, including materials with Dirac bands and topological insulators, are largely determined by the geometry of the atomic lattice and the nature of the interacting orbitals [95, 96]. A compelling case is presented by the system of in-plane p_x p_y orbitals in a honeycomb lattice providing an electronic flat band, due to geometric frustration, and a p type Dirac cone [97–99]. The in-plane p orbitals in the trigonal honeycomb lattice cannot form conventional bonding – antibonding combinations; their interaction gives rise to complex interference patterns. As a result, the four in-plane p bands consist of a non-dispersive flat band, followed by two dispersive bands forming a Dirac cone at higher energy, followed by another flat band. Intrinsic spin-orbit coupling will open a gap at the Dirac point (the quantum spin Hall effect) and detach the flat band from the Dirac cone, making it topological [71, 100]. Since the kinetic energy is quenched in the flat band, the dominant energy scale is set by interactions. It has been predicted that this will lead to interesting quantum phases, such as unconventional superconductivity and Wigner crystals [99, 101]. The physics of in-plane p orbitals in a honeycomb has been studied with ultracold atoms in optical lattices [101–105], [103]light in photonic systems [106], exciton-polaritons in a semiconductor pillar array [107, 108], and has been theoretically investigated for real layered materials [109]. However, an experimental realization of an electronic material in which the physics of in-plane p orbitals can emerge by design has so far only been reported in a square geometry [29]. In this case, the p orbital symmetry fits naturally with the lattice, and the degeneracy between the orbitals can be lifted by manipulating the length scales in the in plane directions independently. This is not the case for the honeycomb geometry investigated here, as the symmetry of the

p orbitals is not commensurate with this lattice.

4.2 Results and discussion

Natural electronic honeycomb systems show interesting results, but there is considerable hybridization between different types of orbitals [100]. In graphene, the most studied electronic honeycomb lattice, the s - and in-plane p_x, p_y orbitals of the carbon atoms hybridize and form sp^2 electronic bands, the lower one being completely filled [97]. This filled band leads to a very strong in-plane bonding between the carbon atoms, but is not electronically active. The remaining p_z orbitals (perpendicular to the graphene plane) form π bonds, resulting in two bands touching at the (K, K') Dirac points at which the Fermi energy is situated. The linear energy-wave vector dispersion (Dirac cone) around the (K, K') points is responsible for the electronic properties of graphene [97]. We remark that bilayer graphene twisted at magic angles offers exciting physics whereby interlayer coupling and interacting electrons result in a flat band and unconventional superconductivity [26, 110].

Here, we report solid-state designs for non-interacting electrons in which the physics of in-plane p orbitals fully emerge. Our work is inspired by the work of Gomes et al. who reported an artificial electronic honeycomb lattice based on the surface state electrons of a Cu(111) surface [15]. In that work, the confinement of the surface state electrons in a honeycomb geometry by CO molecules leads to a Dirac cone formed by the first two surface bands at the high symmetry K point. It has been shown afterwards that this concept can be extended to create systems with different geometries [18], fractal structures [20], non-trivial topology [27, 88] and multiple orbitals by changing the size of the lattice sites [29]. Using this last concept, we design honeycomb lattices consisting of atomic sites with a variable degree of quantum confinement, and electronic coupling between them. Muffin-tin calculations show that it is possible to create lattices in which the on-site s orbitals and p orbitals are sufficiently separated such that $s-p$ hybridization can be avoided and Dirac-cones and a flat band emerge with nearly pure p orbital character. The band structure is experimentally investigated by measurement of the local density of states and wave function mapping.

The theoretically designed honeycomb lattices are presented in Fig. 4.1, with the original lattice by Gomes et al. [15] (Fig. 1(a)), and two geometries where the splitting of s - and p orbitals is enhanced (vide infra) (Fig. 4.1(b, c)). We have calculated the electronic band structure of these lattices by solving the Schrödinger equation with a muffin-tin potential accounting for the rosettes of CO molecules as repulsive scatterers [55]. A broadening of 40 meV was used in the muffin-tin calculations to account for the intrinsic coupling of surface and bulk states in the CO/Cu(111) system. The resulting band structures are presented in Fig. 4.1(d-f). In addition, we fitted the muffin-tin band structure with a tight-binding model based on artificial atomic sites in a honeycomb lattice; each atomic site has one s orbital and two in-plane p orbitals, and we assume s - s , s - p and p - p hopping between neighboring sites. We obtained excellent agreement between the two band structures for all but the highest bands, as the tight binding calculation does not take bands of energies higher than the p orbitals into account (see 4.4 and 4.4 for more details and fitted

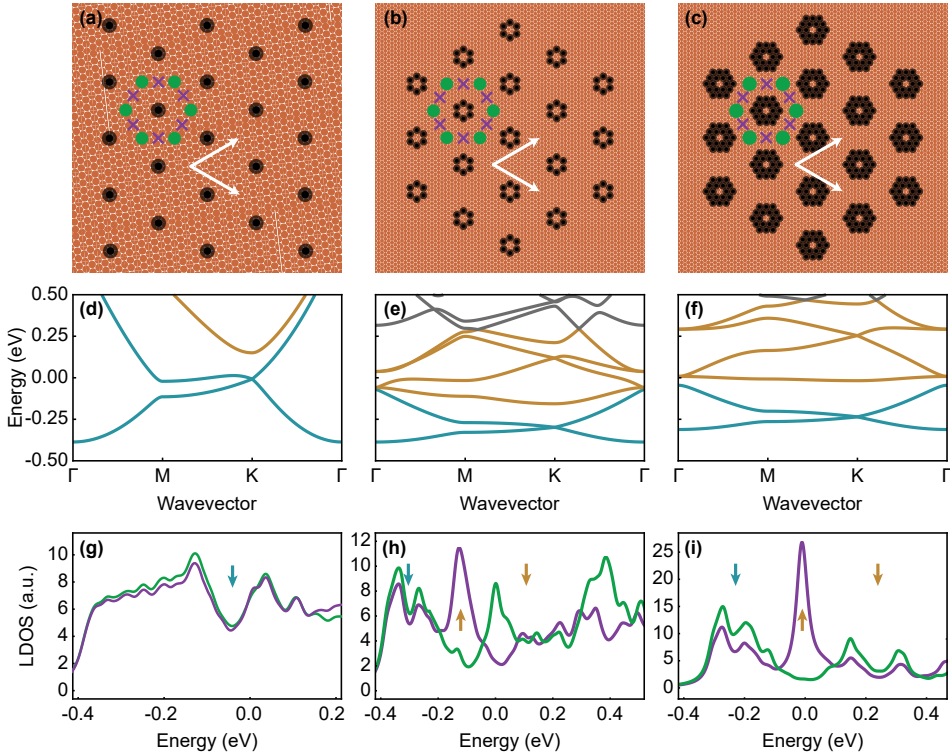


Figure 4.1: Designs for artificial atoms in a honeycomb lattice, corresponding band structures and LDOS spectra. (a-c) Schemes of a Cu(111) surface (copper) and the positions of the CO molecules (black) defining the on-site energies of the s - and p orbitals and their inter-site coupling. The lattice sites are indicated in green, the bridge sites with purple crosses. (a) The lattice reported by Gomes *et al* [15], with a honeycomb lattice vector of 1.92 nm. (b) Lattice with single-ringed CO rosettes as scattering islands and a honeycomb lattice vector of 3.58 nm, corresponding to 14 Cu atoms, (c) lattice with double-ringed CO rosettes as scattering islands, the lattice vector is also 3.58 nm. (d-f) Corresponding band structures calculated by the muffin-tin approximation. The band structures for the designs (b) and (c) reflect (nearly) separated s (blue) and p (orange) orbital bands. (g-i) The LDOS for these three designs; green for the on-site positions, purple for the bridge positions between the sites. Blue arrows indicate the s orbital Dirac point, orange arrows indicate the p orbital flat band and the p orbital Dirac point. A broadening of 40 meV is included to account for scattering with the bulk.

parameters). The calculations predict a single Dirac cone (blue color) for the lattice by Gomes *et al.* (Fig. 4.1(d, g)), in agreement with the experimental results reported. For this lattice, our calculations show that the next band (orange color) is strongly dispersive and extends outside the Cu(111) surface state energy window (-0.45 V to +0.5 V). To be able to lower the energy of the p bands, the lattice constant was increased [15, 18]. Additionally, to be able to separate the on-site s - and p orbitals, we increased the on-site quantum confinement by using single and double CO rosettes as potential barriers.

The design presented in Fig. 4.1(b) is based on single CO rosettes [29]. In this case, two dispersive s orbital bands emerge, forming a Dirac cone (blue). The four p orbital bands (orange) contain a (nearly) flat band and two dispersive bands forming a Dirac cone. However, in this design the s - and p bands are not separated. We remark here that in the context of real materials, similar-sized lattices of graphene in a graphene matrix have been considered by DFT and tight-binding calculations; in this system, there is strong hybridization between the carbon s and in-plane p_x, p_y orbitals, while the Dirac properties arise from the coupling of the perpendicular p_z orbitals [111]. In order to prevent this s - p hybridization, the on-site s - and p energy levels must be better separated by quantum confinement. This is achieved with the lattice presented in Fig. 4.1(c) (double-ringed CO rosettes as scatterers), showing the p orbital flat band and Dirac cone, well separated in energy from the lower s Dirac cone. The LDOS calculated for designs (b) and (c) (Fig. 4.1(h, i)) display a double peak with a minimum, reflecting the s Dirac cone, followed by a single peak with high LDOS due to the p orbital flat band, followed by a second double peak due to the p orbital Dirac cone. This indicates that our lattices are appropriate electronic quantum simulators for the study of the in-plane p orbital physics.

First, we present an overall electronic characterization of the honeycomb lattice according to the design shown in Fig. 4.1(c). The results on the other lattice (Fig. 4.1(b)) are given in 4.4. Fig. 4.2(a) shows a scanning tunneling microscope image using a Cu tip. Details are presented in Fig. S4.5, displaying a nearly identical lattice but now imaged with a CO-terminated tip. The LDOS could be probed with scanning tunneling spectroscopy by placing the metallic Cu-coated tip above the center of the artificial sites (green circles in Fig. 4.1(c) and 2(a)) and on bridge sites between the lattice sites (purple crosses); the bias voltage was changed over the entire voltage region of the Cu surface state between $V = -0.4$ and $+0.5$ V. The LDOS, i.e. normalized dI/dV vs. bias voltage [15], spectra on the on-site and bridge site positions are presented in Fig. 4.2(b), see Fig. S4.6 for details; they should be compared with the theoretical muffin-tin spectra, for convenience replotted from Fig. 4.1(i) in light colours.

The first double peak (peaks 1 and 3) corresponds to two s orbital bands forming a Dirac cone, the minimum indicates the Dirac point (point 2). The two maxima correspond to the high LDOS at the M points (see 4.4); if the overlap integral between neighboring s orbitals is neglected, the distance between these two maxima provide a good estimation for two times the hopping term between the nearest-neighbor s orbitals, i.e. $2t_{ss}$ (see 4.4). The t_{ss} value that we obtain is 45 meV. From a tight-binding fit, taking the overlap into account, we find 60 meV. The two s orbital bands do not show the typical bonding (lowest s band) and anti-bonding (higher s band)

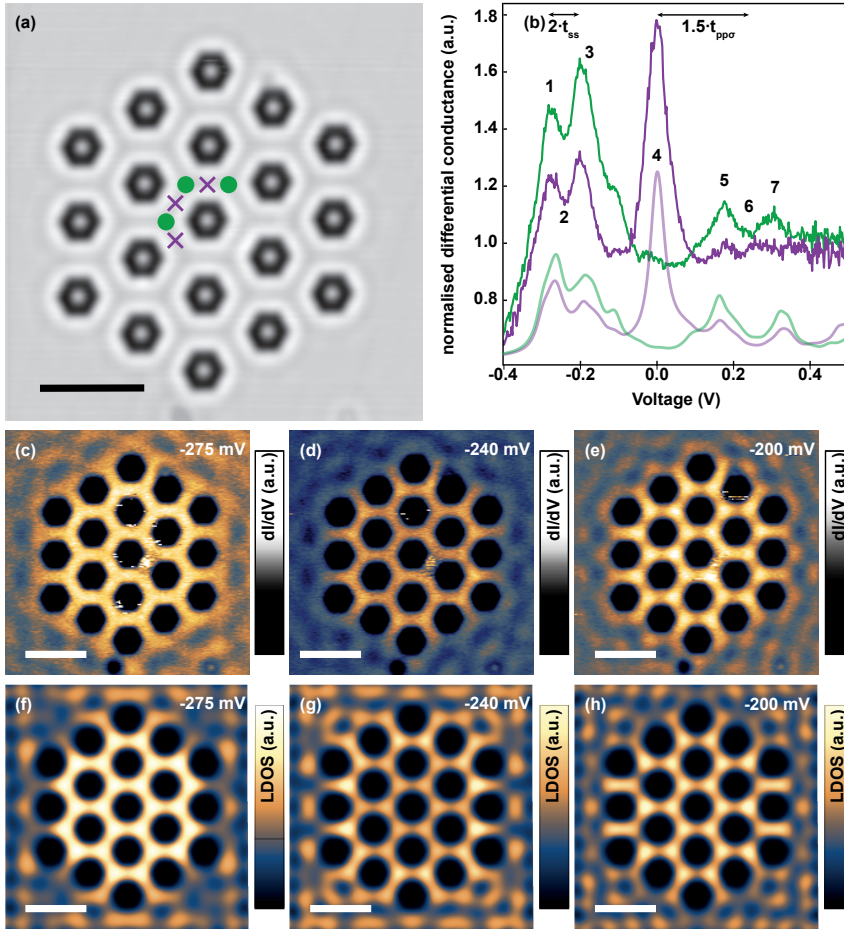


Figure 4.2: Scanning tunneling spectroscopy and electron probability maps of an artificial honeycomb lattice with separated s - and p bands. (a) Scanning tunneling microscopy image (0.5 V, 0.3 nA) of the artificial honeycomb lattice prepared with double-ringed rosettes according to scheme 4.1(c); a detailed image for a similar lattice is presented in Fig. S4.5. The bright spot in the center of the rosettes is typically found in dI/dV plots at positive bias. Other examples can be found in 4.4. (b) The LDOS, i.e. $(dI/dV)_{\text{lattice}}/(dI/dV)_{\text{Cu}}$, vs. bias voltage V , measured by scanning tunneling spectroscopy, on top of the artificial atom sites (green) and bridge sites (purple). The LDOS calculated using the muffin-tin approach is replotted in light green and light purple for comparison. The magnitudes of t_{ss} and $t_{pp\sigma}$ are indicated. (c, d, e) Spatially resolved LDOS maps in the energy region of the lowest Dirac cone (points 1-3 in Fig. 4.1(b)) measured at constant height with (f, g, h) the same maps calculated with a muffin-tin potential landscape. The high density of states at the sites reflect s orbital bands. Scale bars are 5 nm.

character. An analytical tight-binding model presented in 4.4, provides a detailed explanation.

Around $V = 0$ V, a very strong LDOS peak is observed on the bridge sites, while the LDOS on the lattice sites is very low (peak 4). A comparison with the muffin-tin band structure, and the tight-binding fit to it, reveals that this strong resonance localized between the sites is due to the flat band originating from p orbitals. The high electron probability observed between the lattice sites will be discussed in detail below. Between 0.1 and 0.4 V, we find a second double peak with a minimum. Comparison with our calculations shows that this feature reflects the dispersive p orbital bands; the minimum corresponds to the Dirac point (point 6), the lower maximum (peak 5) reflects the high LDOS at the M point. The maximum at higher energy (peak 7) corresponds to the third and fourth p orbital bands. If the orbital overlap and residual s - p hybridization are neglected, the energy difference between the flat band maximum and the Dirac point is $1.5 t_{pp\sigma}$; from this, $t_{pp\sigma}$ is found to be 160 meV. From the muffin-tin calculations combined with a tight-binding fit we find a value of 127 meV (see Table S4.1).

Figures 4.2(c, d, e) display energy-resolved LDOS maps in the energy region of the s bands measured over the entire lattice at a constant tip-sample distance, while the panels below (Fig. 4.2(f-h)) show the electron probabilities calculated with the muffin-tin model. There is a good agreement between the observed and calculated LDOS; the large on-site LDOS reflects the on-site s orbitals, the LDOS at the Dirac point is much lower, but does not vanish completely. This reflects a certain broadening of the resonances due to the coupling of the lattice states with surface states outside the lattice and with Cu bulk states. A discussion of the LDOS maps in the s band region from the tight-binding perspective is given in see 4.4.

Maps of the electron probability measured in the energy region of the p bands are presented in Figs. 4.3(a) and (b); Figs. 4.3(c) and (d) show the calculated results. The electron probability pattern at the flat-band energy has a very high electron probability between the sites, and a very low probability on the sites [Figs. 4.3(a), (c) and inserts]. In addition, the electron probability (LDOS) map in the region of the p orbital Dirac cone show detailed patterning [Figs. 4.3(b), (d) and insert], see also 4.4. The low on-site electron probability on the center of the lattice sites show that these two bands are formed from p orbitals.

The intricately patterned electron probabilities observed in the energy region of the p orbital bands in the honeycomb lattice require further investigation. The interaction of in-plane p orbitals at the sites of a honeycomb lattice can best be described as orbital interference by geometric frustration [100]. We have calculated these interference patterns by using the original tight-binding theory [99, 100], see Fig. 4.4. The results of the muffin-tin calculations combined with a tight-binding parameter fit are presented in Figs. S4.2(c) and (d). At the flat band energy, different points in the Brillouin zone show distinct interference patterns from the in-plane p orbitals, two of them being presented in Fig. 4.4(a, b). The overall sum of the electron probability patterns over the Brillouin zone at the energy of the flat band is presented in Fig. 4.4(c), showing a strongly enhanced electron probability on the bridge sites, in full agreement with the experimental results. Likewise, as originally proposed in Ref. [99], Wannier-like eigenstates with the flat band energy can be constructed

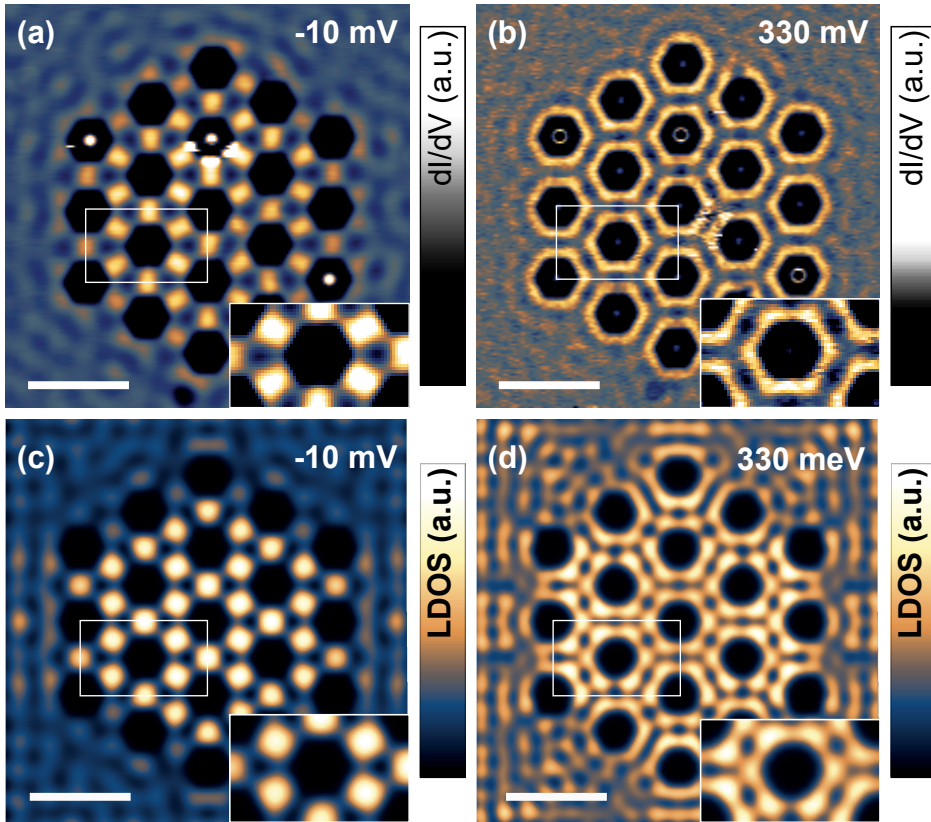


Figure 4.3: Electron probability (LDOS) maps in the energy region of the p orbital flat band and p orbital Dirac cone obtained by energy-resolved scanning tunneling microscopy at constant height. Spatially resolved LDOS measured at (a) the flat band energy [point 4 in Fig. 4.2(b)] showing patterns of very high electron probability at bridge sites, and very low probability on the atomic sites; (b) in the energy region of the p orbital Dirac cone [point 7 in Fig. 4.2(b)]. Several bright spots assigned to mobile hydrogen species are visible in the maps; however, these spots do not perturb the observed pattern. The LDOS calculated using a muffin-tin approach for (c) the flat band showing a pattern of large electron densities between the sites, and very low electron density on the sites, to be compared with the experimental result in Fig. 4.3(a); (d) the energy region of the p orbital Dirac cone, showing a good agreement with the intriguing patterns experimentally observed. More information can be found later in this chapter. The inserts show a magnification. Scale bars are 5 nm.

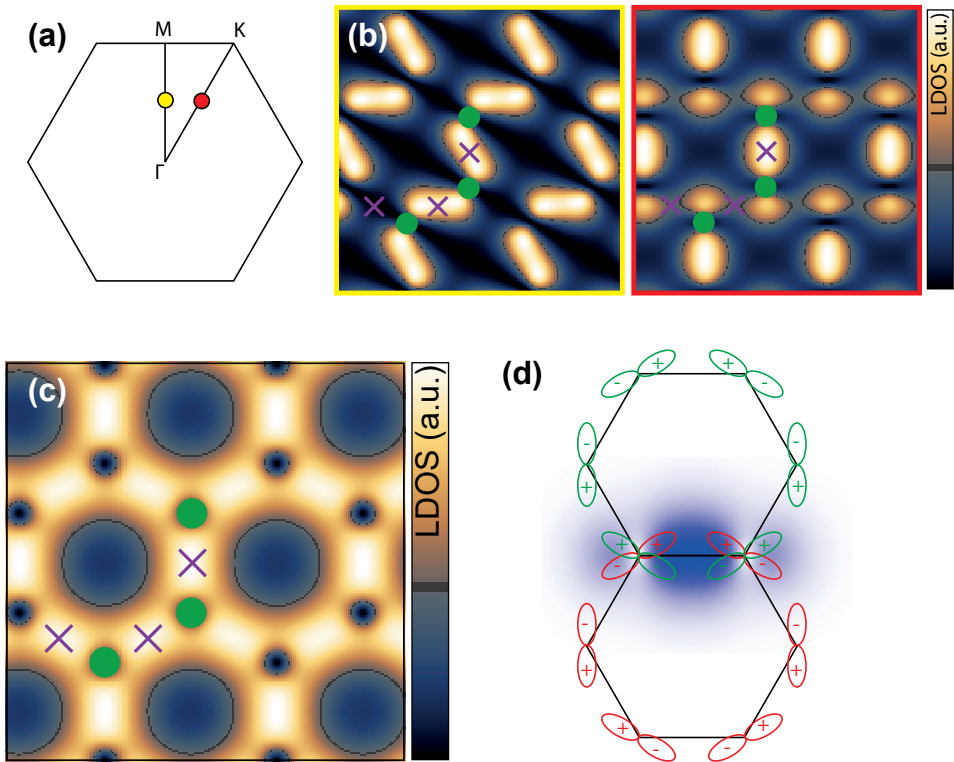


Figure 4.4: Tight-binding calculation of the interference patterns of the in-plane p_x, p_y orbitals in the honeycomb geometry and the resulting electron probabilities in the p type flat band. (a) Scheme of the Brillouin zone with Γ , M and K points indicated. The yellow (red) circles denote the positions in the zone used in panel (b). (b) Two spatial patterns due to interference of the p_x, p_y orbitals in the honeycomb geometry at the flat band energy (-0.01 V) at the two points in the Brillouin zone indicated in panel (a). Artificial atom sites (green) and bridge sites (purple) are indicated. (c) The overall electron probability at the flat band energy obtained from the interference patterns (see panel (b)) and summed over the entire Brillouin zone. Strong electron probabilities are observed on bridge sites (purple crosses) as in the experimental maps. (d) Representation of the electron probability map at the flat band energy by construction of Wannier-like eigenstates from p orbitals organized around a hexagon. The dark blue color indicates high electron probability. See also Fig. S4.9(c).

around each CO rosette of artificial sites resulting in a high electron probability between the lattice sites (also called bridge sites), see Fig. 4.4(d). This spatial electron probability pattern in the flat band agrees with the experimental results and the result of muffin-tin calculations, see Fig. 4.3. In addition, a comparison between Fig. 4.3(b) and 4.3(d) shows that the spatial patterns of the LDOS in the p orbital Dirac region are well reproduced by the muffin-tin calculations.

4.3 Conclusions

Our results show that solid-state electronic honeycomb lattices can be designed in such a way that in-plane p orbital physics fully emerges. The design is purely based on the lattice geometry and the degree of quantum confinement and inter-site coupling. These concepts can, therefore, be directly transferred to two-dimensional semiconductors in which the honeycomb geometry is lithographically patterned [14, 112–114], or, obtained by nanocrystal assembly [71, 115]. Such honeycomb semiconductors can be incorporated in transistor-type devices in which the Fermi level and thus the density of the electron gas can be fully controlled [14, 116]. For instance, a partial filling of the flat band can result in electronic Wigner crystals, magnetic phases and superconductivity [99, 100]. Hence, we present a feasible geometric platform for real materials opening the gate to unexpected electronic quantum phases, both in the single-particle regime [2, 55, 70, 71] as in the regime with strong interactions [117–119].

4.4 Methods

The measurements were obtained in a Scienta Omicron LT-STM. It was operated at a base temperature of 4.5 K and with a pressure in the 10^{-10} mbar range. A clean Cu(111) surface was prepared by multiple sputtering and annealing cycles [120]. CO molecules were deposited on the sample placed in a cooled measurement head by leaking in gas at a pressure of 2×10^{-10} mbar for 3 min. The STM tips were PtIr coated with Cu due to tip preparation. Atomic scale lateral manipulation of the CO molecules was performed to build the honeycomb lattices using previously obtained parameters of 40 nA and 10 mV [15, 49, 121]. Unless mentioned otherwise, all STM topography images were acquired at a constant current of 1 nA and 500 mV. Wave function mapping and differential conductance spectroscopy were performed using constant-height mode with a lock-in amplifier providing a 273 Hz bias modulation with an amplitude between 5 and 20 mV rms. Experimental data was analyzed with the SPM analysis software Gwyddion 2.49 and/or Python 3.7.

The design of the CO rosettes was determined by previously acquired knowledge about CO manipulation [15] and muffin-tin band structure calculations. The double-ringed rosette consists of 18 CO molecules arranged in two rings placed around a central (empty) Cu lattice site as shown in Fig. 4.1(c). This central site was left clear for ease of building. The rosettes were placed at a 3.58 nm spacing (14 Cu atomic sites) along close-packed Cu atomic rows.

All band structures and theoretical LDOS maps shown Fig. 4.1-4.3 of the main

text were calculated using the muffin-tin model. The surface state of Cu(111) is modelled as a two-dimensional electron gas with an effective electron mass of 0.42 times the free electron mass, at a constant potential. The CO molecules are portrayed as discs with a diameter of 0.6 nm and a repulsive potential of 0.9 eV. These parameters were used previously to successfully describe the CO on Cu(111) system [18]. When CO molecules were placed close together and the radii overlapped, the potential of that area was added together and increased to 1.8 eV. The one electron Schrödinger equation was solved numerically for this system to determine the band structure (periodic case) and LDOS maps (finite size). For the LDOS maps, Neumann boundary conditions were applied. In order to obtain the maps shown, a broadening of 0.04 eV was included.

Supplementary Information

Tight-binding analysis of the s and p orbital bands in artificial honeycomb lattices

In the main text, we have compared the experimental spectra and spatial LDOS maps with a muffin-tin calculation (see Fig. 4.2, 4.3), showing a very good agreement between experiment and theory. It is however very insightful to also perform simple tight-binding (TB) calculations, in order to show which atomic site orbitals are involved in the band formation and to estimate the strength of the coupling between specific orbitals.

In the TB approximation, we assume that due to the repulsive potential of the CO rosettes atomic sites can be defined, with s and p orbitals (see Fig. S4.1(a)). We can choose the on-site energy of the s and (two) p energy levels, they are denoted as e_s and e_p . The interaction energy, i.e. hopping (in eV) between the s orbitals of two neighboring sites is denoted by t_{ss} , the hopping between s and in-plane p_x and p_y orbitals by t_{sp} , the σ type interaction integral between the in-plane p orbitals on adjacent sites by $t_{pp\sigma}$, and the π hopping between in-plane p orbitals by $t_{pp\pi}$. These hoppings are depicted in Fig. S4.1(a). We neglect the on-site orbitals at higher energy in this simple approximation. The TB Hamiltonian is:

$$\begin{pmatrix} H_1 & H_2 \\ H_2^\dagger & H_1 \end{pmatrix} \quad (4.1)$$

with

$$H_1 = \begin{pmatrix} e_s & 0 & 0 \\ 0 & e_p & 0 \\ 0 & 0 & e_p \end{pmatrix} \quad (4.2)$$

and

$$H_2 = \begin{pmatrix} t_{ss}(w + 2v) \cos[m] & t_{sp}(-w + e^{-\frac{\pi}{2}} \cos[m]) & t_{sp}i\sqrt{3}v \sin(m) \\ t_{sp}(w - v \cos[m]) & -t_{pp\sigma}w - \left(\frac{t_{pp\sigma}}{2} - \frac{3t_{pp\pi}}{2}\right)v \cos(m) & -(t_{pp\sigma} + t_{pp\pi})\frac{i\sqrt{3}}{2}v \sin(m) \\ -t_{sp}i\sqrt{3}v \sin(m) & -(t_{pp\sigma} + t_{pp\pi})\frac{i\sqrt{3}}{2}v \sin(m) & t_{pp\pi}w - \left(\frac{3t_{pp\sigma}}{2} - \frac{t_{pp\pi}}{2}\right)v \cos(m) \end{pmatrix} \quad (4.3)$$

where

$$m = \frac{k_y}{2}, v = e^{-\frac{ik_x}{2\sqrt{3}}} \text{ and } w = e^{\frac{ik_x}{\sqrt{3}}}.$$

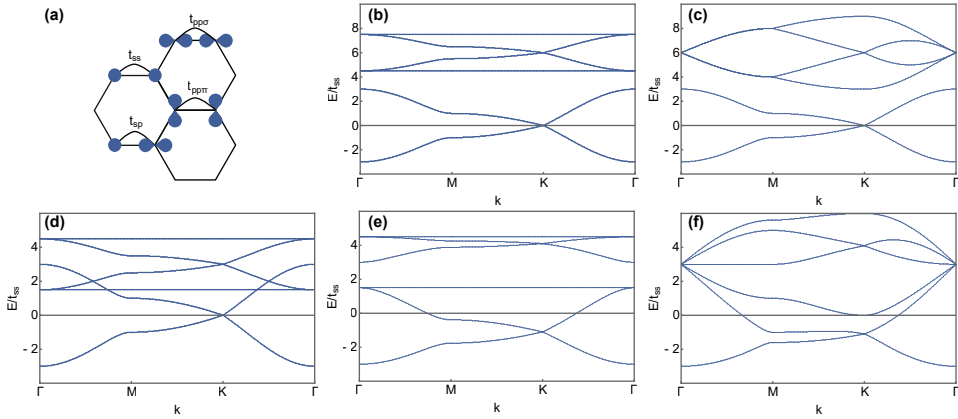


Figure S4.1: Tight-binding band structures, for various values of the hopping parameters. (a) Scheme of the possible hoppings between s and in-plane p orbitals of adjacent atomic sites in the honeycomb lattice. (b) A generic band structure for pure s and p orbital bands, by assuming there is no coupling between s and p orbitals, i.e. $t_{sp} = 0$ and no π hopping. (c) A band structure showing the effect of π hopping between the in-plane p orbitals, resulting in some dispersion of the bands that were flat in (b). (d-f) The effect of reducing the energy difference between the on-site s and p energy levels. (d) Bands cross as t_{sp} is set equal to zero. (e) The effect of s - p coupling results in two groups of (sp^2) bands, with Dirac cones and flat bands. (f) When $t_{pp\pi}$ is set to non-zero, the formerly flat bands obtain a dispersion.

In Fig. S4.1(b-f), we show how different hopping parameters influence the band structure. Here, we neglect the overlap integrals. If t_{sp} is zero, there is no hopping between the s and p orbitals, thus no hybridization, and the bands formed should have pure s character (two bands) and pure p character, (four bands). The s bands form a Dirac cone with the Dirac point at zero energy. The orthogonal in-plane p orbitals are not commensurate with the trigonal binding structure (see Fig. 4.4). This results in two flat bands, with a Dirac cone between these flat bands (Fig. S4.1(b)). If $t_{pp\pi}$ is non-zero, the two flat bands acquire a dispersion, while the p orbital Dirac point is preserved. Here we also take $t_{pp\pi}$ equal to $t_{pp\sigma}$, resulting in a fourfold degeneracy of the p bands at the Γ point, see Fig. S4.1(c).

In Fig. S4.1(d, e) we show what happens if the energy difference between the on-site p and s orbitals is lowered and if s - p hopping is allowed. First, in panel (d), we show the bands with reduced on-site energy difference, but still with t_{sp} being zero. This results in unrealistic crossing points between the s and p bands. The introduction of hopping between s and p orbitals of adjacent sites results in a grouping of three lower bands and three higher bands, separated by a gap. There is a downwards shift of the lower Dirac cone, and an upwards shift of the second Dirac cone. The lower flat band touches the lower Dirac cone. Finally, panel (f) shows an example if all hopping parameters are non-zero; the two Dirac cones are preserved, but the originally flat bands obtain a dispersion due to π hopping.

Parameterization of the tight-binding hoppings in order to obtain maximum agreement with the experimental results and the muffin-tin approximation.

In the main text, the experimental results are compared with a muffin-tin calculation of the band structure. The potential landscape of the individual CO molecules and CO rosettes on Cu(111) can be modelled using a muffin-tin (MT) potential. This is done by adding disk-shaped potential barriers to an otherwise flat potential landscape, resulting in an upside-down muffin tin like structure. In this work, disk diameters of 0.6 nm and potential heights of 0.9 eV were used to account for each CO. By analytically Fourier-transforming the muffin-tin potential landscape and using Bloch-type wave functions, we calculate the electronic band structure for electrons in the honeycomb lattices presented in Fig. 4.1.

In order to be able to discuss the strength of the hoppings between the on-site s and p orbitals, we have varied the tight-binding (TB) hoppings and on-site energies in order to obtain the best agreement between the MT band structure (in agreement with experimental results) and the TB approximation. Here, we have also accounted for the overlap integrals in the TB calculation; orbital overlap between the s orbitals is denoted as s_{ss} , between the s and in-plane p orbitals as s_{sp} , and between in-plane p orbitals as $s_{pp\sigma}$ and $s_{pp\pi}$.

We have varied the TB parameters such that the MT and TB band structures agree as well as possible. In finding the best agreement, we focus on the lower bands, and allow for differences between TB and MT results for the higher p orbital bands. The MT and TB band structures and the corresponding designs are shown in Fig. S4.2. It can be seen that the s and p orbital bands of the experimentally studied lattices can be well approximated with a TB model with s and p orbitals only, except for the highest p band. The corresponding parameters are given in Table S4.1. Because there are 10 fitting parameters, this fit might not be unique. We would like to remark that the relative values of the main hopping parameters t_{ss} and $t_{pp\sigma}$ seem to be very reasonable, seen from a chemical orbital perspective. We show calculations for a lattice similar to the one studied previously by Gomes et al. [15], the two lattices that we have examined, and a lattice with a triple-ringed CO rosette. When the rosettes are enlarged, on-site quantum confinement increases the energy difference between the on-site s and p energy levels.

The increasing agreement between TB and MT with increasing confinement has several origins. First, orbitals higher than p are not incorporated in the TB model. The influence of these orbitals on the lower bands is not completely neglectable and is automatically taken into account in the MT calculations, but not in the TB calculations. Thus, the simple TB approximation becomes more accurate when the energy difference between the on-site energy levels increases. In addition, the s and p orbital bands become more pure when the on-site energy separation between the s levels and p levels increases. We were able to design artificial lattices that unambiguously show two separated Dirac cones and a flat band.

A second factor that improves the TB approximation is that for increasingly larger rosettes, the influence of the orbital overlap and $t_{pp\pi}$ hopping decreases. When $t_{pp\pi}$

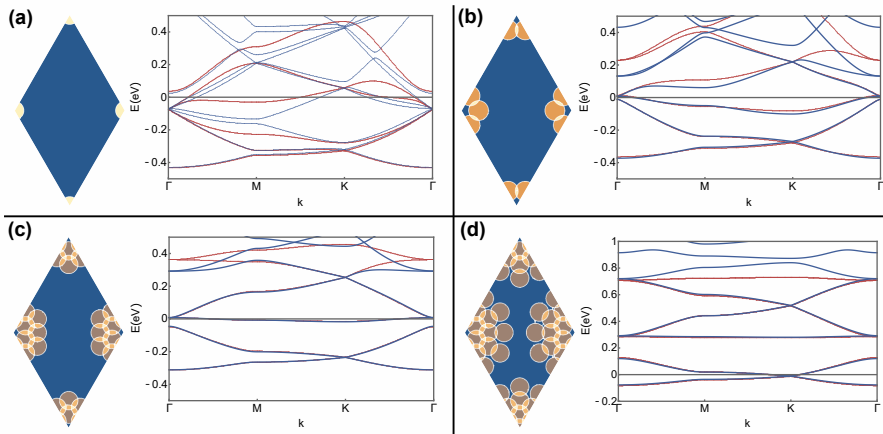


Figure S4.2: Fitting of the calculated muffin-tin band structures with a tight-binding model. Each panel contains a unit cell (blue diamond) of the corresponding lattice with CO molecules portrayed as brown discs. The corresponding band structures are shown next to it with the muffin-tin results in blue and tight-binding results in red. The tight-binding hopping and overlap parameters are presented in Table S3.1. (a) The lattice reported by Gomes et al. [15] with a single CO molecule as scatterer. (b) A lattice with single-ringed CO rosettes as scatterers. (c) A lattice with double-ringed CO rosettes as scatterers. (d) A lattice with triple-ringed CO rosettes (not experimentally studied).

becomes neglectable, the lowest and highest p orbital bands lose their dispersion and become genuine flat bands.

	t_{ss}	t_{sp}	$t_{pp\sigma}$	$t_{pp\pi}$	e_s	e_p	s_{ss}	s_{sp}	$s_{pp\sigma}$	$s_{pp\pi}$
single CO	-0.09	-0.09	-0.11	-0.11	-0.24	-0.075	0.06	0.06	0.15	0.15
single-ringed rosette	-0.07	-0.09	-0.105	-0.045	-0.22	0.105	0.06	0.07	0.2	0.1
double-ringed rosette	-0.062	-0.06	-0.1265	-0.00825	-0.22	0.185	0.1	0.1	0.05	0.05
triple-ringed rosette	-0.034	-0.05	-0.131	0	0.01	0.49	0.04	0.01	0.03	0.01

Table S4.1: Fitting parameters for the designs shown in Fig. S4.2 Units, where applicable are eV.

Results obtained on an artificial honeycomb lattice formed by single-ringed CO rosettes.

Figure S4.3 presents dI/dV vs. V spectra taken on the single-ringed CO rosette lattice, the design is shown in Fig. 4.1(b). We demonstrate the effect of the two normalization techniques shown in Fig. S4.6: subtraction (panel (b)) and division (panel (c)). In panel (a), in orange, we show an averaged spectrum taken on Cu(111), notice that this spectrum shows an increase in intensity above -0.2 V. This feature is also visible in the spectra taken on the atomic lattice sites (green) and bridge sites (purple). Subtraction of the dI/dV of the Cu(111) background partially corrects for this, but it is possible that features in the lattice LDOS remain clouded

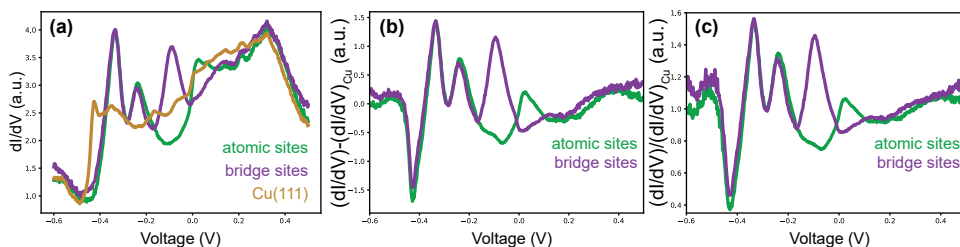


Figure S4.3: Effect of normalizing the raw spectra on an artificial honeycomb lattice formed by single-ringed CO rosettes by various techniques. The (dI/dV) vs. V spectra were acquired on the lattice presented in Fig. 4.1(b), formed by an anti-dot lattice of single-ringed CO rosettes. (a) Averaged spectra taken on two different symmetry positions in the lattice; on the center of the atomic lattice sites (green) and at bridge sites in between (purple). The surface state measured on bare Cu(111) is shown in orange. (b) The same spectra, but with the Cu(111) dI/dV background subtracted. (c) The same spectra but divided by the Cu(111) dI/dV .

above 0.1 V.

In the region below 0.2 V, the bare and normalized spectra obtained on this lattice show clear features corresponding to the LDOS of the artificial lattice. The two peaks at -330 and -210 mV are assigned to the s orbital Dirac cone, more specifically to the M points around the Dirac point at -290 mV at K (see also main text). The strong feature at -0.1 V measured at the bridge sites reflects the p orbital flat band. The results are similar to those obtained with a lattice created with double-ringed CO rosettes. The large dip in intensity at -0.4 V corresponds to a normalization artefact and has no relevance for the band structure.

The spatial distribution of the LDOS over the lattice is presented in Fig. S4.4. At -330 mV, the LDOS intensity is strong on the lattice sites. The LDOS intensity is minimal at the Dirac point at -290 mV. At the second peak of the Dirac cone, at -210 mV, the intensity is high again on the lattice sites. The muffin-tin calculations reproduce the experimental maps well.

Figure S4.4 shows that there is a strong resonance peak at -90 mV for the bridge sites. This peak is absent on the atomic sites. Comparison with our muffin-tin and tight-binding calculations show that this peak reflects the p orbital flat band (see main text). The spatial distribution of the LDOS shows the remarkably strong intensity of the LDOS between the atomic sites, in full agreement with the results obtained on the other artificial lattice presented in the main text. Although the spectra are not very different around 70 mV, we observe patterning throughout the lattice in the LDOS maps. This pattern corresponds to measurements taken on the double-ringed CO rosette lattice.

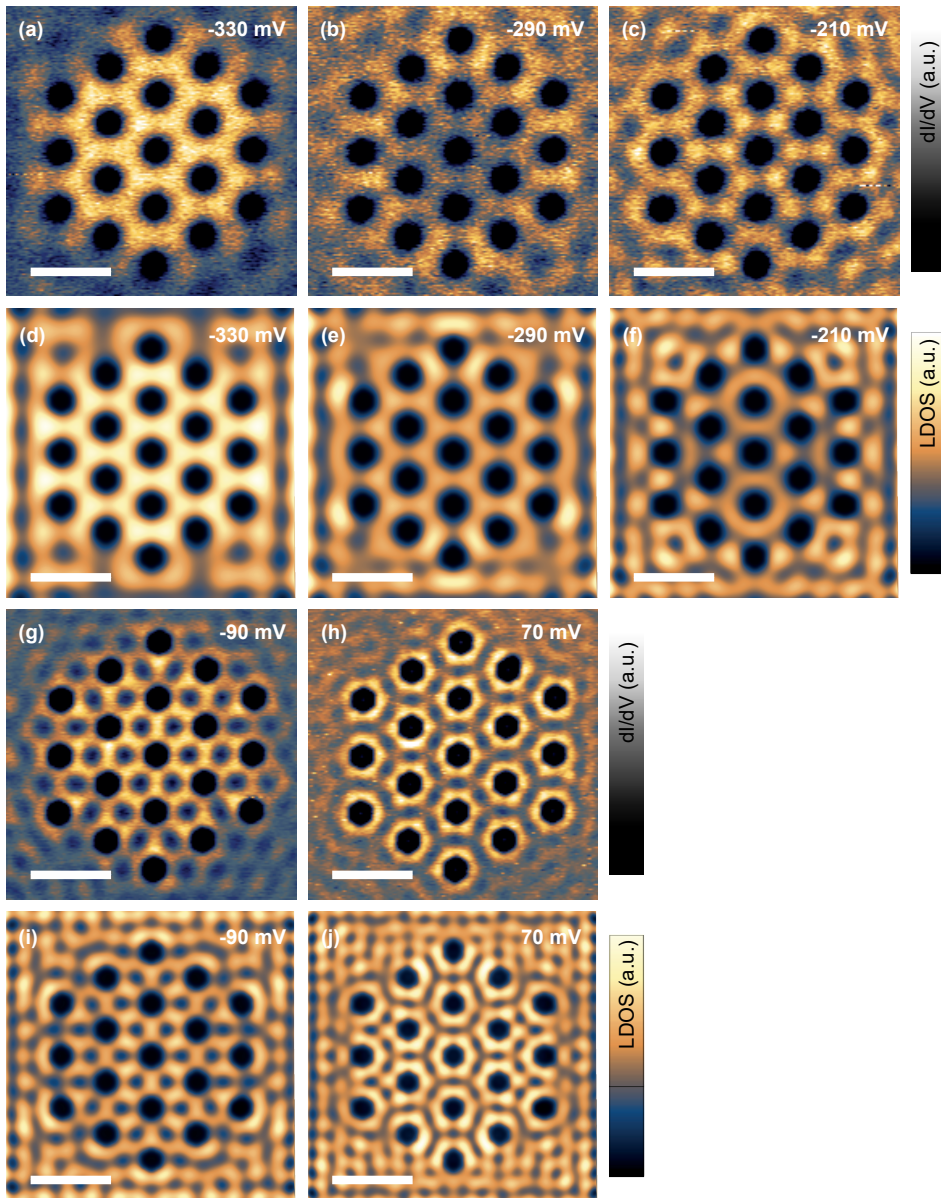


Figure S4.4: Electron probability maps obtained on an artificial honeycomb lattice formed by single-ringed CO rosettes. (a-c) LDOS maps corresponding to the s orbital Dirac cone taken at the first maximum at -330 mV, the Dirac point at -290 mV and the second maximum at -210 mV. The maxima reflect the M points of the Dirac cone. (d-f) Corresponding muffin-tin calculations for the electron probability corresponding to the maps in (a-c). (g) LDOS map corresponding to the p orbital flat band at -90 mV, showing zero intensity on the lattice sites and very strong intensity in between the sites. (h) LDOS map corresponding to higher energy p orbital bands at $+70$ mV. (i, j) Corresponding muffin-tin calculations for the electron probability corresponding to the maps in (g, h), respectively. Scale bars are 5 nm.

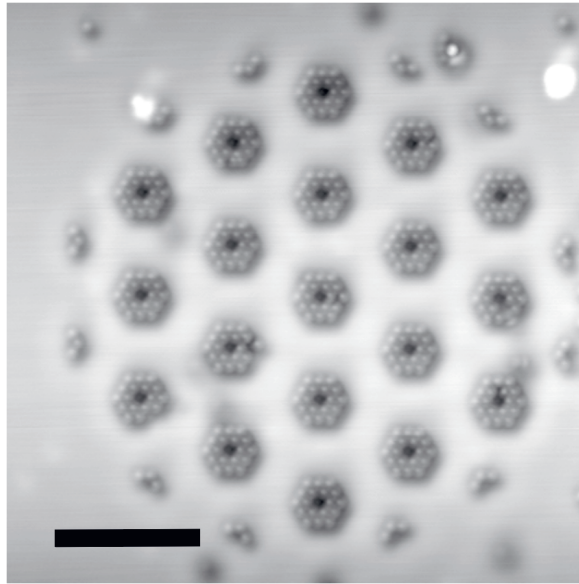


Figure S4.5: Detailed structure of the CO rosettes used to prepare artificial electronic lattices. Constant current STM image of a honeycomb lattice with a lattice vector of 3.86 nm. The potential landscape is obtained by using double-ringed CO rosettes as repulsive scatterers for the surface state of the underlying Cu(111) surface. The purpose is to form artificial atomic sites located between the repulsive rosettes. This image was obtained with a CO-terminated tip. Each double-ringed rosette consists of 18 CO molecules, which are imaged as circular protrusions. Several defects or misplaced CO molecules can be spotted. Scale bar is 5 nm.

The structure of an artificial honeycomb lattice created by rosettes of CO scatterers imaged with a CO tip.

The artificial honeycomb lattices studied in this work are prepared by creating a potential energy landscape to force the electrons of the Cu(111) surface state into a honeycomb geometry. The potential energy landscape is obtained by placing repulsive CO molecules acting as scatterers in rosettes, e.g. see Fig. 4.2. Fig. S4.5 presents a specific lattice imaged with a CO tip, allowing us to discern the individual CO molecules (absorbed on top of Cu atoms) as circular protrusions in each rosette, and even misplaced CO molecules. Please, also notice that we have placed CO scatterers around the lattice to isolate the lattice from the rest of the Cu(111) surface state.

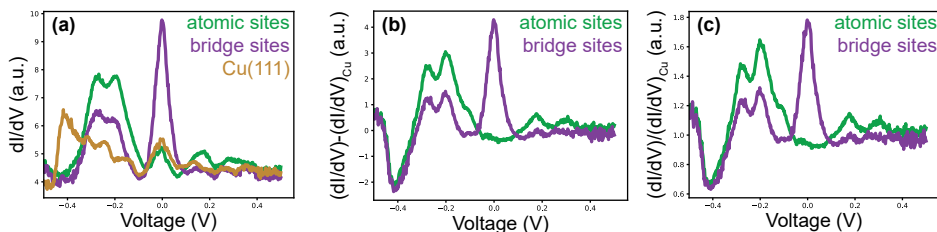


Figure S4.6: Effect of normalizing the raw spectra by various techniques. The (dI/dV) vs. V spectra were acquired on the lattice presented in Fig. 4.2(a), formed by an anti-dot lattice of double-ringed CO rosettes. (a) Averaged spectra taken on two different symmetry positions in the lattice; on the center of the atomic lattice sites (green) and at bridge sites in between (purple). The surface state measured on bare Cu(111) is shown in orange. (b) The same spectra, but with the Cu(111) dI/dV background subtracted. (c) The same spectra but divided by the Cu(111) dI/dV .

Effect of normalizing the raw spectra by various techniques

In order to correct for the effects from the Cu sample and Cu tip, all dI/dV vs. V spectra in this manuscript have been presented as normalized spectra. This was done following a method used by Gomes et al. [15]. The raw spectra were divided by an averaged dI/dV obtained on a bare Cu(111) surface, acquired with exactly the same settings and the same tip. This procedure should remove LDOS components of the tip and the Cu(111) sample. The normalization technique is the same as shown in 4.4. For the two different tip states and lattices the normalization provides reproducible results, a good indication that our normalization technique is sound.

In Fig. S4.6 we demonstrate the effect of two different normalization techniques. In panel (a) we show the raw spectra taken on bare Cu(111), and on lattice sites and bridge sites. First, the effect of quantum confinement in the lattice can be seen by the onset of resonances at higher energy than the onset of the bare surface state. Second, one can already see the peaks and valleys of interest in the spectra taken on the two positions in the lattice. However, the spectral intensities of the lattice should be corrected for the background related to substrate and tip. In panel (b), we subtracted the dI/dV of the Cu(111); a horizontal line through zero would form a reference. In panel (c) we divided the raw spectra by the Cu(111) background spectra; thus a horizontal line through 1 would now form a reference. The spurious peak at 0V (green line) is absent in both cases. The procedure shown in (c) is the procedure used to represent the LDOS in the main text.

Analytic tight-binding model for the electronic honeycomb lattice in the absence of hybridization, broadening and orbital overlap.

DOS and spatially-resolved LDOS maps in the s sector

We have calculated the local density of states $LDOS(E, \mathbf{r})$ in the absence of broadening, at energy E and position \mathbf{r} using

$$LDOS(E, \mathbf{r}) = \sum_{\mathbf{k}, \alpha} |\Psi_{\mathbf{k}, \alpha}(\mathbf{r})|^2 \delta(E - E_{\mathbf{k}, \alpha}) \quad (4.4)$$

where $\Psi_{\mathbf{k}, \alpha}(\mathbf{r})$ is a state in band α , with lattice momentum \mathbf{k} , and energy $E_{\mathbf{k}, \alpha}$. Due to the presence of the delta function, the $LDOS(E, \mathbf{r})$ can be rewritten as an integral over a constant-energy path in the Brillouin zone of the honeycomb lattice.

In the absence of s - p hybridization, the energy bands in the s sector are given by [122]:

$$E_{\mathbf{k}, \pm} = \pm t_{ss} |u(\mathbf{k})| \quad (4.5)$$

where the zero of energy is set at the Dirac point, t_{ss} is the hopping between nearest-neighbor s orbitals, and $u(\mathbf{k})$ is defined as $\sum_{j=1}^3 e^{i\mathbf{k} \cdot \delta_j}$, with the vectors δ_j pointing to nearest neighbors of a site. By symmetry, the weight of each eigenstate $\Psi_{\mathbf{k}, \alpha}(\mathbf{r})$ is the same on the two Bloch waves formed by the s orbitals on the sublattices A and B. However, the phase between the two contributions differs by the angle $\theta_{\mathbf{k}} = \text{Arg}u(\mathbf{k})$. Since $E_{\mathbf{k}, \pm}$ does not depend on $\theta_{\mathbf{k}}$, the phase can be seen as a pseudo-spin degree of freedom. [97]

Figure S4.7(a) depicts constant-energy paths in the Brillouin zone. Close to zero energy, since the allowed states form cones around (K, K') , the paths consists of tiny (blue) circles, as shown at $E = \pm 0.2t_{ss}$. The radius of the circles goes to zero at the Dirac point where the DOS vanishes. At increasing energy from the Dirac point, the constant-energy path tends to deviate from the circular shape. For $E = \pm t_{ss}$, the constant-energy path becomes a hexagon that touches the edge of the Brillouin zone at the M points. This leads to a maximum of the LDOS at these energies. In this simple model, in which hybridization with p orbitals is excluded and the overlap integral is neglected, the distance in energy between the two peak maxima in the $LDOS(E)$ plot of the s bands is equal to $2|t_{ss}|$. This is used in the main text for a first estimation of $|t_{ss}|$. This value can be compared with the value obtained from a tight-binding model by fitting the 6 lowest bands (s and p bands), including s - p hybridization, and taking the overlap integrals into account.

Spatially-resolved LDOS maps are obtained by integration of $|\Psi_{\mathbf{k}, \alpha}(\mathbf{r})|^2$ on the constant-energy paths (Fig. S4.7(a)). In a tight-binding representation with one s orbital $\phi_s(\mathbf{r} - \mathbf{R}_i)$ on each site \mathbf{R}_i , the LDOS for any allowed energy E close to the Dirac point is just the superposition of the squared s orbitals, i.e., $\sum_i |\phi_s(\mathbf{r} - \mathbf{R}_i)|^2$. The extra terms in $|\Psi_{\mathbf{k}, \alpha}(\mathbf{r})|^2$, which come from the cross terms between nearest-neighbor s orbitals, cancel out after integration over constant-energy paths because they are proportional to $\cos(\theta_{\mathbf{k}})$. This is one explanation for the experimental results

presented in Fig. 4.2: the two peaks reflecting the high density of states at the M points of the s orbital Dirac cone are nearly symmetrical in intensity, when measured on atomic sites (green curve in Fig. 4.2(b)) and on bridge sites (purple curve in Fig. 4.2(b)). This also explains the experimental LDOS maps of Fig. 4.2(c) and (e), with high intensities on the atomic sites and weaker intensity between the sites. However, in Fig. S4.8 we do not see the same symmetry effect. This can be understood as a consequence of the contribution of the energies far away from the Dirac point, where the approximation explained above is not valid. The symmetric density of states on the bridge sites can alternatively be explained by the influence of s - p hybridization in the highest s orbital that is not taken into account in Fig. S4.8.

DOS and spatially-resolved LDOS maps in the p sector

The four energy bands (Fig. S4.7(b)) in a pure p_x, p_y model (no s - p hybridization) with negligible π coupling are given by

$$\begin{aligned} E_{\mathbf{k},1} &= -\frac{3}{2}t_{pp\sigma} & E_{\mathbf{k},4} &= -E_{\mathbf{k},1} \\ E_{\mathbf{k},2} &= -\frac{1}{2}t_{pp\sigma}|u(\mathbf{k})|^2 & E_{\mathbf{k},3} &= -E_{\mathbf{k},2} \end{aligned} \quad (4.6)$$

where $t_{pp\sigma}$ is the hopping term of σ type between nearest-neighbor p orbitals [99, 101]. The second and third bands have the same dispersion as the s orbital bands, provided that t_{ss} is replaced by $\frac{t_{pp\sigma}}{2}$. The description with constant-energy paths, shown above, remains valid after this substitution. In particular, the DOS vanishes at zero energy (Dirac point) and presents a maximum at $E = \pm \frac{t_{pp\sigma}}{2}$, when the constant-energy paths form a hexagon connecting the M points of the Brillouin zone. The first and fourth bands in this p_x, p_y model are totally flat, giving rise to the DOS in the form of Dirac delta functions at $E = \pm 3\frac{t_{pp\sigma}}{2}$ in absence of extra sources of broadening or dispersion (absence of π bonding or s - p hybridization).

Comparison between the band structure for the pure p_x, p_y model (Fig. S4.7(b)) and the band structure calculated by solving the Schrödinger equation with a muffin-tin potential (Fig. 4.1(f)) shows that the lowest flat band and the p orbital Dirac cone are well distinguishable in the muffin-tin results and in the experimental LDOS spectra. The main differences appear in the upper part of the band structure due to strong coupling with higher-energy orbitals. This leads to a down shift of the dispersive band $E_{\mathbf{k},3}$, especially at the Γ point. In addition, the upper band $E_{\mathbf{k},4}$ is not flat anymore. It is thus wise to use the lowest bands to estimate the value of $t_{pp\sigma}$ from the experimental LDOS results, Fig. S4.7(b) and the values given in the main text.

Whereas the LDOS maps close to the Dirac point do not depend on energy in the s orbital model, the situation is totally different in the p orbital model due to the orbital degree of freedom [99, 101]. The orbital configuration on each site strongly varies with \mathbf{k} , explaining the remarkable patterns that were observed and presented in Fig. 4.3. In the case of the flat bands, the eigenstates $\Psi_{\mathbf{k},\alpha}(\mathbf{r})$ can be written either in terms of Bloch states or, alternatively, as a linear superposition of Wannier-like localized states, which are all degenerate. One localized state exists per hexagonal plaquette [99, 101]. The configuration in terms of p orbitals for the lowest flat

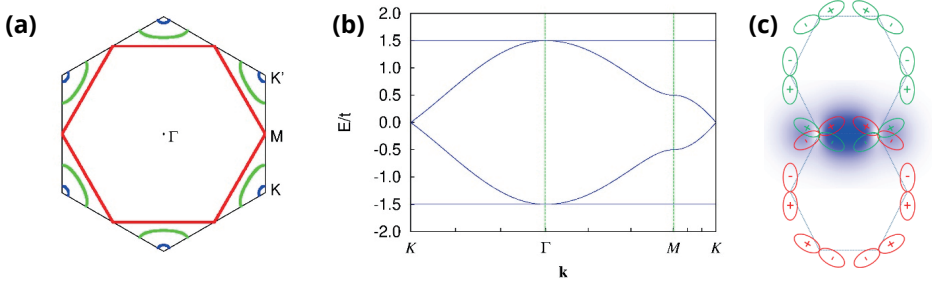


Figure S4.7: Tight-binding analysis without hybridization. (a) Constant-energy paths in the Brillouin zone of the honeycomb lattice for different energies around the Dirac points at (K, K) . Blue cones around (K, K) : $E = \pm 0.2t_{ss}$, green curves around (K, K) : $E = \pm 0.7t_{ss}$, red hexagon $E = \pm t_{ss}$ (b) p Orbital band structure for a tight-binding model with in-plane $p_{x,y}$ orbitals in a honeycomb lattice, in absence of π coupling ($t_{pp\pi} = 0$) and hybridization. The energies are given in units of $t_{pp\sigma}$. (c) Localized eigenstates for the lowest flat band in two neighboring hexagons (red and green colors, respectively). The sum of the squared amplitude of these two eigenstates is shown along the bond common to the two hexagons.

band is depicted in Fig. S4.7(c) (see also Fig. 4.4). One p orbital is tangential to the hexagon; as a consequence, the other p orbital on the same site is then parallel to the bond external to the hexagon. The flatness of the band is explained by the cancellation of hopping terms to neighboring loops (interference effect) in absence of π bonding. In this configuration, the LDOS map on nearest-neighbor atoms A and B is given by the squared amplitude of the two localized eigenstates that share this bond. Fig. S4.7(c) presents the summed amplitude calculated using a p_x orbital of the form $x \cdot e^{-\frac{|x|}{\gamma}}$, where $\gamma = 0.25a$, a being the lattice vector (same definition for p_y). It can be seen that the LDOS amplitude is very high at the center between two adjacent sites of the hexagon, in agreement with the experimental results and the muffin-tin calculation, see main text.

Calculation of the LDOS(E) spectra by using the tight-binding approximation.

Using the tight-binding model, we can obtain the eigenvectors corresponding to each energy $E_n(k)$ in the band structure, where n denotes the band number. This gives the wave function distribution over the orbitals and sublattice sites for that energy. We approximate the s orbitals as normalized Gaussians $Ae^{-\frac{x^2}{r}}$, the p orbitals as $Be^{-\frac{x^2}{r}} \sin \phi$ for the p_y orbital and $Be^{-\frac{x^2}{r}} \cos \phi$ for the p_x orbital, where A and B are normalization constants, r is proportional to the lattice size, $r = \frac{\sqrt{3}}{10}a$, with a the lattice spacing, and ϕ the angle with respect to the horizontal axis. Using this approximation, we can calculate the wave function $\Psi(x, y)_{E_n(k)}$. If we now wish to calculate the LDOS for an energy E , we can sum $\Psi(x, y)_{E_n(k)}$ over n and a (dense enough) k grid, where each contribution is weighted by the broadening

$L[E_n(k) - E]$. Here $L(x)$ is given by $\frac{b}{[x^2 + (\frac{b}{2})^2]}$ with b the broadening of 0.04 eV.

In Fig. S4.8, the resulting maps and spectra are shown for a simple tight-binding model. On the lattice sites, the *s* orbital Dirac cone is manifest, but the *p* orbital bands have nearly zero intensity due to the nodal planes. The *p* orbital flat bands and the *p* orbital Dirac cone are mostly localized on the bridge sites. In this tight-binding calculation, no *s-p* hybridization or $t_{pp\pi}$ are taken into account, the overlap integrals (which are small compared to the hoppings, see Table S3.1, have been neglected.

Differential LDOS conductance maps acquired for the lattice of Fig. 4.2 in the energy region of the *p* orbital Dirac cone.

The spatial patterns in the energy region of the *p* orbital Dirac cone are very detailed and typical (Fig. S4.9(a, b)). There is high intensity close to the rosettes, very weak intensity on the sites and even weaker intensity between the sites. As a guide to the eye, a scheme is presented in Fig. S4.9(c) where the CO rosettes are left uncolored for clarity. At the Dirac point, the rings of high intensity around the rosettes are nearly uniform. For both peaks (M points) around the Dirac point, the high intensities form trigonal arrays around each artificial site.

Comparison of the experimental results obtained on the artificial lattice with double-ringed rosettes (Fig. 4.1(c)) with the muffin-tin calculations.

Figure S4.10 shows a comparison between experimental results and muffin-tin calculations. Overall, an excellent agreement is found between experimental and theoretical LDOS maps for the energy region with the *s* orbital Dirac cone and *p* orbital flat band, and a reasonable agreement for the region of the *p* orbital Dirac cone.

First row: Experimental spectra (left) and the muffin-tin calculations (right). The numbers are related to the LDOS maps below. Notice that the orange spectrum (close to the rosettes) was taken with a different tip. Peaks 1-5 are at the same position, but have a slightly different relative intensity. This can either be due to a remaining effect of the tip change, but could, in our view, also be caused due to the fact of the very close proximity of the position of measurement to the CO rosette. Insert: A sketch of the locations at which the spectra were taken.

Second and third row: Experimental electron probability (LDOS) maps acquired at constant-heights at the spectral features (numbers 1-7). The intriguing LDOS map at the flat band (point 4) has been summarized in a sketch that emphasizes the high electron density (yellow) between the artificial sites (grey circles on the hexagon). The high intensity regions between the sites form plaquettes around each hexagon of the honeycomb lattice.

Fourth and fifth row: LDOS maps calculated with the muffin-tin model. The maps

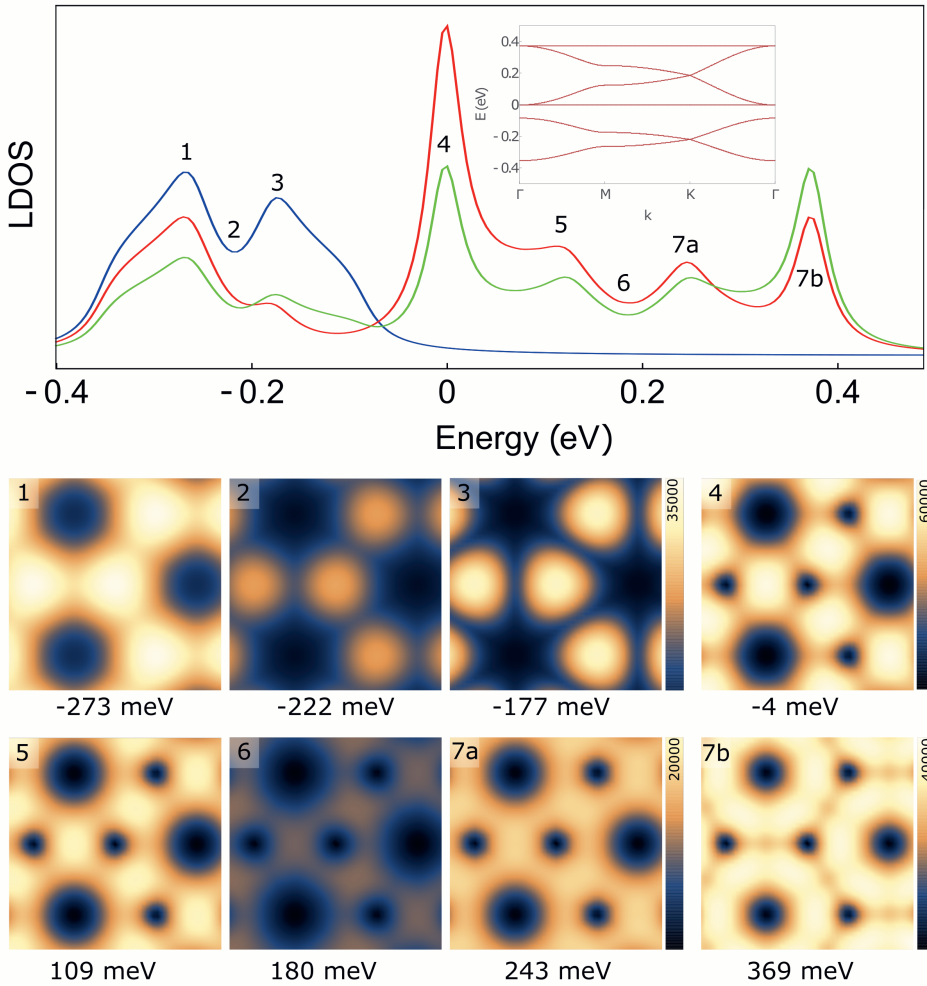


Figure S4.8: Tight-binding analysis of the spectra, band structure and wave function maps of a periodic system for the lattice with the double rosettes. (Top) Spectra are shown for three positions in the lattice: artificial atomic sites (blue), bridge sites (red) and very close to a CO rosette (green). Inset shows the band structure. (Bottom) LDOS maps corresponding to the interesting features in the spectra with no orbital overlap, s - p hybridization or $t_{pp\pi}$.

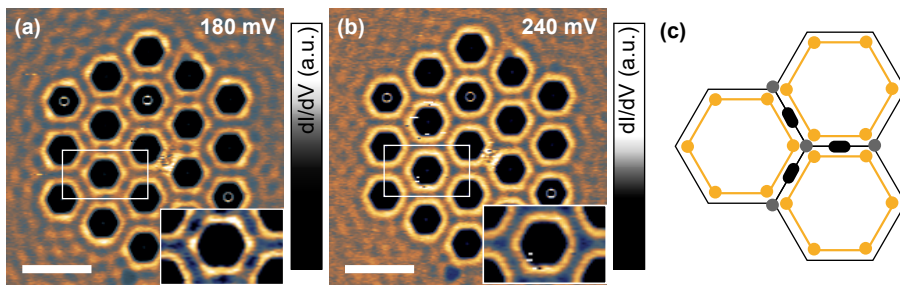


Figure S4.9: Differential LDOS conductance maps acquired for the lattice of Fig. 4.2 in the energy region of the p orbital Dirac cone. (a) Electron probability map taken at 180 mV (lower energy maximum of p orbital Dirac cone). The atomic sites have a low intensity while the bridge sites have an even lower intensity. The rings of high intensity around the CO rosettes show a modulation in the intensity as well. (b) Electron probability map taken at 240 mV (p orbital Dirac point). The atomic sites have a low intensity while the bridge sites have a slightly higher intensity. The insets show an enlargement. Scale bar is 5 nm. (c) Scheme of the intensities around an artificial site for the region of p orbital Dirac cone. The artificial site has low intensity (light grey), the bridge sites have even lower intensity (dark grey). Each rosette is circumvented with high LDOS intensity, resulting in a triangle of high intensity around each artificial site.

1-4 are in excellent agreement with the corresponding experimental results. The calculated maps 5 and 6 (first peak of the p orbital Dirac cone and Dirac point) show intricate and rapid oscillations in intensity that differ from those in the experimental spectrum; in addition, the calculated overall intensity is much weaker than observed experimentally. In contrast, the calculated LDOS map 7, at the second peak of the Dirac cone, is in very reasonable agreement with the experimental result shown at 330 mV. As in our muffin-tin approach, the CO's are modeled as vertical potential barriers, the muffin-tin results in close proximity to the CO barriers become less accurate. For convenience, the detailed LDOS pattern found in the region of the p orbital Dirac cone is sketched again. The regions of high intensity are indicated in yellow. Each artificial atom (grey circle) is surrounded by three regions of high intensity (yellow disks) and with three regions of very low intensity (black regions at bridge sites). The regions of high intensity (yellow) form hexagonal plaquettes. The low intensity regions (bridge sites) form plaquettes around each hexagon of the honeycomb lattice. The scale bars are 5 nm.

A check of the uniformity of the LDOS across the artificial lattice of Fig. 4.2 by differential conductance spectra acquired along lines in the lattice.

To check that the LDOS measurements are similar throughout the entire lattice, we obtained many spectra along a line to visualize the uniformity (Fig. S4.11). Periodic intensity plots show the strong reproducibility of the LDOS on different sites across

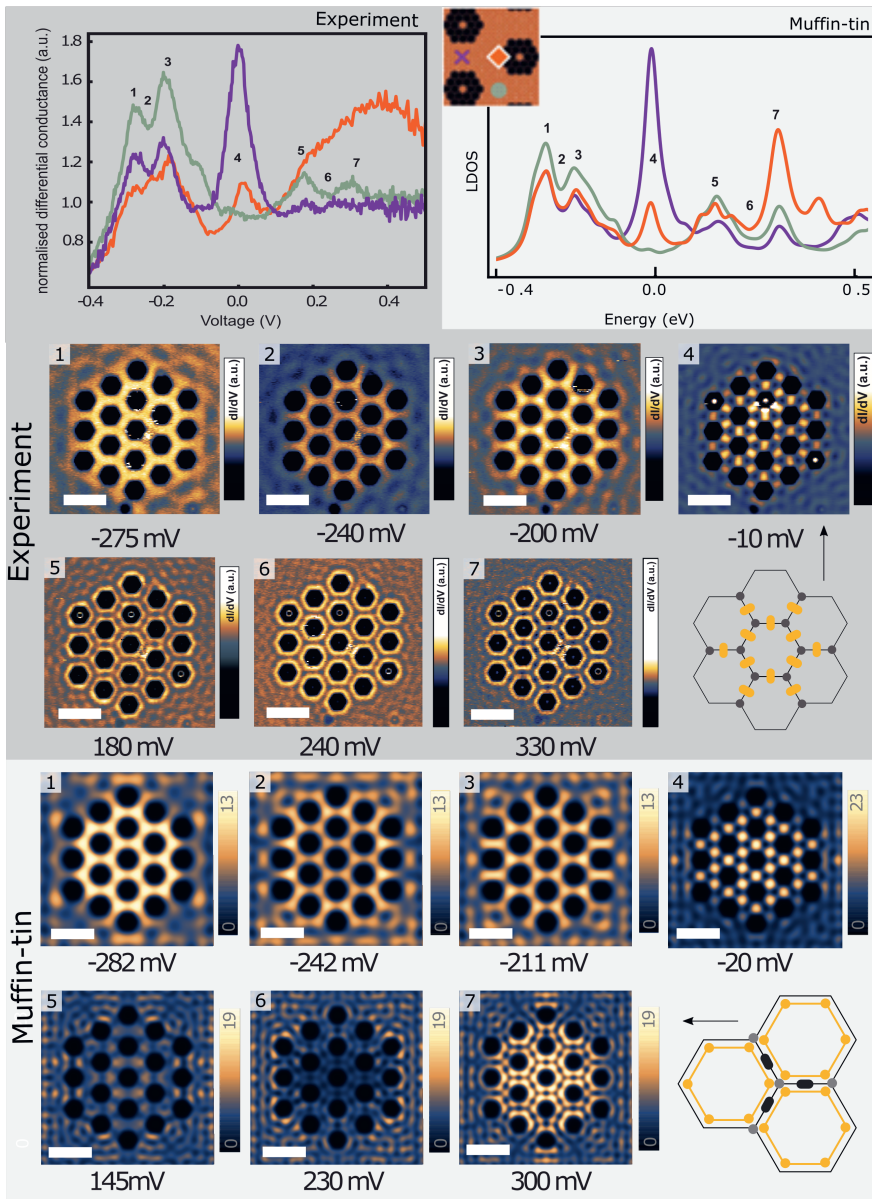


Figure S4.10: Comparison of the experimental results obtained on the artificial lattice with double-ringed rosettes (Fig. 4.1(c)) with the muffin-tin calculations.

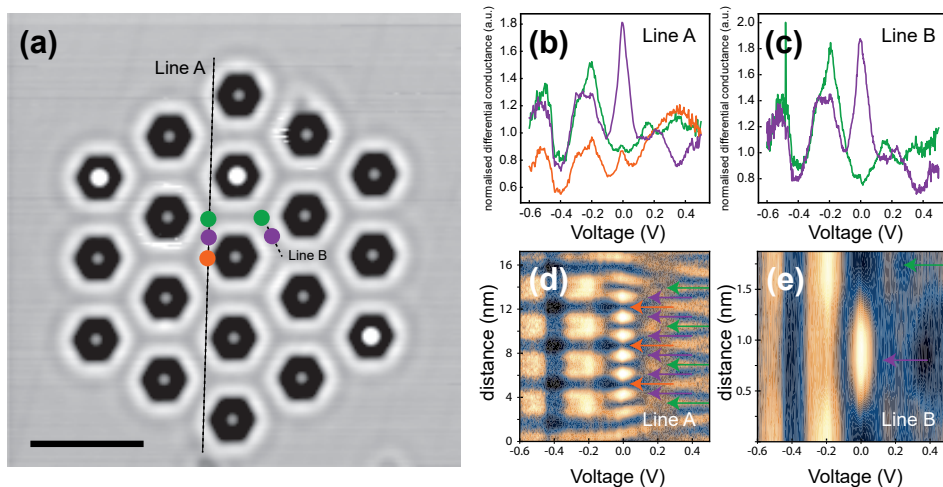


Figure S4.11: A check of the uniformity of the LDOS across the artificial lattice of Fig. 4.2 by differential conductance spectra acquired along lines in the lattice (a) An STM image of the lattice with two dashed black lines indicating the line traces along which spectra were taken. 100 spectra were taken along line A, consecutively on the green lattice sites, the violet positions between the lattice sites, and orange positions closer to the CO rosettes. On line B 15 spectra were taken on green and violet sites. The scale bar is 5 nm. (b, c) Individual representative spectra taken on lines A and B, respectively. (d, e) Colored LDOS intensity plots obtained from all 100(15) spectra taken on line A(B), respectively, presented in a (line position – bias) frame. The arrows indicate the locations corresponding to the colored locations in panel (a).

the lattice. At 0 V, the high intensity on bridge sites reflecting the p orbital flat band is reproducibly observed. The orange sites closer to the rosettes show high intensity above 0.2 V due to the peaks of the p orbital Dirac cone, in line with the maps presented in the main text, Figs. 4.3, 4.4.

Three-dimensional $E(k_x, k_y)$ diagram of the band structure of the artificial lattice in Fig. 4.1(c).

For the experimentally realized design presented in Fig. 1(c), we show a three-dimensional representation of the band structure in Fig. S4.12.

Contrast of the CO rosettes at positive bias.

The contrast of the differential conductance maps shown in the main text can be adjusted such that the internal contrast of the CO rosettes is more visible. Figure S4.13 shows two dI/dV maps (+150 mV and +330 mV) with an adjusted colour scale. The central missing CO molecule shows up as brighter spots.

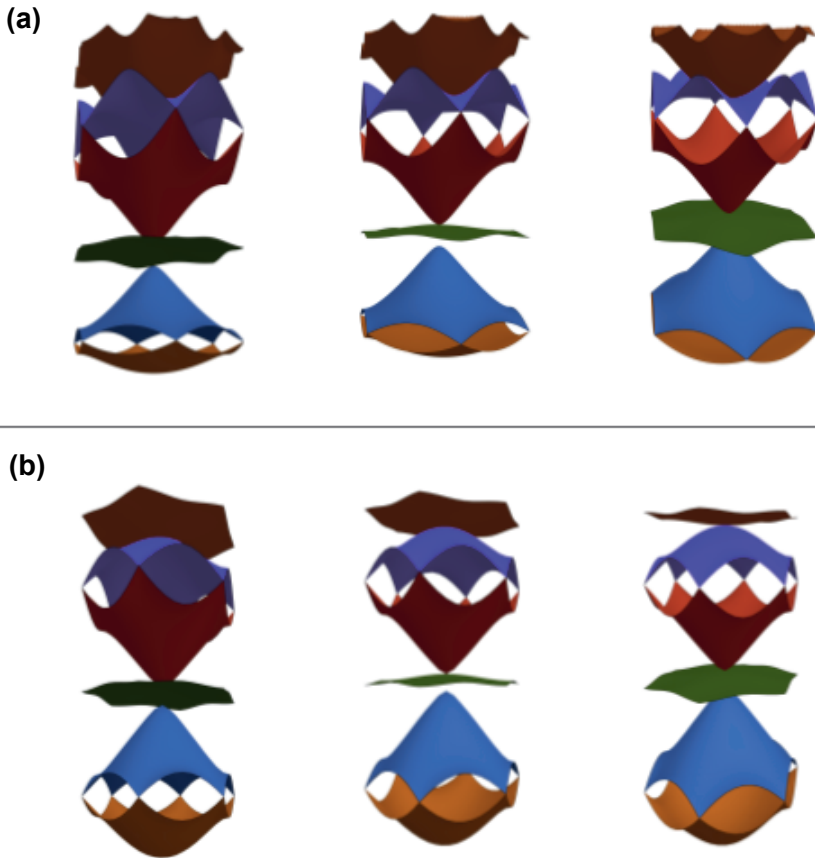


Figure S4.12: Three-dimensional $E(k_x, k_y)$ diagram of the band structure of the artificial lattice in Fig. 4.1(c). (a,b) Three $E(k_x, k_y)$ diagrams at various viewing angles of the band structure corresponding to the double-ringed rosette lattice calculated with the muffin-tin (a) and tight-binding (b) approach.

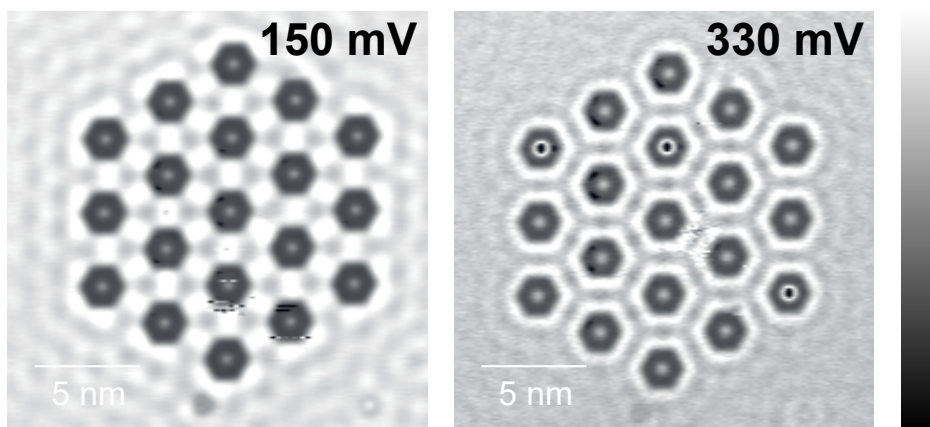


Figure S4.13: Two differential conductance maps taken at positive bias showing the internal contrast of the CO rosettes.

Spin-orbit gaps in the s and p orbital bands of an artificial honeycomb lattice

This chapter is partially based on the following publication:

J. J. van den Broeke, I. Swart, C. Morais Smith & D. Vanmaekelbergh, *Spin-orbit gaps in the s and p orbital bands of an artificial honeycomb lattice*, **arXiv preprint**, arXiv:2104.06912 (2021)

Muffin-tin methods have been instrumental in the design of honeycomb lattices that show, in contrast to graphene, separated s and in-plane p bands, a p orbital Dirac cone, and a p orbital flat band. Recently, such lattices have been experimentally realized using the 2D electron gas on Cu(111). A possible next avenue is the introduction of spin-orbit coupling to these systems. Intrinsic spin-orbit coupling is believed to open topological gaps, and create a topological flat band. Although Rashba coupling is straightforwardly incorporated in the muffin-tin approximation, intrinsic spin-orbit coupling has only been included either for a very specific periodic system, or only close to the Dirac point. Here, we introduce general intrinsic and Rashba spin-orbit terms in the Hamiltonian for both periodic and finite-size systems. We observe a strong band opening over the entire Brillouin zone between the p orbital flat band and Dirac cone hosting a pronounced edge state, robust against the effects of Rashba spin-orbit coupling.

5.1 Introduction

Ever since the prediction of the quantum spin Hall effect in graphene as a result of intrinsic spin-orbit coupling by Kane and Mele [2], efforts have been made to observe the predicted state. Not only would the intrinsic spin-orbit coupling turn graphene into a bulk insulator, it would also create conducting edge modes that would be protected from scattering by the topology of the system [2]. Unfortunately, the gap turned out to be too small for practical applications [3]. Although efforts have been made to enhance the intrinsic spin-orbit coupling [5, 123], no convincing method has been found so far. An alternative pathway to create lattices with robust quantum spin Hall edge states would be to lithographically pattern quantum wells from heavy element semiconductor compounds such as GaAs [14] and GaInAs [12]. However, these lattices still suffer from geometric disorder. Meanwhile, the effects of intrinsic spin-orbit coupling can be studied in artificial lattices, created by placing energy barriers on top of a (heavy) metal with a 2D electronic surface gas using a scanning tunnelling microscope. This method was pioneered by Gomes et al. [15] using CO molecules as energy barriers on top of Cu(111), to create a triangular array of scatterers, resulting in an effective honeycomb potential for the surface state electrons. The potential landscape can be thought of as an artificial lattice of coupled quantum corrals, i.e. artificial atoms, that have one s and two (in-plane) p

orbitals. If s - p hybridization is absent, the coupling between the sites in the lattice results in an s orbital Dirac cone and 4 p bands. In Ref. [15], only the lowest two bands were considered, forming a Dirac cone (c.f. the bands derived from the $2p_z$ orbitals in graphene). Later, Gardenier et al. [28] extended the method: The size of the atomic sites was increased to bring the p band system in the accessible energy window of the Cu(111) surface state [53]. Additionally, by using CO rosettes instead of single COs s - p hybridization could be avoided to a large extent, resulting in two s - and four p orbital bands. The p orbital bands include a Dirac cone and a flat band [28], which was considered by tight-binding methods [24, 70, 71, 77, 99, 101].

The system of in-plane p orbital bands is of high interest to study the effects of intrinsic spin-orbit coupling. Not only is the effect of the coupling shown to be larger in these systems [70, 71, 124] because it is onsite instead of next-nearest neighbour, as would be the case for s and p_z orbitals, but it is also predicted to generate topological flat bands [24]. Flat bands are particularly interesting to study interactions, as the kinetic energy is quenched. Thus, interaction driven phenomena like superconductivity and charge density waves become accessible. Moreover, flat bands can be even more interesting when they are topological [25]. Thus, introducing intrinsic spin-orbit coupling in artificial electron lattices could open up exciting new possibilities for the field.

Patterned lattices are usually described as a two-dimensional (2D) free-electron gas confined to the lattice using a modulated (muffin-tin) potential. This muffin-tin method has yielded remarkably accurate predictions for effectively spinless systems, and has proven to be a vital tool in the design of artificial electronic lattices [12, 18, 28, 29, 55, 61, 88]. For these systems, the muffin-tin approach is often more convenient than the tight-binding method because there are only a few parameters involved, namely the potential landscape $V(x, y)$ and the electron effective mass. These parameters only have to be determined once for a material and patterning technique, whereas the tight-binding approach requires new fitting for each design. The muffin-tin method has the additional advantage that it does not require any assumption about the orbital character of the system. It can be complemented with a tight-binding parametrization, enabling one to understand which lattice orbitals are involved in the band formation. Besides this, the muffin-tin method is also well suited for finite-size calculations, and thus very useful for the study of edge states in practical systems.

Unfortunately, the inclusion of intrinsic spin-orbit coupling in muffin-tin models is not straightforward. The theoretical approaches proposed so far vary substantially [124, 125], and are only valid for a specific setup or only describe the physics near the Dirac point. In addition, these techniques are not easily extended to finite-size calculations.

Here, we propose a heuristic method that uses text book spin-orbit Hamiltonian terms, the magnitude of which depend on two input parameters, one for the intrinsic spin-orbit coupling, and one for the Rashba coupling. We reproduce the defining features of other approaches that use ab-initio derived expressions to account for spin-orbit coupling. Additionally, this method allows for calculations on finite size systems, crucial for the study of protected edge states.

The outline of this paper is the following: in Sec. 5.2, we review the muffin-tin

model and adapt it to incorporate Rashba and intrinsic spin-orbit coupling. We then investigate the influence of spin-orbit coupling on a honeycomb toy model in Sec. 5.3, and present our conclusions in Sec. 5.4.

5.2 The model

Let us consider an artificial lattice, created by adatoms arranged to form an anti-lattice confining the surface state electrons into the honeycomb geometry. These confined electrons can be described by the one-electron time-independent 2D Schrödinger equation,

$$\left(\frac{-\hbar^2}{2m^*} \nabla^2 + V \right) \Psi = E\Psi, \quad (5.1)$$

where m^* is the effective mass and V is the potential created by the adatoms patterning the surface. Thus, the only freedom in the input parameters is in the shape of the potential. When modeling a patterned potential $V(x, y)$ as a collection of disk shaped protrusions, also called a muffin-tin potential, only two parameters remain, namely the disk height and the disk width.

In order to study the effect of spin-orbit coupling in artificial lattices, we start with the spin-orbit coupling that originates from the Dirac equation as a relativistic correction to the Schrodinger equation, given by

$$H_{SO} = \frac{\hbar}{4m^2c^2} (\nabla V^* \times \mathbf{P}) \cdot \sigma, \quad (5.2)$$

where m is the real electron mass, V^* is the full potential, \mathbf{P} is the vector momentum, σ is the vector of Pauli matrices, and c is the speed of light. Here, we see that spin-orbit coupling is proportional to the gradient of the potential V^* . The Rashba spin-orbit coupling originates from Eq. (5.2) at the surface of materials, due to the large change in the potential at the interface. As inversion symmetry is not present, spin degeneracy is not required and is indeed broken. The Rashba term for a 2D electron system with a potential change in the out-of-plane direction has been derived before, see Refs [126, 127], and reads:

$$H_R = \alpha_1 (p_x \sigma_y - p_y \sigma_x). \quad (5.3)$$

Here, p_i ($i = x, y$) is the momentum component, σ_i are the Pauli matrices, and α_1 is the effective strength of the Rashba coupling. As a check, we add this term to Eq. (5.1), and use α_1 and m^* as experimentally measured in Ref. [128] for the Au(111) surface state, which is known to have a large Rashba splitting. It can be seen that our calculation reproduces the previously observed Rashba splitting of 0.26 nm^{-1} between the two parabola minima [128], as shown in Fig. 5.1. Therefore, the muffin-tin method can accurately describe the Rashba spin-orbit coupling in the absence of scatterers by including H_R in Eq. 5.1. When scatterers are present, this can potentially locally change the derivative of the potential in the z direction. However, this effect is expected to be negligible.

Next, we consider intrinsic spin-orbit coupling, which is a consequence of the coupling between the magnetic moment of the orbital angular momentum and the spin

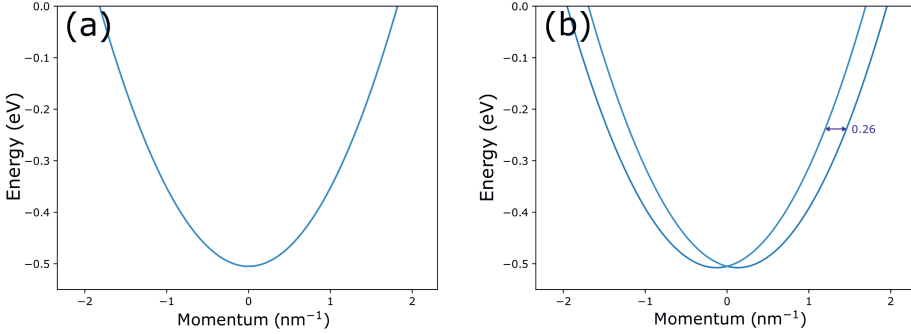


Figure 5.1: The gold surface state, calculated as a free electron gas (a) without and (b) with Rashba spin-orbit coupling. Here, an effective mass of $0.25 m_e$ and $\alpha_1 = 6.02 \times 10^4 \text{ m/s}$ were used, as measured in Ref. [128]

of the electron. In atomic systems, the intrinsic spin-orbit term H_I scales supralinear with the atomic number [129]. Thus, H_I tends to be much larger for heavier elements. In the case of the muffin-tin technique, however, the substrate is approximated as a 2D electron gas with an effective mass m^* and a scattering potential originating from the patterned adatoms. Thus, details on the precise potential landscape, like the size of the nuclei in the substrate, that give rise to the intrinsic spin-orbit coupling, are lost. Here, we propose a heuristic solution to this issue that maps the intrinsic spin-orbit coupling coming from Eq. (5.2) to the muffin-tin calculations by assuming an effective coupling α_2 between the patterned muffin-tin potential and the spin-orbit term,

$$H_I = \alpha_2 (\nabla V \times \mathbf{p}) \cdot \boldsymbol{\sigma}. \quad (5.4)$$

Note that \mathbf{p} represents the momentum operator acting on the envelope wave functions of the electrons in the 2D muffin-tin model. By allowing the effective parameter α_2 to be system dependent, Eq. 5.4 can be used for any type of artificial lattice. Additionally, because of the relative simplicity of this approach, it easily translates to both finite and periodic calculations, which is highly convenient when working with topological materials. Please note that α_1 and α_2 do not have the same units and $H_R \approx H_I$ does not mean that $\alpha_1 \approx \alpha_2$, as the potential derivative is only absorbed in α_1 , cf. Eq. (5.3) and (5.4).

As the electrons are confined to the x, y plane, only the z component of the cross product survives, and the intrinsic spin-orbit contribution becomes,

$$H_I = \alpha_2 \left(\frac{\partial V}{\partial x} p_y - \frac{\partial V}{\partial y} p_x \right) \sigma_z. \quad (5.5)$$

With appropriate fitting for the effective parameter α_2 , Eq. (5.5) should yield adequate predictions for spin-orbit coupling in an artificial lattice. Indeed, as shown in the next section, Eq. (5.5) reproduces the main features found using other methods. Adding H_R and H_I to Eq. (5.1), the full time-independent one-electron Schrödinger

equation becomes:

$$\left[\frac{-\hbar^2}{2m} \nabla^2 - i\hbar\alpha_2 \left(\frac{\partial V}{\partial x} \frac{\partial}{\partial y} - \frac{\partial V}{\partial y} \frac{\partial}{\partial x} \right) \sigma_z - i\hbar\alpha_1 \left(\frac{\partial}{\partial x} \sigma_y - \frac{\partial}{\partial y} \sigma_x \right) + V \right] \Psi_\sigma = E \Psi_\sigma. \quad (5.6)$$

For finite-size systems, solving this equation is not much different from solving the spinless system. Nevertheless, there is one important point to consider. Due to the presence of a derivative of the potential, the precise shape of the potential becomes important. For the muffin-tin potential, we would encounter infinities in the spin-orbit term. We solve this by using Gaussian potentials instead. As shown in the supplementary information, a change in potential shape from muffin-tin to Gaussian does not yield significantly different results in the case without spin-orbit coupling, and is therefore an appropriate approximation.

In the case of a periodic system, careful Fourier transformation is required to incorporate the spin-orbit couplings. We first Fourier transform the wave function:

$$\Psi_\sigma(\mathbf{x}) = \frac{1}{\sqrt{A}} \sum_{\mathbf{k}} e^{i\mathbf{k}\cdot\mathbf{x}} \Psi_\sigma(\mathbf{k}), \quad (5.7)$$

where $A = L^2$ is the system size in which the wave function is periodic, and $\mathbf{k} = \frac{2\pi}{L} (l_x, l_y)$, with l_i ranging from $-\infty$ to ∞ . Meanwhile, we also Fourier transform the potential V . However, as V has the unit cell periodicity we have

$$V(\mathbf{x}) = \sum_{\mathbf{K}} e^{i\mathbf{K}\cdot\mathbf{x}} V_{\mathbf{K}}, \quad (5.8)$$

where \mathbf{K} are the reciprocal lattice vectors. Applying these transformations to Eq. (5.6), the resulting equation also has to hold for a single Fourier component \mathbf{q} ,

$$\begin{aligned} \frac{\hbar^2}{2m} q^2 \Psi_\sigma(\mathbf{q}) - \hbar\alpha_1 (q_y \sigma_x - q_x \sigma_y) \Psi_\sigma(\mathbf{q}) \\ - i\hbar\alpha_2 \sum_{\mathbf{K}} V_{-\mathbf{K}} (K_x q_y - K_y q_x) \sigma_z \Psi_\sigma(\mathbf{q} + \mathbf{K}) \\ + \sum_{\mathbf{K}} V_{-\mathbf{K}} \Psi_\sigma(\mathbf{q} + \mathbf{K}) = E_q \Psi_\sigma(\mathbf{q}). \end{aligned} \quad (5.9)$$

Only wave functions of the shape $\Psi(\mathbf{q})$ and $\Psi(\mathbf{q} + \mathbf{K})$ appear in this equation. We can therefore apply a shift $\mathbf{q} \rightarrow \mathbf{q} + \mathbf{K}'$ and $\mathbf{K} \rightarrow \mathbf{K} - \mathbf{K}'$ to obtain a coupled system of equations for each \mathbf{q} in the Brillouin zone,

$$\begin{aligned} \frac{\hbar^2}{2m} (\mathbf{q} + \mathbf{K}')^2 \Psi_\sigma(\mathbf{q} + \mathbf{K}') \\ - \hbar\alpha_1 [(q_y + K'_y) \sigma_x - (q_x + K'_x) \sigma_y] \Psi_\sigma(\mathbf{q} + \mathbf{K}') \\ - i\hbar\alpha_2 \sum_{\mathbf{K}} V_{\mathbf{K}'-\mathbf{K}} [(K_x - K'_x) q_y - (K_y - K'_y) q_x + \\ K_x K'_y - K_y K'_x] \sigma_z \Psi_\sigma(\mathbf{q} + \mathbf{K}) \\ + \sum_{\mathbf{K}} V_{\mathbf{K}'-\mathbf{K}} \Psi_\sigma(\mathbf{q} + \mathbf{K}) = E_{\mathbf{q}+\mathbf{K}'} \Psi_\sigma(\mathbf{q} + \mathbf{K}'). \end{aligned} \quad (5.10)$$

In principle, Eq. 5.10 is an infinite set of equations, one for each \mathbf{K}' , and can therefore not be solved. However, we are only interested in the lowest bands. As $V_{\mathbf{K}}$ becomes exponentially small for large values of \mathbf{K}^2 for both Gaussian and muffin-tin potentials (see also the supplementary information), we can introduce a cutoff in the values of \mathbf{K}' that we consider. We can then solve the system of equations for arbitrary \mathbf{q} in the Brillouin zone. In this work, a square grid $iK_1 + jK_2$ with $K_{1,2}$ the reciprocal primitive vectors and i and j integers ranging from -4 to 4, was used.

5.3 Honeycomb structures

In order to see the effect of the spin-orbit terms introduced above on the band structure of artificial lattices, it is instructive to first investigate a test system. For this, we will consider a honeycomb lattice, as spin-orbit coupling has been extensively studied in graphene-like lattices through other methods [2, 5, 24]. As a starting point, the first artificial graphene lattice realized by Gomes et al. [15] using CO on the copper (111) surface might appear as a good choice. However, more elaborated designs of honeycomb lattices have recently been shown to lead to interesting features, like the appearance of a flat p band [28]. Additionally, for patterned quantum wells, intrinsic spin-orbit coupling is predicted to open a larger band gap between these higher bands than at the Dirac cone of the lower (i.e. predominantly s orbital) energy bands [124]. We therefore use the system described in Ref. [28] as a reference system. This system also uses CO molecules on copper (111), but instead of positioning single CO molecules in a triangular lattice as in Ref. [15], clusters of CO molecules are used. The clusters consist of two highly symmetrical rings. This added structure gives more confinement to the surface electrons without breaking the symmetry, which leads to a clear energetic separation of s and p orbitals and the appearance of not only s bands, as in Ref. [15], but also (nearly flat) p bands and a p orbital Dirac cone. The cluster arrangement of the CO molecules on the Cu (111) surface is shown in Fig. 5.2 (a). In Ref. [28], a muffin-tin potential with a height of 0.9 eV and a diameter of 0.6 nm is used. When switching to Gaussians, the choice was made for Gaussians with a full width at half maximum of 0.6 nm. With an adjustment of the potential height to 0.45 eV, this setup fully reproduces the muffin-tin results from Ref. [28], as shown in the supplementary information.

The bare band structure of the reference system is shown in Fig 5.2 (b). Here, we see the two lowest energy bands forming the well known Dirac cone at the K point, like in graphene. The p bands start with a (nearly) flat band, connected to two bands forming a p orbital Dirac cone at the K point, which is connected to a fourth p orbital band. Upon inclusion of the Rashba coupling, spin degeneracy is lifted everywhere except at the Γ point, as shown in Fig. 5.2 (c). This result is analogous to that of previous tight-binding studies on single-orbital honeycomb lattices [130, 131]. Additionally, the splitting of Dirac cones under the influence of Rashba spin-orbit coupling [130] is recovered, as shown in the supplementary information. The value of α_1 was set to a quarter of the value we found for Au(111). This allows for the effects of the Rashba term to still be clearly seen on the band-structure. Note that in principle the Au(111) surface state can also be used to construct artificial lattices. If only the intrinsic spin-orbit coupling is included, as shown in Fig. 5.2

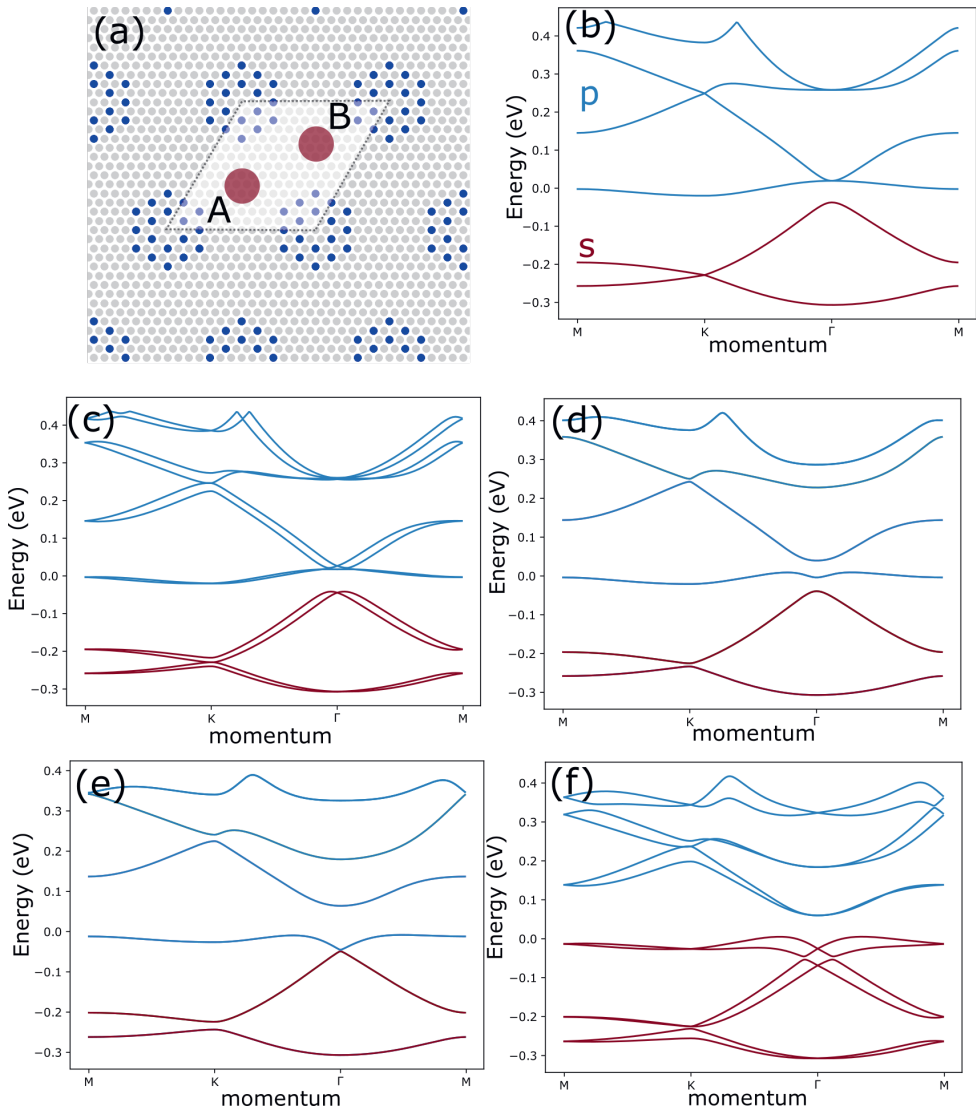


Figure 5.2: Periodic system calculations, using Cu (111) parameters as a test case (effective mass $m^* = 0.42 m$, CO molecules as Gaussians with a height of 0.45 eV and a FWHM of 0.6 nm). (a) shows the arrangement of CO molecules on Cu (111) in the reference system realised experimentally in Ref. [28] without spin-orbit coupling. The unit cell with the two lattice sites A and B is indicated. The band structure with s and p orbital bands plotted in red and blue respectively are shown (b) without any spin-orbit coupling; (c) with only Rashba spin-orbit coupling ($\alpha_1 = 1.6 \times 10^4 \text{ m/s}$); (d,e) with only intrinsic spin-orbit coupling ($\alpha_2 = 0.8 \times 10^{15} \text{ s/kg}$, $\alpha_2 = 2 \times 10^{15} \text{ s/kg}$) and (f) with both Rashba and intrinsic spin-orbit coupling ($\alpha_1 = 1.6 \times 10^4 \text{ m/s}$, $\alpha_2 = 2 \times 10^{15} \text{ s/kg}$).

(d,e), the spin degeneracy remains, and instead we see gaps opening up between the original band touching points. Indeed, this is also the result of intrinsic spin-orbit coupling in numerous other theoretical studies on honeycomb systems [24, 70, 100, 124, 125, 130, 131]. There is both theoretical and experimental evidence for these gaps to be topological and harbor protected edge states [24, 70, 71, 100, 124, 125]. Notably, the gap opening up between the first two p orbital bands at the Γ point is much larger than the gaps opening up at the K points. In previous works, a similar trend of larger gaps between the p orbital bands than between the s orbital ones is observed as a consequence of the same intrinsic spin-orbit coupling [70, 100, 124]. This effect can be explained by the angular momentum of p orbitals, making intrinsic spin-orbit coupling an onsite effect. In s orbitals that have no angular momentum, the spin-orbit coupling can only emerge through next-nearest-neighbour coupling, which connect the same sublattice in a honeycomb geometry. On the other hand, for p orbitals the intrinsic spin-orbit coupling can couple p_x and p_y orbitals on the same site, thus rendering the effect more robust [70]. Additionally, we see an unexpected effect, namely, if α_2 is large enough, the p orbital flat band is no longer isolated as in Fig. 5.2 (d), but the gap between the s and p type bands seemingly closes to form a Dirac cone at the Γ point, as shown in Fig. 5.2 (e). However, a small gap can be observed between the two bands. A zoom in on the gap can be found in the supplementary information. This phenomenon is interesting and it has not been observed before, as far as the authors are aware. Finally, we can also include both Rashba and intrinsic spin-orbit coupling, as shown in Fig. 5.2 (f). Here, we see that the Rashba coupling can close the gaps opened by the intrinsic spin-orbit coupling, diminishing the protection of possible topological states. However, the gap between the first two p orbitals is remarkably robust to the Rashba coupling. Additionally, the isolated flat band in Fig. 5.2(d) remains isolated in the presence of Rashba coupling, as shown in the supplementary information. This robustness against Rashba spin-orbit coupling is of high importance in applications of topological materials, as Rashba spin orbit coupling is to a certain degree always present in devices based on 2D materials.

In order to further study the topological nature of band gaps opened by the intrinsic spin-orbit coupling, we calculated the local density of states (LDOS) of the finite lattice. For this, we solved Eq. 5.6 on a finite grid with 8 points per nm, and included a square border of 2.56 nm with $V = 0$ surrounding the design. At the edge of the simulation box, periodic boundary conditions were imposed to mimic an infinite surrounding surface state. A Lorentzian broadening of 40 meV was included in the numerical solutions, to account for the experimental broadening resulting from the scattering of surface electrons to the bulk, as described in more detail in Ref. [18]. The solution for a finite honeycomb domain is essential, as it allows for characterisation of the in-gap state localized at the edge, see Fig. 5.3. The design used for the finite-size system is shown in Fig. 5.3 (a). We study two types of locations here, onsite locations indicated by the pink dot, and bridge locations, indicated by the green dot for the bulk and blue dot for the edge. Along the top edge, onsite edge locations have been marked with purple crosses, and edge and sub-edge bridge sites have been marked with yellow and open circles, respectively. This design is different from the periodic case only at the boundary, where blocker potentials have been placed to separate the lattice from the surrounding 2D electron gas. The introduc-

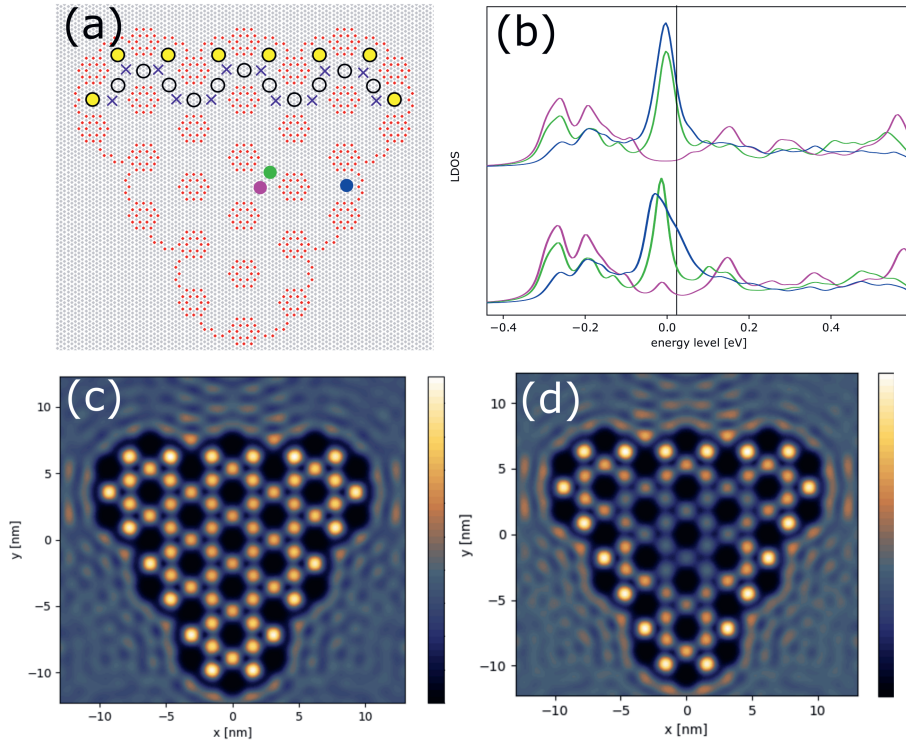


Figure 5.3: Finite-size system calculations using Cu (111) parameters as a test case as in Fig. 5.2. Here, a spectral broadening of 40 meV realistic for the CO on Cu (111) system has also been included. (a) The locations of CO sites (red) on the Cu (111) grid (gray). Along the top edge, the locations of lattice sites, edge bridge sites and sub edge bridge sites have been indicated with purple crosses, yellow disks and open disks respectively. (b) The spectra calculated for the spots indicated in (a). The top and bottom curves correspond to the system without and with intrinsic spin-orbit coupling ($\alpha_2 = 2 \times 10^{15}$ s/kg), respectively. (c), (d) A map of the calculated LDOS on the energy indicated by a vertical line in (b) at $E = 0.027$ eV without and with intrinsic spin-orbit coupling, respectively.

tion of these blockers is crucial as without them there would be no clear boundary and therefore it would not be possible to study edge states. The location of blocking potentials is non trivial, as the introduction of out of lattice potentials can change the onsite energy of nearby sites. They have, therefore, been chosen in such a way as to not shift the LDOS spectra at the edge sites with respect to the bulk, as can be seen by comparing the blue and green lines in the top graph of Fig. 5.3 (b). A triangular design was chosen to optimise the distance between the boundaries and at the same time have edges as uniform as possible, given the small system size. The system was studied without and with intrinsic spin-orbit coupling. The LDOS spectra of the two systems are mostly similar in the bulk, as shown in Fig. 5.3 (b). The pink and green spectra representing the bulk both with and without spin-orbit coupling display two peaks from the s orbitals at ≈ -0.3 and ≈ -0.2 eV, and both show a peak corresponding to the flat p band around 0 eV. These peak locations are inline with the band structure in Fig. 5.2 (b) and (e). However, some differences are visible. In the case without spin-orbit coupling (Fig. 5.3 (b) top), there is very little mixing between the s and p orbitals resulting in an on-site (pink) dip at the flat band energy due to negative interference between the p orbitals in the flat band. In the intrinsic spin-orbit case, there is more mixing, as evidenced by the band touching between the highest s and lowest p orbital in Fig. 5.2 (e). Therefore, there is some onsite density of state in this case, as evidenced by a pink peak around 0 eV (Fig. 5.3 (b) bottom). At a slightly higher energy (0-0.06 eV) we see a dip in the bulk spectra of the intrinsic spin-orbit case. This corresponds to the band gap between the first two p orbitals in Fig. 5.2 (e) from 0 till 0.05 eV. Notably, the edge bridge site where the spectrum was calculated (blue) has an increased LDOS in this range (the shoulder is a signature of an additional peak, which cannot be separated from the flat band one), signaling a possible edge state. Indeed, if we look at LDOS maps at 0.027 eV, we see a state clearly localized on the (sub) edge bridge sites of the system indicated in Fig. 5.3 (a) for the intrinsic spin-orbit system, as shown in Fig. 5.3 (d), whereas none is present for the system shown in Fig. 5.3 (c), without spin-orbit coupling. Thus, as expected, intrinsic spin-orbit coupling results in a strong decrease in the DOS over the entire bulk of the finite system in the gap between the third and fourth band, accompanied with an increase in the intensity at the bridge sites at the system edge, pointing to a protected edge state. The intensity is maximal on the bridge sites, in accordance with the p orbital bands. We cannot test the precise topological nature of the edge state within the present muffin tin model; but an atomistic tight-binding study on a semiconductor system showed that this state is a helical quantum spin Hall state [24].

5.4 Conclusion

We have presented an effective muffin-tin model by introducing the intrinsic and Rashba spin-orbit coupling into the Schrödinger equation and tested the adequacy of the model by comparison with established results. Then, we have studied the effect of spin-orbit coupling on a honeycomb system with separated s and p orbital bands, which allows us to study p orbital physics in the honeycomb system. Besides the expected band openings at the Dirac points, intrinsic spin-orbit coupling shifts

the p orbital flat band downwards, causing hybridization with the s bands. As a result, a broad gap arises between the third and fourth band of the system; our results on a finite lattice show the emergence of an edge state in this gap. We see that Rashba spin-orbit coupling reduces the spin-orbit gaps at the K and K' points of the Brillouin zone, but the broad gap between the third and fourth band remains robust. We should also remark that the model that we developed can be used to study the effects of spin-orbit coupling on any type of artificial lattice, including honeycomb patterns in semiconductor quantum wells.

Experimentally, strong spin-orbit coupling might be realized in artificial lattices by using a metallic surface state on a heavy element metal such as rhenium, lead or bismuth, and/or using heavy adatoms as potential barriers or attractive sites for the surface electrons. A similar concept has been reported for graphene, by placing In and Tl atoms in the hollow sites of a graphene monolayer [5]. Real devices, applicable in electronics, can be achieved by nanoscale patterning of heavy-element semiconductor quantum wells, such as Ge, GaAs and InSb, with a honeycomb or another geometry of interest [12, 14, 114].

Supplementary Information

Gaussian potentials

Recent works have been modeling the experimental results of artificial lattices built using CO on copper (111) by using a Muffin-tin calculation. Here, the Schrödinger equation is solved in two dimensions for a potential landscape where the CO molecules are modeled as positive disk shaped protrusions. This approach is convenient in Fourier space, as the Fourier transformed form of this potential is analytically known.

However, the intrinsic spin-orbit coupling term contains a derivative with respect to the potential, making the muffin-tin approach less ideal. We therefore turn to modeling the CO molecules as Gaussian potential barriers. We find that this reproduces the muffin-tin results. Furthermore, there appears to be a lot of freedom in choosing the width of the Gaussians, as long as the height is adjusted as well (the broader the Gaussian, the lower it should be). The classical muffin-tin results, along with the results for a Gaussian potential landscape, are shown in Fig. S5.1. The relation between the width of the Gaussian and its height in order to reproduce the classical muffin-tin results is shown in Fig. S5.2.

In case of a periodic system, we run into another important point, which is that the Gaussian potentials are not zero at the unit cell boundaries, but have a non-zero tail. However, we can approximate the Fourier transform of the Gaussian in the unit cell as an infinite Fourier transform. The error is minimal, as the Gaussian potential exponentially decreases away from the centre and is thus very small outside of the unit cell. We have

$$V_{\mathbf{K}} = \frac{1}{A} \int_{\text{unitcell}} e^{-a|\mathbf{x}|^2} e^{-i\mathbf{K}\cdot\mathbf{x}} d\mathbf{x} \approx \frac{1}{A} \int_{-\infty}^{\infty} e^{-a|\mathbf{x}|^2} e^{-i\mathbf{K}\cdot\mathbf{x}} d\mathbf{x}, \quad (5.11)$$

where A is the unit cell surface. The integral on the right is a known integral, and thus we get

$$V_{\mathbf{K}} \approx \frac{\pi}{a} e^{-|\mathbf{K}|^2/4a}. \quad (5.12)$$

Indeed, the potential becomes exponentially small for large \mathbf{K} , thus making it possible to introduce a cutoff on the \mathbf{K} values included in Eq. 5.10 to calculate the band structure.

In classical muffin-tin calculations, the potential is fully periodic and the Fourier transformed potential is analytically known,

$$V_{\mathbf{K}} = \frac{\pi d}{A|\mathbf{K}|} J_1\left(|\mathbf{K}|\frac{d}{2}\right) V_0. \quad (5.13)$$

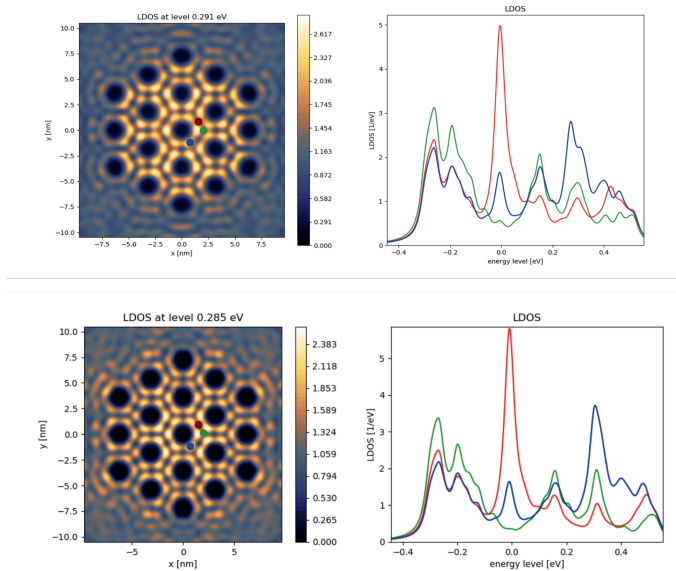


Figure S5.1: Finite-size system comparison. Top images are made using Gaussians with a full width at half maximum (FWHM) of 0.6 nm and a height of 0.45eV and the bottom images were created using a classical muffin-tin calculation with a diameter of 0.6 nm and a height of 0.9eV.

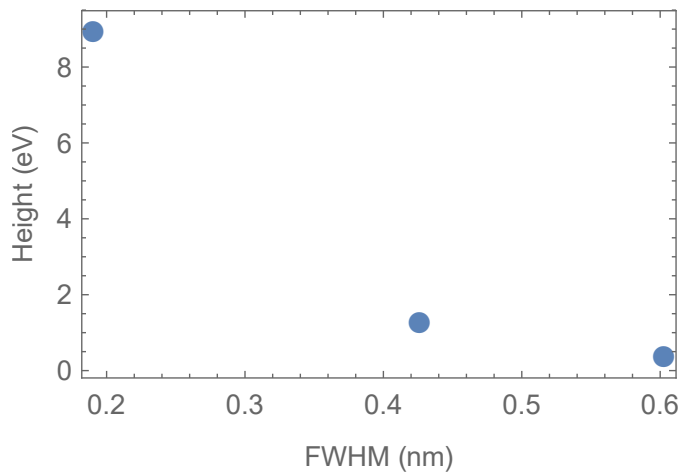


Figure S5.2: Relation between the height of the Gaussians and their full width at half maximum (FWHM) that reproduce the muffin-tin results.

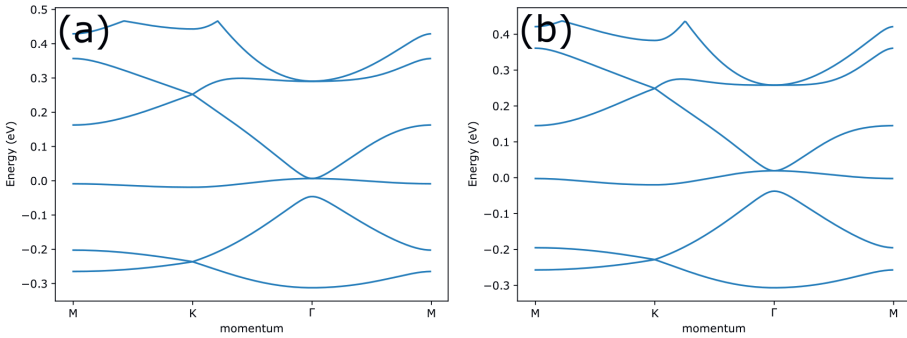


Figure S5.3: Band structure of double ring design calculated using (a) Muffin-tin and (b) Gaussian shaped potentials. The position of CO molecules on a copper lattice is shown in Fig. 5.2 (a).

Here, d is the diameter of the muffin-tin potential disks, V_0 is the height of the potentials, and J_1 is the Bessel function. Just as for the Gaussian potential, $V_{\mathbf{K}}$ becomes small for large \mathbf{K} .

When the spin-orbit coupling is tuned to zero, the muffin-tin and Gaussian potential can be compared. Using the same parameters as before, we indeed see the same band structures for both potentials. This is shown in Fig. S5.3.

Rashba modified Dirac point

As mentioned in the main text, the Rashba coupling creates additional Dirac cones around the s orbital Dirac cone in the muffin-tin method, as shown in Fig. S5.4. This is in agreement with tight-binding calculations for Rashba coupling in graphene [130].

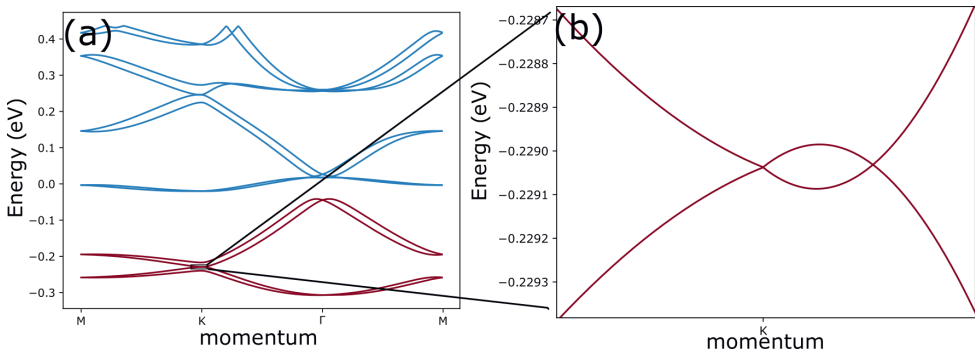


Figure S5.4: A zoom in on the s orbital Dirac cone in Fig. 5.2 (c). The location of the zoom is indicated in (a). (b) shows the zoomed in image.

"Dirac" point between s and p bands

In Fig. 5.2 (e) the s and p bands seem to hybridize to form a Dirac cone. However upon close inspection we see that the gap between the bands does not close, as shown in Fig. S5.5.

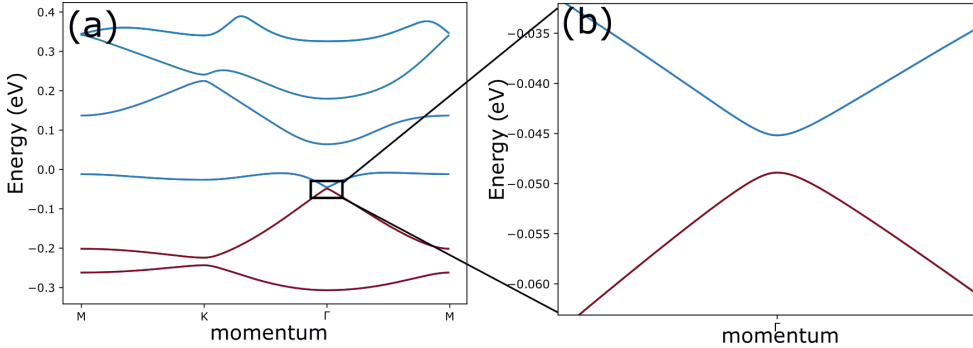


Figure S5.5: A zoom in on the apparent Dirac cone between the s and p bands in Fig. 5.2 (e) of the main text. The location of the zoom is indicated in (a). (b) shows the zoomed in image.

Rashba coupling and an isolated flat band

In Fig. 5.2(d), it was shown that an isolated flat band can be obtained with the right α_2 . The isolation of the band is robust against Rashba coupling, as shown in Fig. S5.6.

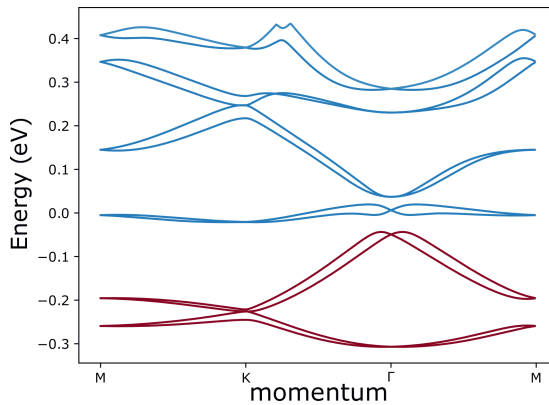


Figure S5.6: Rashba coupling with intermediate intrinsic spin-orbit coupling. The band structure was obtained with $\alpha_1 = 1.6 \times 10^4 m/s$ and $\alpha_2 = 0.8 \times 10^{15} s/kg$; the remaining parameters were the same as in Fig. 5.2(d).

On the influence of electron spin in artificial lattices

This chapter is partially based on the following publication:

J. J. van den Broeke*, T. S. Gardenier*, R. A. M. Ligthart & I. Swart, *On the influence of electron spin in artificial lattices*, in preparation.

*Both authors contributed equally

Recently, artificial lattices consisting of coupled quantum corrals have been used to study and engineer the electronic structure of a wide variety of geometries. Thus far, the spin degree of freedom of electrons in this kind of artificial lattices has not been considered. Here, we investigate the interplay between magnetic field, orbital angular momenta, and spin in quantum corrals, and calculate the spin interaction with a magnetic field in a CO/Cu(111) system that could be measured with a non spin-polarized STM tip.

6.1 Introduction

Atom manipulation in a scanning tunneling microscope (STM) can be used to create systems that do not exist in nature, such as mirages [132], logical circuits [133] and 2D analogues of real crystals [15, 18]. These analogues have recently been shown to reproduce a wide array of crystal features, such as topology [27, 88], higher orbital physics [28, 29] and fractal structure [20]. However, the influence of spin in these artificial systems has not yet been investigated. This is unfortunate, as the spin of electrons is the basis for many fascinating phenomena, such as the quantum spin Hall effect [2] and the quantum anomalous Hall effect. Thus, it is important to gain a good understanding of the influence of spin in artificial lattices. For this, it is convenient to start by investigating the spin in the building blocks of artificial lattices, quantum corrals.

Quantum corrals were one of the first structures built using STM atom manipulation and showed standing wave patterns, corresponding to the electronic states, due to the confinement of the surface state electrons within a ring of adatoms [52]. Since then, many groups have created quantum corrals on different combinations of substrates and adatoms [134, 135] and used them to investigate other properties such as electron diffusion [136] and scattering [134]. Quantum corrals can also be interpreted as the building blocks for larger artificial lattices [53]. Thus, the introduction of spin and magnetic field in quantum corrals would open up a new array of possibilities for artificial lattices.

To assess the feasibility to include spin physics in artificial lattices of coupled quantum corrals, we propose experiments on small quantum corrals subjected to magnetic fields of up to 5 T. We establish the relative importance of orbital and spin contributions by studying the influence of the magnetic field on s type (with orbital moment of zero) and p type orbitals (with orbital moment one). The changes in local density of states (LDOS) due to the magnetic field show that the orbital mo-

momentum coupling with the magnetic field has effects on the same order as the spin magnetic coupling. To investigate this effect in more detail, we have also included a square quantum corral, for which the angular momentum is not well defined. The adsorbates that define the quantum corral generate a potential energy landscape with finite barriers of finite width. In previous experiments, the confining wall of scatterers was 1 atom or molecule thick. To reduce the coupling between the quantum corral and the surrounding 2DEG as far as possible, we employ a barrier of three concentric rings of repulsive scatterers, see Fig. 6.1(a), (b) for the circular and square quantum corral, respectively. The red circles show the position of the CO molecules with a barrier height of 0.9 eV on the Cu(111) surface (gray).

6.2 Magnetic muffin-tin model

In order to predict the experimental results, a muffin-tin approximation is used, as described in chapter 2. The surface state is described as a two dimensional electron gas. The CO molecules are described as potential discs with a diameter of 0.6 nm and a height of 0.9 eV. Hence, they define the potential landscape for the surface state electrons. A larger system is created by placing these discs at the positions of the CO molecules and subsequently numerically solving the Schrödinger equation. This method has yielded excellent agreement with measurements in earlier works without magnetic fields [18, 20, 28, 29, 88].

Here, we extend this model to also include magnetic field effects. Without a magnetic field, the system is described by the following Hamiltonian,

$$H = \frac{\mathbf{p}^2}{2m^*} + V(x, y), \quad (6.1)$$

with $\mathbf{p} = (p_x, p_y)$ denoting the momentum, m^* the effective mass of the electrons at the Cu(111) surface, and $V(x, y)$ the muffin-tin potential. We can add a magnetic field to this formula by transforming $\mathbf{p} \rightarrow \mathbf{p} - q\mathbf{A}$ with \mathbf{A} the magnetic vector potential and q the electron charge. However, as the electrons also have spin, we must add the coupling between the spin magnetic moment and the magnetic field, the spin Zeeman term, as well. Thus, we obtain the muffin-tin version of the Pauli equation [76],

$$H = \frac{(\mathbf{p} - q\mathbf{A})^2}{2m^*} - \frac{q}{m^*} \mathbf{S} \cdot \mathbf{B} + V(x, y), \quad (6.2)$$

with \mathbf{S} the electron spin operator. As the electrons are moving in a two dimensional (x, y) plane and the magnetic field is perpendicular to this plane, we can rewrite this to get,

$$H = \frac{\mathbf{p}^2}{2m^*} - \frac{q}{2m^*} (\mathbf{L} + 2\mathbf{S}) \cdot \mathbf{B} + \frac{q^2 \mathbf{B}^2}{8m^*} r^2 + V(x, y), \quad (6.3)$$

where \mathbf{L} is the angular momentum, \mathbf{r} is the position vector and the symmetric gauge $\mathbf{A} = \frac{1}{2} \mathbf{B} \times \mathbf{r}$ has been used.

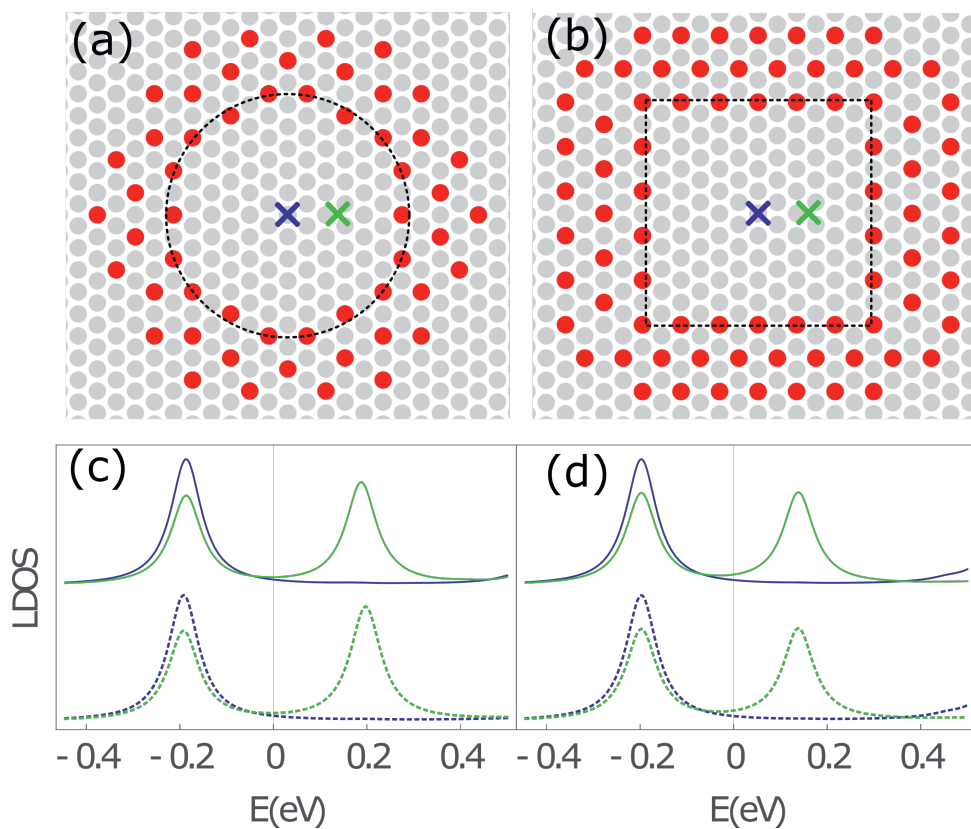


Figure 6.1: (a) Placement of CO molecules (red circles) to form a quantum corral with a diameter of 3.07 nm on a Cu(111) background (gray circles). The crosses indicate the positions of the spectra taken at the centre of the corral and 0.5 nm off-centre in purple and green, respectively. The black dotted line indicates the boundary of the corresponding quantum well (b) same as (a) but for a square quantum corral. (c), (d) local density of states for the circular and square quantum corral (solid lines), and quantum well (dotted lines), respectively. The color of the graph corresponds to the locations indicated in (a), (b).

6.3 Quantum well

A standard circular quantum corral confines electrons into a circular area which approximates the standard particle-in-a-box model with the box being a 2D circular infinite potential well. Solving the Schrödinger equation for such an infinite well in polar coordinates r, θ , gives eigenenergies and wave functions corresponding to [54]

$$\phi_{n,l}(r, \theta) \propto J_{|l|}\left(\frac{j_{|l|,n}r}{a}\right) e^{il\theta}, \quad E_{n,l} = \frac{\hbar^2 j_{|l|,n}^2}{2m^* a^2}, \quad (6.4)$$

respectively, where $n = 0, 1, 2, \dots$, $l = 0, \pm 1, \pm 2, \dots$, $j_{|l|,n}$ is the n -th crossing of zero of the $|l|$ -th Bessel function, a is the radius of the well, and the angular momentum L is given by $L = \hbar l$. The local density of states of different positions in a circular corral is plotted in the bottom row of Fig. 6.1(c). Here, a Lorentzian broadening of 40meV has been included for better comparison to the CO on copper system. In this work, we will be focusing on the three lowest energy solutions ($\phi_{1,0}$ and $\phi_{1,\pm 1}$). $\phi_{1,0}$, also sometimes referred to as the 1s solution for its similarity to the atomic solution, has a high density of states in the center and gradually becomes lower towards the edge. This corresponds to the lowest energy peak at -190 mV in the local density of states plot. At slightly higher energy, approximately 180 mV, the peak corresponding to the degenerate $\phi_{1,\pm 1}$ (1p) solutions is visible. These solutions have no density of states in the center of the corral. A quantum corral is similar to the circular quantum well, but has less confinement by CO molecules than infinite potential barriers. Additionally, the experimental quantum corral does not have full circular symmetry. In the quantum corral design shown in Fig. 6.1(a), these differences have been minimized: the circular symmetry has been maintained as much as possible on the hexagonal copper grid, and a triple layer of CO molecules has been used to maximize the quantum confinement. The resulting energy spectrum calculated using the classical muffin-tin model is in excellent agreement with the quantum well solutions, as shown in Fig. 6.1(c).

For the square quantum well with infinite barriers at $x, y = 0, x, y = L$, the solutions are given by,

$$\phi_{n,k}(x, y) \propto \sin\left(\frac{\pi n}{L}x\right) \sin\left(\frac{\pi k}{L}y\right), \quad E_{n,k} = \frac{\hbar^2 \pi^2 (n^2 + k^2)}{2m^* L^2}. \quad (6.5)$$

Just like the circular well, the square well has an s ($n = 1, k = 1$) and degenerate p type ($n = 2, k = 1$ and $n = 1, k = 2$) solutions, and can be approximated using a square quantum corral, as shown in Fig. 6.1(b,d). Note that in contrast to circular corrals and real atoms, angular momentum is not well defined for square corrals and wells. It is therefore unclear what the consequence of the $L \cdot B$ term in Eq. 6.3 is. This raises the question to what extend square (and rectangular) quantum corrals can be thought of as artificial atoms.

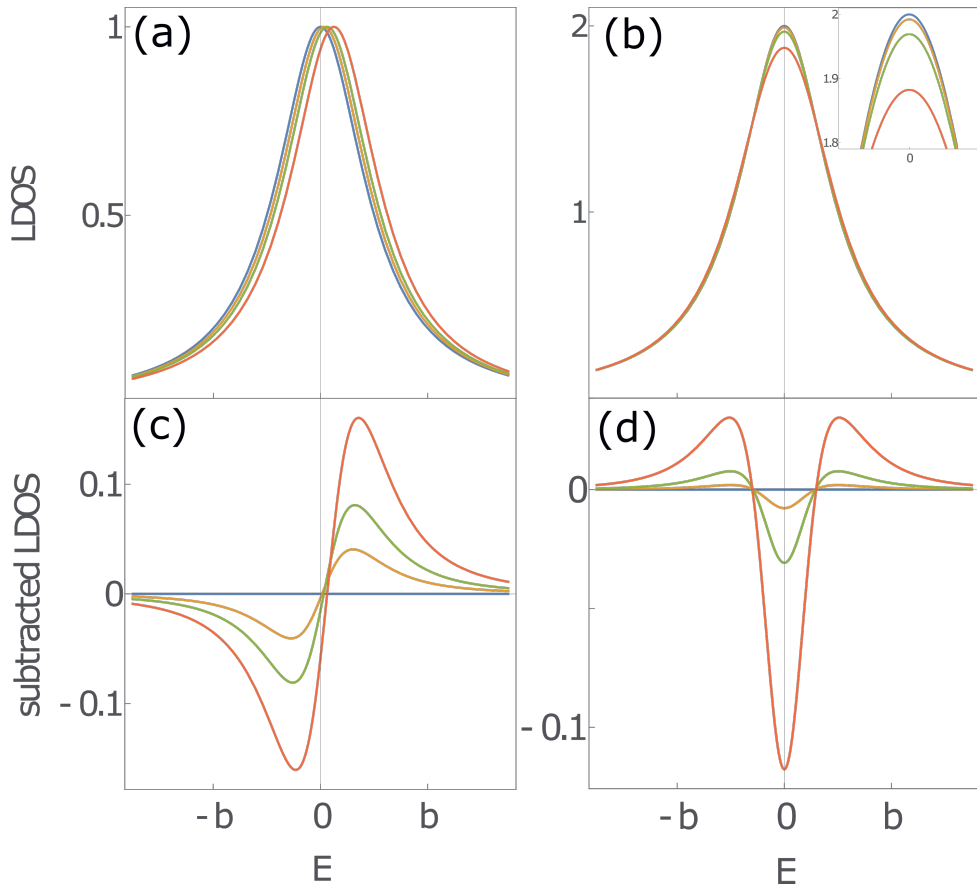


Figure 6.2: Difference spectra for shifted and split Lorentzian peaks $L_i(E)$, centered at $E=i$ with broadening b . (a) Shifted Lorentzians $L_i(E)$ with $i=0, \frac{1}{32}b, \frac{1}{16}b, \frac{1}{8}b$ in blue, yellow, green and red, respectively. (b) Split Lorentzian peaks $L_i(E) + L_{-i}(E)$ with $i=0, \frac{1}{32}b, \frac{1}{16}b, \frac{1}{8}b$ in blue, yellow, green, and red, respectively. Inset shows a zoom of the top of the graph. (c) Subtracted shifted Lorentzians, $L_i - L_0$, with i and colors as in (a). (d) Subtracted split Lorentzian peaks, $L_i(E) + L_{-i}(E) - 2L_0$ with i and colors as in (b).

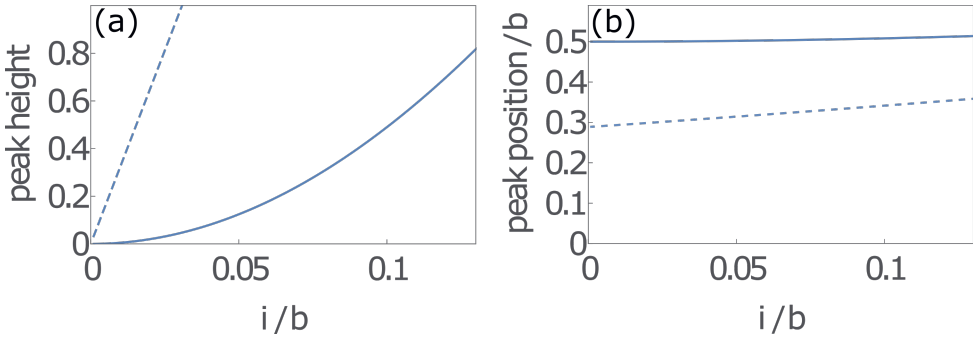


Figure 6.3: (a) Difference spectra peak heights and (b) peak positions for shifted ($L_i - L_0$ (dotted)) and split ($L_i(E) + L_{-i}(E) - 2L_0$ (solid)) Lorentzian peaks $L_i(E)$.

6.4 Subtracted spectra

Using the Hamiltonian from Eq. 6.3, we can predict how a magnetic field perpendicular to the surface will influence the quantum corral solutions. To enhance the visibility of the magnetic field effects, we plot subtracted spectra. As the broadening in the LDOS spectra is Lorentzian [18], a shift or splitting of the s and or p orbital energy peaks of the quantum corrals corresponds to a shift of Lorentzians. It is therefore instructive to first investigate how small changes in Lorentzian functions,

$$L_i(E) = \frac{b^2/4}{(E - E_i) + b^2/4} \quad (6.6)$$

with E_i the center of the Lorentzian and b the broadening, look like in subtracted spectra.

If a Lorentzian peak in the LDOS is shifted by small amounts compared to the broadening b , as in Fig. 6.2(a), the resulting subtracted spectra display a single dip, followed by a peak, as in Fig. 6.2(c). It is important to note here that the top of the peak becomes approximately linearly higher with a bigger shift, see Fig. 6.3(a), but this is less clear for the position of the top, as the position does not converge to zero as the shift i becomes zero (Fig. 6.3(b)). For a split in a Lorentzian peak as in Fig. 6.2(b), as one might expect from the Zeeman effect, a slightly different pattern emerges. In this case, we see a symmetric pattern of a peak followed by a dip and another peak, as in Fig. 6.2(d). Here again we see a clear effect of the size of the split on the height of the peaks in Fig. 6.3(a), but not on the peak positions in Fig. 6.3(b), as would be the case for splits large compared to b .

The difference spectra for the quantum corrals for the same center and off-center positions as in Fig. 6.1 are shown in Fig. 6.4. To assess the importance of the orbital and spin components on the observed signal, we show theoretical spectra where the coupling between the spin moment and the magnetic field is excluded (red lines), as well as calculations where both the orbital and spin degree of freedom are taken into account (green and purple lines). Due to the absence of orbital angular momentum for the 1s-like state, the two simulations give markedly different signatures.

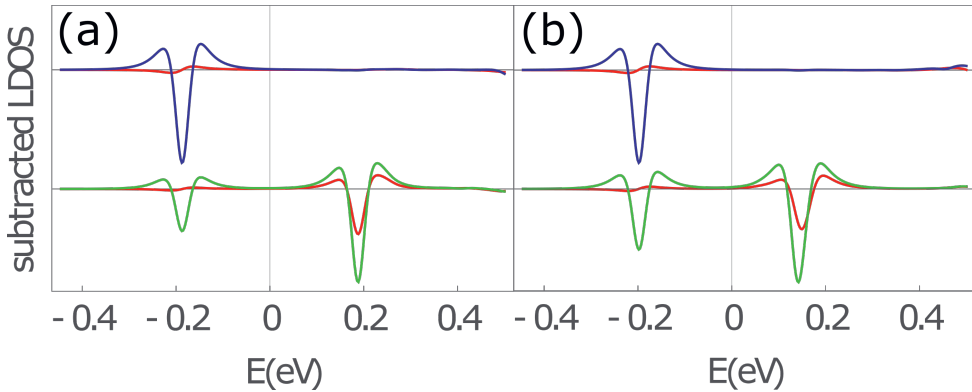


Figure 6.4: Subtracted spectra (5T-0T) taken at the center (purple) and off-center (green) of the corral. Red lines indicate the spin term is excluded from the Hamiltonian. (a) and (b) show the spectra for the circular and square quantum corral, respectively.

The top of Fig. 6.4(a) shows subtracted spectra calculated at the center of the circular quantum corral (purple). The 0 T spectrum is subtracted from the 5, spectrum which gives difference spectra with various shapes. At the energy of the $1s$ peak (-190 mV) we find a small indication of a shift (red) and a clear sign of splitting of peaks (purple). The shift is most likely caused by the B^2 term in Eq. 6.3. The splitting of the peaks is a consequence of introducing the coupling between the spin and magnetic field to the Hamiltonian. This term causes the spin up and spin down electrons to shift to lower and higher energies, respectively. At 0.5 nm away from the center of the corral, a feature due to the p type orbitals appears at $V = +180$ mV (Fig. Fig. 6.4(a), bottom spectra). For this energy, the orbitals with angular momentum ($l \neq 0$) already have a splitting even in the absence of Zeeman coupling, due to the magnetic field coupling with the angular momentum. Realize that the s type orbitals have no angular momentum and therefore do not split into two peaks in the spin-less case. If the spin term is turned on, all orbitals gain an additional splitting irrespective of the angular momentum.

Remarkably, an almost identical picture appears when we study the subtracted spectra for the square quantum corral, as shown in Fig. 6.4(b). This is interesting, as we understood the splitting of peaks in the absence of spin as the coupling between the angular momentum of the quantum corral and the magnetic field. However, due to the breaking of angular symmetry in the square system, the angular momentum is not well defined. One could argue that this is due to the square quantum corral being an imperfect sphere. However, even for the square quantum well, the spin less splitting of the p orbitals is present, as shown in the supplementary material. It is presently not fully understood how to interpret the observed orbital coupling for square/rectangular corrals.

6.5 Conclusion

We have shown that it is possible to distinguish between orbital and spin effects of the magnetic field in a quantum corral by focusing on a certain orbital ($l = 0$ or $l \neq 0$). STM experiments should be able to visualize a splitting of peaks corresponding to the coupling between the spin of the confined electrons and an external magnetic field, even with a non spin-polarized tip. Spectra at the center of a corral can prove immediately if a spin effect is visible in the quantum corral or not.

In addition, we have found that even if the angular momentum of an artificial atom is not well defined mathematically, a splitting between p orbital artificial atom peaks does occur in a spin less system in the presence of a magnetic field, indicating that artificial atoms effectively have an angular momentum, independent of their precise symmetry. This idea is supported by the work on spin-orbital coupling in artificial honeycomb lattices in chapter 5, where the circular symmetry of the artificial atoms was broken as well. The presence of angular momentum in non-symmetric artificial atoms allows for an even stronger analogy with atomic systems and opens the door to more angular momentum related effects.

Supplementary Information

Bessel functions

An infinite quantum well confines electrons into an ideal situation where all states are quantised. In an infinite well, the wave functions have a strict boundary condition, namely that they must be zero at the edges of the well. An ideal quantum corral has the same condition, and the wave function shape can be described by Bessel functions [52, 137]. A 0-th order Bessel function has a non-zero value at $x = 0$ which is the centre of the corral. This corresponds to s type orbitals having no nodes at the centre of a corral. Higher order Bessel functions all have a node at 0 corresponding to orbitals with higher angular momentum quantum numbers ($l \neq 0$). An STM can only measure the electron probability, corresponding to the squared wave function $|\Psi|^2$. A schematic depiction of the four lowest lying wave functions is shown in Figure S6.1. These wave functions correspond to the four lowest lying states (not counting degeneracy) in a small quantum corral, the $1s$, $1p$, $1d$ and $2s$ states.

Subtracted spectra of quantum well systems

Besides the subtracted spectra for the quantum corral, as in Fig. 6.4, one can also calculate the influence of the magnetic field on quantum well systems as in Fig. 6.1. The resulting subtracted spectra are shown in Fig. S6.2.

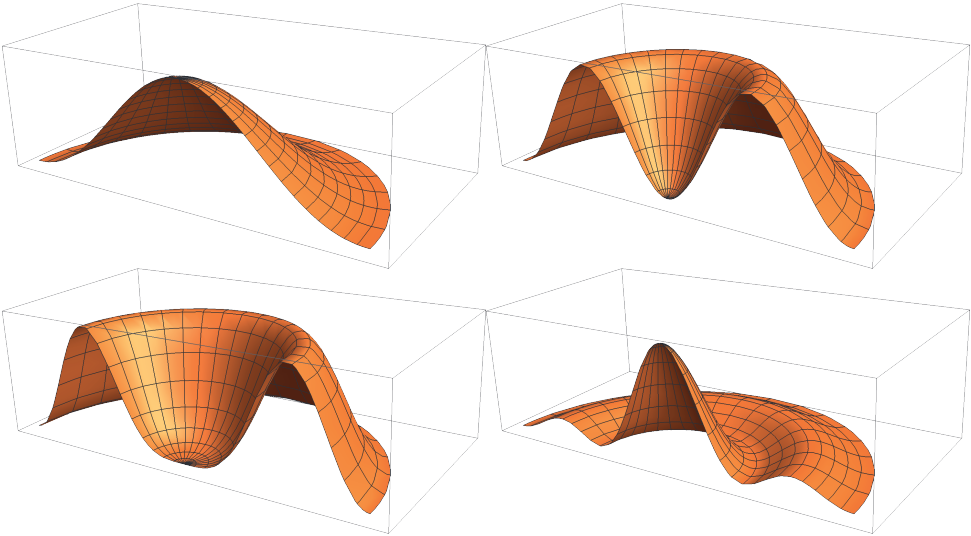


Figure S6.1: Schematic representation of the squared wave function cross section corresponding to the four lowest lying orbitals. FLTR: 1s, 1p, 1d and 2s orbital.

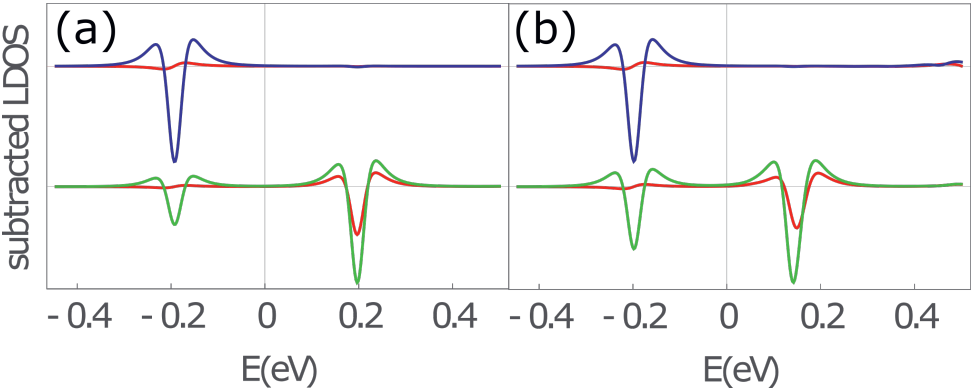


Figure S6.2: Subtracted spectra (5T-0T) taken at the center (off-center) of the well in the top (bottom) half of the graph, red lines indicate the spin term is excluded from the Hamiltonian. (a), (b) show the spectra for the circular and square quantum well respectively.

Conclusion

In this thesis, we have explored several possibilities for artificial electron lattices. We have shown that artificial electron lattices can be adequate quantum simulators that mimic important features of atomic lattices such as orbital degree of freedom, topology, spin-orbit coupling and the Zeeman effect. In these artificial electronic lattices created with an STM, essential lattice parameters such as bonding strengths and energy scale are much more easily adaptable than their atomic equivalents.

In **Chapter 3**, we found through the Kekulé lattice that it is possible to introduce crystalline topology into artificial electron systems, and detected the corresponding edge states. Contrary to quantum Hall or quantum spin Hall edge states, these crystalline topological edge modes do not require magnetic fields or strong spin-orbit coupling, making them much easier to realize. However, the nature of these edge modes is also different. The topological Kekulé edge modes only occur for specific boundary conditions, requiring very precise boundary construction. Additionally, although the even and odd edge modes in the Kekule lattice are prevented from splitting at the high-symmetry points of the Brillouin zone by the symmetry of the lattice, like the time-reversal symmetry related edge modes in the quantum spin Hall effect, the equivalence seems to end there. The even and odd modes in the Kekule lattice have no clear backscattering protection and are not well defined outside of the high-symmetry point, like the spin polarized edge modes, that transform into each other under a time-reversal operation in quantum spin Hall systems. Whether these type of edge modes can be used for practical applications, remains an open question.

For the artificial electronic honeycomb lattice, we found in **Chapter 4** that it is possible to bring p character bands in the accessible energy window of the CO on Cu(111) system by changing the size of the unit cell. Additionally, we found that the p orbital band could be isolated in energy from the s orbital bands by increasing

the quantum confinement through clustering of CO molecules into double layered rosettes. For the resulting four isolated p orbital bands, we predicted through muffin-tin and tight-binding calculations two flat bands connected through a p -orbital Dirac cone. Experimentally, the predicted signatures of the first flat band and the Dirac cone were measured. However, the second flat band was more difficult to observe due to the closeness to the edge of the observable energy window and mixing with higher energy bands. This could possibly be resolved by using larger CO clusters providing more orbital separation and/or enlarging the lattice unit cell. However, enlarging the unit cell further would only have limited effect in the CO on Cu(111) system, as the bands can not get too close together due to the broadening effect. The observation of flat bands is interesting, as their kinetic energy is quenched, making interaction effects such as superconductivity the dominant contribution. However, the flat band observed here is not isolated, allowing for kinetic contributions from the connecting band.

One way to isolate the p orbital flat band in a honeycomb lattice in a tight-binding model is through intrinsic spin-orbit coupling. In this case, the band is not only isolated, but can also become topological [24]. Using muffin-tin simulations, we predicted in **Chapter 5** that this is also the case for artificial electron p orbital flat bands. We find that under the influence of spin-orbit coupling, the flat band becomes isolated and the resulting gap hosts edge states, signaling a topological character. Due to their non local character, topological isolated flat bands are especially interesting, and have been predicted to be responsible for the superconducting behavior of twisted bilayer graphene [25, 26]. Additionally, we found that the gap in the p orbital bands is relatively large compared to the gap that opens up between the s orbital bands. This effect, caused by the onsite character of intrinsic spin-orbit coupling induced p orbital hopping, leads to more robustness of spin-orbit band gaps against Rashba coupling. It is therefore highly relevant for the realization of the quantum spin Hall effect, which can be destroyed by Rashba spin-orbit coupling [2]. Unfortunately, the spin-orbit coupling in copper is too small to observe a topological flat band or the quantum spin Hall effect. There are several possibilities to increase the intrinsic spin orbit coupling, like the addition of heavy atoms to the lattice, or building the lattice on heavier substrates. However, these techniques are still in development.

Finally, in **Chapter 6** we investigated the effect of perpendicular magnetic fields in artificial electronic lattices. As the effects of the currently available magnetic fields in STM systems are very small, we investigate subtracted spectra. We find that for individual artificial atoms, or quantum corrals, the energy splitting due to coupling of the magnetic field to the spin has approximately the same order of magnitude as the energy splitting caused by the coupling between the magnetic field and angular momentum of the electrons. However, as s orbitals have no angular momentum and p orbitals do, we can compare the energy splitting in these orbitals to separate the spin and angular momentum effects. Interestingly, we find that in both square and round quantum corrals there is a significant coupling between the (effective)

angular momentum and a perpendicular magnetic field. This is remarkable, as the angular momentum of square quantum wells is not well defined, and provides additional proof that artificial electronic atoms have orbitals with angular momenta similar to atomic systems, even when the circular symmetry is broken. Unfortunately, the predicted effects have not yet been measured. It therefore remains an open question whether it is possible to reduce the noise in the STM signal enough to observe the predicted signatures in the difference spectra.

Artificial electron lattices made with an STM thus offer many possibilities to simulate quantum systems, and there are many more to be discovered. However, there are also intrinsic shortcomings. For example, in the CO on Cu(111) system, there is a relatively large broadening compared to the available energy scale and the construction method is not suitable for a larger scale. One possible solution is to create a potential pattern in thin semiconductor films on top of two-dimensional quantum wells using lithography [12–14]. These systems have a much smaller broadening and the production can more easily be scaled up. Additionally, a measurable spin-orbit coupling has been predicted for such a system [124]. The challenge for the future is to achieve the same control and precision in these semiconductor films on quantum wells as is now available for artificial electron lattices made with an STM.

Bibliography

- [1] A. K. Geim & K. S. Novoselov, “The rise of graphene”, *Nature Materials*, vol. 6, 2007, pp. 183–191.
- [2] C. L. Kane & E. J. Mele, “Quantum spin Hall effect in graphene”, *Physical Review Letters*, vol. 95, no. 22, 2005, p. 226801.
- [3] J. Sichau, M. Prada, T. Anlauf, T. J. Lyon, B. Bosnjak, L. Tiemann & R. H. Blick, “Resonance microwave measurements of an intrinsic spin-orbit coupling gap in graphene: A possible indication of a topological state”, *Physical Review Letters*, vol. 122, no. 4, 2019, p. 046403.
- [4] K. Hatsuda, H. Mine, T. Nakamura, J. Li, R. Wu, S. Katsumoto & J. Haruyama, “Evidence for a quantum spin Hall phase in graphene decorated with Bi₂Te₃ nanoparticles”, *Science Advances*, vol. 4, no. 11, 2018.
- [5] C. Weeks, J. Hu, J. Alicea, M. Franz & R. Wu, “Engineering a robust quantum spin Hall state in graphene via adatom deposition”, *Physical Review X*, vol. 1, no. 2, 2011, p. 021001.
- [6] C. Cao & J.-H. Chen, “Quantum Spin Hall Materials”, *Advanced Quantum Technologies*, vol. 2, no. 10, 2019, p. 1900026.
- [7] I. Bloch, J. Dalibard & S. Nascimbene, “Quantum simulations with ultracold quantum gases”, *Nature Physics*, vol. 8, no. 4, 2012, pp. 267–276.
- [8] A. Aspuru-Guzik & P. Walther, “Photonic quantum simulators”, *Nature Physics*, vol. 8, no. 4, 2012, pp. 285–291.
- [9] Y. Chu, P. Kharel, W. H. Renninger, L. D. Burkhardt, L. Frunzio, P. T. Rakich & R. J. Schoelkopf, “Quantum acoustics with superconducting qubits”, *Science*, vol. 358, no. 6360, 2017, pp. 199–202.
- [10] L. Kouwenhoven & C. Marcus, “Quantum dots”, *Physics World*, vol. 11, no. 6, 1998, p. 35.
- [11] C. Volk, A.-M. J. Zwerver, U. Mukhopadhyay, P. T. Eendebak, C. J. van Diepen, J. P. Dehollain, T. Hensgens, T. Fujita, C. Reichl, W. Wegscheider, et al., “Loading a quantum-dot based “Qubyte” register”, *npj Quantum Information*, vol. 5, no. 1, 2019, pp. 1–8.
- [12] N. A. Franchina Vergel, L. C. Post, D. Sciacca, M. Berthe, F. Vaurette, Y. Lambert, D. Yarekha, D. Troadec, C. Coinon, G. Fleury, et al., “Engineering a Robust Flat Band in III–V Semiconductor Heterostructures”, *Nano Letters*, 2020.
- [13] M. Gibertini, A. Singha, V. Pellegrini, M. Polini, G. Vignale, A. Pinczuk, L. N. Pfeiffer & K. W. West, “Engineering artificial graphene in a two-dimensional electron gas”, *Physical Review B*, vol. 79, no. 24, 2009, p. 241406.

- [14] S. Wang, D. Scarabelli, L. Du, Y. Y. Kuznetsova, L. N. Pfeiffer, K. W. West, G. C. Gardner, M. J. Manfra, V. Pellegrini, S. J. Wind, et al., “Observation of Dirac bands in artificial graphene in small-period nanopatterned GaAs quantum wells”, *Nature Nanotechnology*, vol. 13, no. 1, 2018, pp. 29–33.
- [15] K. K. Gomes, W. Mar, W. Ko, F. Guinea & H. C. Manoharan, “Designer Dirac fermions and topological phases in molecular graphene”, *Nature*, vol. 483, no. 7389, 2012, pp. 306–310.
- [16] R. Drost, T. Ojanen, A. Harju & P. Liljeroth, “Topological states in engineered atomic lattices”, *Nature Physics*, vol. 13, no. 7, 2017, p. 668.
- [17] S. R. Schofield, P. Studer, C. F. Hirjibehedin, N. J. Curson, G. Aeppli & D. R. Bowler, “Quantum engineering at the silicon surface using dangling bonds”, *Nature Communications*, vol. 4, no. 1, 2013, pp. 1–7.
- [18] M. R. Slot, T. S. Gardenier, P. H. Jacobse, G. C. P. van Miert, S. N. Kempkes, S. J. M. Zevenhuizen, C. M. Smith, D. Vanmaekelbergh & I. Swart, “Experimental realization and characterization of an electronic Lieb lattice”, *Nature Physics*, vol. 13, no. 7, 2017, pp. 672–676.
- [19] L. C. Collins, T. G. Witte, R. Silverman, D. B. Green & K. K. Gomes, “Imaging quasiperiodic electronic states in a synthetic Penrose tiling”, *Nature Communications*, vol. 8, 2017, p. 15961.
- [20] S. N. Kempkes, M. R. Slot, S. E. Freeney, S. J. M. Zevenhuizen, D. Vanmaekelbergh, I. Swart & C. M. Smith, “Design and characterization of electrons in a fractal geometry”, *Nature Physics*, vol. 15, no. 2, 2019, p. 127.
- [21] K. v. Klitzing, G. Dorda & M. Pepper, “New method for high-accuracy determination of the fine-structure constant based on quantized Hall resistance”, *Physical Review Letters*, vol. 45, no. 6, 1980, p. 494.
- [22] M. Freedman, A. Kitaev, M. Larsen & Z. Wang, “Topological quantum computation”, *Bulletin of the American Mathematical Society*, vol. 40, no. 1, 2003, pp. 31–38.
- [23] C. Nayak, S. H. Simon, A. Stern, M. Freedman & S. D. Sarma, “Non-Abelian anyons and topological quantum computation”, *Reviews of Modern Physics*, vol. 80, no. 3, 2008, p. 1083.
- [24] J. Cano, B. Bradlyn, Z. Wang, L. Elcoro, M. G. Vergniory, C. Felser, M. I. Aroyo & B. A. Bernevig, “Topology of disconnected elementary band representations”, *Physical Review Letters*, vol. 120, no. 26, 2018, p. 266401.
- [25] D.-S. Ma, Y. Xu, C. S. Chiu, N. Regnault, A. A. Houck, Z. Song & B. A. Bernevig, “Spin-orbit-induced topological flat bands in line and split graphs of bipartite lattices”, *Physical Review Letters*, vol. 125, no. 26, 2020, p. 266403.
- [26] Y. Cao, V. Fatemi, S. Fang, K. Watanabe, T. Taniguchi, E. Kaxiras & P. Jarillo-Herrero, “Unconventional superconductivity in magic-angle graphene superlattices”, *Nature*, vol. 556, no. 7699, 2018, pp. 43–50.
- [27] S. E. Freeney, J. J. van den Broeke, A. J. J. H. van der Veen, I. Swart & C. M. Smith, “Edge-dependent topology in Kekulé lattices”, *Physical Review Letters*, vol. 124, no. 23, 2020, p. 236404.
- [28] T. S. Gardenier, J. J. van den Broeke, J. R. Moes, I. Swart, C. Delerue, M. R. Slot, C. M. Smith & D. Vanmaekelbergh, “p Orbital flat band and Dirac cone

- in the electronic honeycomb lattice”, *ACS Nano*, vol. 14, no. 10, 2020, PMID: 32991147, pp. 13638–13644.
- [29] M. R. Slot, S. N. Kempkes, E. J. Knol, W. M. J. Van Weerdenburg, J. J. van den Broeke, D Wegner, D Vanmaekelbergh, A. A. Khajetoorians, C. M. Smith & I Swart, “p-Band engineering in artificial electronic lattices”, *Physical Review X*, vol. 9, no. 1, 2019, p. 011009.
- [30] J. van den Broeke, I Swart, C. M. Smith & D Vanmaekelbergh, “Spin-orbit gaps in the s and p orbital bands of an artificial honeycomb lattice”, *arXiv preprint arXiv:2104.06912*, 2021.
- [31] W. Shockley, “On the surface states associated with a periodic potential”, *Physical review*, vol. 56, no. 4, 1939, p. 317.
- [32] I. Tamm, “On the possible bound states of electrons on a crystal surface”, *Phys. Z. Sowjetunion*, vol. 1, 1932, pp. 733–735.
- [33] P. O. Gartland & B. J. Slagsvold, “Transitions conserving parallel momentum in photoemission from the (111) face of copper”, *Physical Review B*, vol. 12, no. 10, 1975, p. 4047.
- [34] J Kliever, R Berndt, E. V. Chulkov, V. M. Silkin, P. M. Echenique & S Crampin, “Dimensionality effects in the lifetime of surface states”, *Science*, vol. 288, no. 5470, 2000, pp. 1399–1402.
- [35] B. Voigtländer, *Scanning probe microscopy: Atomic force microscopy and scanning tunneling microscopy*, Springer, 2015.
- [36] G. Binnig, H. Rohrer, C. Gerber & E. Weibel, “Surface studies by scanning tunneling microscopy”, *Physical review letters*, vol. 49, no. 1, 1982, p. 57.
- [37] G. Binnig, H. Rohrer, C. Gerber & E. Weibel, “Tunneling through a controllable vacuum gap”, *Applied Physics Letters*, vol. 40, no. 2, 1982, pp. 178–180.
- [38] J. Bardeen, “Tunnelling from a many-particle point of view”, *Physical Review Letters*, vol. 6, no. 2, 1961, p. 57.
- [39] J. Tersoff & D. R. Hamann, “Theory and application for the scanning tunneling microscope”, *Physical review letters*, vol. 50, no. 25, 1983, p. 1998.
- [40] J. Tersoff & D. R. Hamann, “Theory of the scanning tunneling microscope”, *Physical Review B*, vol. 31, no. 2, 1985, p. 805.
- [41] N. Lang, “Spectroscopy of single atoms in the scanning tunneling microscope”, *Physical Review B*, vol. 34, no. 8, 1986, p. 5947.
- [42] D. M. Eigler & E. K. Schweizer, “Positioning single atoms with a scanning tunnelling microscope”, *Nature*, vol. 344, no. 6266, 1990, pp. 524–526.
- [43] I.-W. Lyo & P. Avouris, “Field-induced nanometer-to atomic-scale manipulation of silicon surfaces with the STM”, *Science*, vol. 253, no. 5016, 1991, pp. 173–176.
- [44] L Bartels, G Meyer & K. H. Rieder, “Basic steps of lateral manipulation of single atoms and diatomic clusters with a scanning tunneling microscope tip”, *Physical Review Letters*, vol. 79, no. 4, 1997, p. 697.
- [45] H. J. Mamin, P. H. Guethner & D Rugar, “Atomic emission from a gold scanning-tunneling-microscope tip”, *Physical review letters*, vol. 65, no. 19, 1990, p. 2418.

- [46] D. Huang, H. Uchida & M. Aono, “Deposition and subsequent removal of single Si atoms on the Si (111)- 7×7 surface by a scanning tunneling microscope”, *Journal of Vacuum Science & Technology B: Microelectronics and Nanometer Structures Processing, Measurement, and Phenomena*, vol. 12, no. 4, 1994, pp. 2429–2433.
- [47] S.-i. Ishi, Y. Ohno & B. Viswanathan, “An overview on the electronic and vibrational properties of adsorbed CO”, *Surface Science*, vol. 161, no. 2-3, 1985, pp. 349–372.
- [48] L. Bartels, G. Meyer & K.-H. Rieder, “The evolution of CO adsorption on Cu (111) as studied with bare and CO-functionalized scanning tunneling tips”, *Surface science*, vol. 432, no. 3, 1999, pp. L621–L626.
- [49] L. Bartels, G. Meyer & K. H. Rieder, “Controlled vertical manipulation of single CO molecules with the scanning tunneling microscope: A route to chemical contrast”, *Applied Physics Letters*, vol. 71, no. 2, 1997, pp. 213–215.
- [50] S. Fölsch, J. Martínez-Blanco, J. Yang, K. Kanisawa & S. C. Erwin, “Quantum dots with single-atom precision”, *Nature nanotechnology*, vol. 9, no. 7, 2014, p. 505.
- [51] O. Jeandupeux, L. Bürgi, A. Hirstein, H. Brune & K. Kern, “Thermal damping of quantum interference patterns of surface-state electrons”, *Physical Review B*, vol. 59, no. 24, 1999, p. 15926.
- [52] M. F. Crommie, C. P. Lutz & D. M. Eigler, “Confinement of electrons to quantum corrals on a metal surface”, *Science*, vol. 262, no. 5131, 1993, pp. 218–220.
- [53] S. E. Freney, S. T. P. Borman, J. W. Hartevelde & I. Swart, “Coupling quantum corrals to form artificial molecules”, *SciPost Physics*, vol. 9, 6 2020, p. 85.
- [54] E. B. Davies & L. Parns, “Trapped modes in acoustic waveguides”, *Q. J. Mech. Appl. Math.*, vol. 51, 1988, pp. 477–492.
- [55] C.-H. Park & S. G. Louie, “Making massless Dirac fermions from a patterned two-dimensional electron gas”, *Nano Letters*, vol. 9, no. 5, 2009, pp. 1793–1797.
- [56] W. E. Arnoldi, “The principle of minimized iterations in the solution of the matrix eigenvalue problem”, *Quarterly of applied mathematics*, vol. 9, no. 1, 1951, pp. 17–29.
- [57] C. Lanczos, “An iteration method for the solution of the eigenvalue problem of linear differential and integral operators”, *Journal of Research of the National Bureau of Standards*, vol. 45, no. 4, 1950, pp. 255–282.
- [58] I. U. Ojalvo & M. Newman, “Vibration modes of large structures by an automatic matrix-reduction method”, *AIAA Journal*, vol. 8, no. 7, 1970, pp. 1234–1239.
- [59] W. R. Inc., *Mathematica, Version 11.2*, Champaign, IL, 2017.
- [60] P. Virtanen, R. Gommers, T. E. Oliphant, M. Haberland, T. Reddy, D. Cournapeau, E. Burovski, P. Peterson, W. Weckesser, J. Bright, S. J. van der Walt, M. Brett, J. Wilson, K. J. Millman, N. Mayorov, A. R. J. Nelson, E. Jones, R. Kern, E. Larson, C. J. Carey, bibinitperiodI. Polat, Y. Feng, E. W. Moore, J. VanderPlas, D. Laxalde, J. Perktold, R. Cimrman, I. Henriksen, E. A. Quintero, C. R. Harris, A. M. Archibald,

- A. H. Ribeiro, F. Pedregosa, P. van Mulbregt & SciPy 1.0 Contributors, “SciPy 1.0: Fundamental Algorithms for Scientific Computing in Python”, *Nature Methods*, vol. 17, 2020, pp. 261–272.
- [61] S. Li, W.-X. Qiu & J.-H. Gao, “Designing artificial two dimensional electron lattice on metal surface: a Kagome-like lattice as an example”, *Nanoscale*, vol. 8, no. 25, 2016, pp. 12747–12754.
- [62] J. C. Slater & G. F. Koster, “Simplified LCAO method for the periodic potential problem”, *Physical Review*, vol. 94, no. 6, 1954, p. 1498.
- [63] J. K. Asbóth, L. Oroszlány & A. Pályi, “A short course on topological insulators”, *Lecture notes in physics*, vol. 919, 2016, pp. 997–1000.
- [64] A. Y. Kitaev, “Unpaired Majorana fermions in quantum wires”, *Physics-Uspekhi*, vol. 44, no. 10S, 2001, p. 131.
- [65] S. Frolov, *Quantum computing’s reproducibility crisis: Majorana fermions*, 2021.
- [66] S. Schlamminger & D. Haddad, “The Kibble balance and the kilogram”, *Comptes Rendus Physique*, vol. 20, no. 1-2, 2019, pp. 55–63.
- [67] H. A. Kramers, “Théorie générale de la rotation paramagnétique dans les cristaux”, *Proc. Acad. Amst.*, vol. 33, no. 6, 1930.
- [68] B. A. Bernevig, T. L. Hughes & S.-C. Zhang, “Quantum spin Hall effect and topological phase transition in HgTe quantum wells”, *Science*, vol. 314, no. 5806, 2006, pp. 1757–1761.
- [69] M. König, S. Wiedmann, C. Brüne, A. Roth, H. Buhmann, L. W. Molenkamp, X.-L. Qi & S.-C. Zhang, “Quantum spin Hall insulator state in HgTe quantum wells”, *Science*, vol. 318, no. 5851, 2007, pp. 766–770.
- [70] W. Beugeling, E. Kalesaki, C. Delerue, Y.-M. Niquet, D. Vanmaekelbergh & C. M. Smith, “Topological states in multi-orbital HgTe honeycomb lattices”, *Nature Communications*, vol. 6, no. 1, 2015, pp. 1–7.
- [71] E. Kalesaki, C. Delerue, C. M. Smith, W. Beugeling, G. Allan & D. Vanmaekelbergh, “Dirac cones, topological edge states, and nontrivial flat bands in two-dimensional semiconductors with a honeycomb nanogeometry”, *Physical Review X*, vol. 4, no. 1, 2014, p. 011010.
- [72] W. P. Su, J. R. Schrieffer & A. J. Heeger, “Solitons in polyacetylene”, *Physical Review Letters*, vol. 42, no. 25, 1979, p. 1698.
- [73] O. Klein, “Elektrodynamik und wellenmechanik vom standpunkt des korrespondenzprinzips”, *Zeitschrift für Physik A Hadrons and nuclei*, vol. 41, no. 6-7, 1927, pp. 407–442.
- [74] W. Gordon, “Der comptoneffekt nach der schrödingerschen theorie”, *Zeitschrift für Physik*, vol. 40, no. 1-2, 1926, pp. 117–133.
- [75] P. A. M. Dirac, “The quantum theory of the electron”, *Proceedings of the Royal Society of London. Series A, Containing Papers of a Mathematical and Physical Character*, vol. 117, no. 778, 1928, pp. 610–624.
- [76] W. Pauli, “Zur quantenmechanik des magnetischen elektrons”, in: *Wolfgang Pauli*, Springer, 1988, pp. 282–305.
- [77] G. van Miert, V. Juričić & C. M. Smith, “Tight-binding theory of spin-orbit coupling in graphynes”, *Physical Review B*, vol. 90, no. 19, 2014, p. 195414.

- [78] R. Cuadrado & J. I. Cerdá, “Fully relativistic pseudopotential formalism under an atomic orbital basis: Spin–orbit splittings and magnetic anisotropies”, *Journal of Physics: Condensed Matter*, vol. 24, no. 8, 2012, p. 086005.
- [79] K. Von Klitzing, “The quantized Hall effect”, *Reviews of Modern Physics*, vol. 58, no. 3, 1986, p. 519.
- [80] D. J. Thouless, M. Kohmoto, M. P. Nightingale & M. den Nijs, “Quantized Hall conductance in a two-dimensional periodic potential”, *Physical Review Letters*, vol. 49, no. 6, 1982, p. 405.
- [81] A. Altland & M. R. Zirnbauer, “Nonstandard symmetry classes in mesoscopic normal-superconducting hybrid structures”, *Physical Review B*, vol. 55, no. 2, 1997, p. 1142.
- [82] L. Fu, “Topological crystalline insulators”, *Physical Review Letters*, vol. 106, no. 10, 2011, p. 106802.
- [83] R.-J. Slager, A. Mesaros, V. Juričić & J. Zaanen, “The space group classification of topological band-insulators”, *Nature Physics*, vol. 9, no. 2, 2013, p. 98.
- [84] M. Nurul Huda, S. Kezilebieke & P. Liljeroth, “Designer flat bands in one-dimensional artificial systems”, *arXiv:2003.08234*, 2020.
- [85] J. Girovsky, J. L. Lado, F. E. Kalf, E. Fahrenfort, L. J. J. M. Peters, J. Fernández-Rossier & A. F. Otte, “Emergence of quasiparticle Bloch states in artificial crystals crafted atom-by-atom”, *SciPost Physics*, vol. 2, 3 2017, p. 020.
- [86] H. Kim, A. Palacio-Morales, T. Posske, L. Rózsa, K. Palotás, L. Szunyogh, M. Thorwart & R. Wiesendanger, “Toward tailoring Majorana bound states in artificially constructed magnetic atom chains on elemental superconductors”, *Science Advances*, vol. 4, no. 5, 2018, eaar5251.
- [87] A. Kamlapure, L. Cornils, J. Wiebe & R. Wiesendanger, “Engineering the spin couplings in atomically crafted spin chains on an elemental superconductor”, *Nature Communications*, vol. 9, no. 1, 2018, p. 3253.
- [88] S. N. Kempkes, M. R. Slot, J. J. van den Broeke, P. Capiod, W. A. Benalcazar, D. Vanmaekelbergh, D. Bercioux, I. Swart & C. M. Smith, “Robust zero-energy modes in an electronic higher-order topological insulator”, *Nature Materials*, vol. 18, no. 12, 2019, pp. 1292–1297.
- [89] T. Kariyado & X. Hu, “Topological states characterized by mirror winding numbers in graphene with bond modulation”, *Scientific Reports*, vol. 7, no. 1, 2017, p. 16515.
- [90] J. Noh, W. A. Benalcazar, S. Huang, M. J. Collins, K. P. Chen, T. L. Hughes & M. C. Rechtsman, “Topological protection of photonic mid-gap defect modes”, *Nature Photonics*, vol. 12, no. 7, 2018, p. 408.
- [91] L.-H. Wu & X. Hu, “Topological properties of electrons in honeycomb lattice with detuned hopping energy”, *Scientific reports*, vol. 6, 2016, pp. 24347–24347.
- [92] K. Nakada, M. Fujita, G. Dresselhaus & M. S. Dresselhaus, “Edge state in graphene ribbons: Nanometer size effect and edge shape dependence”, *Physical Review B*, vol. 54, no. 24, 1996, p. 17954.

- [93] M. Fujita, K. Wakabayashi, K. Nakada & K. Kusakabe, “Peculiar localized state at zigzag graphite edge”, *J. Phys. Soc. Jpn*, vol. 65, no. 7, 1996, pp. 1920–1923.
- [94] D. Nečas & P. Klapeťek, “Gwyddion: an open-source software for SPM data analysis”, *Open Physics*, vol. 10, no. 1, 2012, pp. 181–188.
- [95] B. Bradlyn, L. Elcoro, J. Cano, M. G. Vergniory, Z. Wang, C. Felser, M. I. Aroyo & B. A. Bernevig, “Topological quantum chemistry”, *Nature*, vol. 547, no. 7663, 2017, pp. 298–305.
- [96] B. Keimer & J. E. Moore, “The physics of quantum materials”, *Nature Physics*, vol. 13, no. 11, 2017, pp. 1045–1055.
- [97] A. H. Castro Neto, F. Guinea, N. M. R. Peres, K. S. Novoselov & A. K. Geim, “The electronic properties of graphene”, *Reviews of Modern Physics*, vol. 81, no. 1, 2009, pp. 109–162.
- [98] W.-X. Qiu, L. Ma, J.-T. Lü & J.-H. Gao, “Making artificial px,y orbital honeycomb electron lattice on metal surface”, *Arxiv*, 2019, pp. 1–10.
- [99] C. Wu, D. Bergman, L. Balents & S. D. Sarma, “Flat bands and Wigner crystallization in the honeycomb optical lattice”, *Physical Review Letters*, vol. 99, no. 7, 2007, p. 070401.
- [100] F. Reis, G. Li, L. Dudy, M. Bauernfeind, S. Glass, W. Hanke, R. Thomale, J. Schäfer & R. Claessen, “Bismuthene on a SiC substrate: A candidate for a high-temperature quantum spin Hall material”, *Science*, vol. 357, no. 6348, 2017, pp. 287–290.
- [101] C. Wu & S. D. Sarma, “p x, y-orbital counterpart of graphene: Cold atoms in the honeycomb optical lattice”, *Physical Review B*, vol. 77, no. 23, 2008, p. 235107.
- [102] C. Wu, W. V. Liu, J. Moore & S. D. Sarma, “Quantum stripe ordering in optical lattices”, *Physical Review Letters*, vol. 97, no. 19, 2006, pp. 3–6.
- [103] T. Müller, S. Fölling, A. Widera & I. Bloch, “State preparation and dynamics of ultracold atoms in higher lattice orbitals”, *Physical Review Letters*, vol. 99, no. 20, 2007, pp. 1–4.
- [104] M. Ölschläger, T. Kock, G. Wirth, A. Ewerbeck, C. Morais Smith & A. Hemmerich, “Interaction-induced chiral px ± ipy superfluid order of bosons in an optical lattice”, *New Journal of Physics*, vol. 15, 2013.
- [105] G. Wirth, M. Ölschläger & A. Hemmerich, “Evidence for orbital superfluidity in the P-band of a bipartite optical square lattice”, *Nature Physics*, vol. 7, no. 2, 2011, pp. 147–153.
- [106] M. Milićević, T. Ozawa, G. Montambaux, I. Carusotto, E. Galopin, A. Lemaître, L. Le Gratiet, I. Sagnes, J. Bloch & A. Amo, “Orbital Edge States in a Photonic Honeycomb Lattice”, *Physical Review Letters*, vol. 118, no. 10, 2017, pp. 1–6.
- [107] T. Jacqmin, I. Carusotto, I. Sagnes, M. Abbarchi, D. D. Solnyshkov, G. Malpuech, E. Galopin, A. Lemaître, J. Bloch & A. Amo, “Direct observation of Dirac cones and a flatband in a honeycomb lattice for polaritons”, *Physical Review Letters*, vol. 112, no. 11, 2014, pp. 1–5.
- [108] S. Klemmt, T. H. Harder, O. A. Egorov, K. Winkler, R. Ge, M. A. Bandres, M. Emmerling, L. Worschech, T. C. H. Liew, M. Segev, C. Schneider & S.

- Höfling, “Exciton-polariton topological insulator”, *Nature*, vol. 562, no. 7728, 2018, pp. 552–556.
- [109] J. Zeng, M. Lu, H. Liu, H. Jiang & X. C. Xie, “Degenerate p orbitals flat band model and realization in two-dimensional materials”, *Arxiv*, 2020, pp. 1–5.
- [110] Y. Cao, V. Fatemi, A. Demir, S. Fang, S. L. Tomarken, J. Y. Luo, J. D. Sanchez-Yamagishi, K. Watanabe, T. Taniguchi, E. Kaxiras, R. C. Ashoori & P. Jarillo-Herrero, “Correlated insulator behaviour at half-filling in magic-angle graphene superlattices”, *Nature*, vol. 556, no. 7699, 2018, pp. 80–84.
- [111] A. K. Singh, E. S. Penev & B. I. Yakobson, “Vacancy clusters in graphane as quantum dots”, *ACS Nano*, vol. 4, no. 6, 2010, pp. 3510–3514.
- [112] M. Gibertini, A. Singha, V. Pellegrini, M. Polini, G. Vignale, A. Pinczuk, L. N. Pfeiffer & K. W. West, “Engineering artificial graphene in a two-dimensional electron gas”, *Physical Review B*, vol. 79, no. 24, 2009, pp. 8–11.
- [113] A. Singha, M. Gibertini, B. Karmakar, S. Yuan, M. Polini, G. Vignale, M. I. Katsnelson, A. Pinczuk, L. N. Pfeiffer, K. W. West & V. Pellegrini, “Two-dimensional Mott-Hubbard electrons in an artificial honeycomb lattice”, *Science*, vol. 332, no. 6034, 2011, pp. 1176–1179.
- [114] L. C. Post, T Xu, N. A. F. Vergel, A Tadjine, Y Lambert, F Vaurette, D Yarekha, L Desplanque, D Stiévenard, X Wallart, et al., “Triangular nanoporation and band engineering of InGaAs quantum wells: a lithographic route toward Dirac cones in III–V semiconductors”, *Nanotechnology*, vol. 30, no. 15, 2019, p. 155301.
- [115] M. P. Boneschanscher, W. H. Evers, J. J. Geuchies, T. Altantzis, B. Goris, F. T. Rabouw, S. A. P. Van Rossum, H. S. J. Van Der Zant, L. D. A. Siebbeles, G. Van Tendeloo, I. Swart, J. Hilhorst, A. V. Petukhov, S. Bals & D. Vanmaekelbergh, “Long-range orientation and atomic attachment of nanocrystals in 2D honeycomb superlattices”, *Science*, vol. 344, no. 6190, 2014, pp. 1377–1380.
- [116] M. Alimoradi Jazi, V. A. E. C. Janssen, W. H. Evers, A. Tadjine, C. Delerue, L. D. A. Siebbeles, H. S. J. Van Der Zant, A. J. Houtepen & D. Vanmaekelbergh, “Transport Properties of a Two-Dimensional PbSe Square Superstructure in an Electrolyte-Gated Transistor”, *Nano Letters*, vol. 17, no. 9, 2017, pp. 5238–5243.
- [117] S. Rachel, “Interacting topological insulators: A review”, *Reports on Progress in Physics*, vol. 81, no. 11, 2018.
- [118] M. Laubach, J. Reuther, R. Thomale & S. Rachel, “Rashba spin-orbit coupling in the Kane-Mele-Hubbard model”, *Physical Review B*, vol. 90, no. 16, 2014, pp. 1–13.
- [119] A. Bermudez, N. Goldman, A. Kubasiak, M. Lewenstein & M. A. Martin-Delgado, “Topological phase transitions in the non-Abelian honeycomb lattice”, *New Journal of Physics*, vol. 12, 2010.
- [120] R. G. Musket, W Mclean, A Colmenares, D. M. Makowiecki & W. J. Siekhaus, “Preparation of Atomically Clean Surfaces of Selected Elements: A Review”, *Applications of Surface Science*, vol. 10, 1982, pp. 143–207.

- [121] “Invited article: Autonomous assembly of atomically perfect nanostructures using a scanning tunneling microscope”, *Review of Scientific Instruments*, vol. 85, no. 12, 2014.
- [122] P. R. Wallace, “The Band Theory of Graphite”, *Physical Review*, vol. 71, no. 9, 1947, pp. 622–634.
- [123] L. Kou, Y. Ma, Z. Sun, T. Heine & C. Chen, “Two-dimensional topological insulators: Progress and prospects”, *The Journal of Physical Chemistry Letters*, vol. 8, no. 8, 2017, pp. 1905–1919.
- [124] H. D. Scammell & O. P. Sushkov, “Tuning the topological insulator states of artificial graphene”, *Physical Review B*, vol. 99, no. 8, 2019, p. 085419.
- [125] P. Ghaemi, S. Gopalakrishnan & T. L. Hughes, “Designer quantum spin Hall phase transition in molecular graphene”, *Physical Review B*, vol. 86, no. 20, 2012, p. 201406.
- [126] L. W. Molenkamp, G. Schmidt & G. E. W. Bauer, “Rashba Hamiltonian and electron transport”, *Physical Review B*, vol. 64, no. 12, 2001, p. 121202.
- [127] L. Lenz & D. Bercioux, “Dirac-Weyl electrons in a periodic spin-orbit potential”, *EPL*, vol. 96, no. 2, 2011, p. 27006.
- [128] M. Hoesch, M Muntwiler, V. N. Petrov, M Hengsberger, L Patthey, M Shi, M Falub, T Greber & J Osterwalder, “Spin structure of the Shockley surface state on Au (111)”, *Physical Review B*, vol. 69, no. 24, 2004, p. 241401.
- [129] P. Atkins, J. De Paula & J. Keeler, *Physical Chemistry*, Oxford University Press, UK, 2018.
- [130] R. van Gelderen & C. M. Smith, “Rashba and intrinsic spin-orbit interactions in biased bilayer graphene”, *Physical Review B*, vol. 81, no. 12, 2010, p. 125435.
- [131] M. Zarea & N. Sandler, “Rashba spin-orbit interaction in graphene and zigzag nanoribbons”, *Physical Review B*, vol. 79, no. 16, 2009, p. 165442.
- [132] H. C. Manoharan, C. P. Lutz & D. M. Eigler, “Quantum mirages formed by coherent projection of electronic structure”, *Nature*, vol. 403, no. 6769, 2000, pp. 512–515.
- [133] A. J. Heinrich, “Molecule Cascades”, *Science*, vol. 298, no. 5597, 2002, pp. 1381–1387.
- [134] S. Crampin & O. Bryant, “Fully three-dimensional scattering calculations of standing electron waves in quantum nanostructures: The importance of quasiparticle interactions”, *Physical Review B*, vol. 54, no. 24, 1996, R17367–R17370.
- [135] J. Kliewer, R. Berndt & S. Crampin, “Scanning tunnelling spectroscopy of electron resonators”, *New Journal of Physics*, vol. 3, no. 111, 2001.
- [136] R. X. Cao, B. F. Miao, Z. F. Zhong, L. Sun, B. You, W. Zhang, D. Wu, A. Hu, S. D. Bader & H. F. Ding, “Two-dimensional quantum diffusion of Gd adatoms in nano-size Fe corrals”, *Physical Review B*, vol. 87, no. 8, 2013, pp. 1–5.
- [137] R. W. Robinett, “Visualizing the solutions for the circular infinite well in quantum and classical mechanics”, *American Journal of Physics*, vol. 64, no. 4, 1996, pp. 440–446.

Samenvatting

Materiaalwetenschap bestudeert de eigenschappen van materialen en heeft tot doel nieuwe materialen te creëren met specifieke kenmerken die technologische uitdagingen kunnen overwinnen. Hoewel veel van deze natuurlijke materialen al buitengewoon nuttige eigenschappen hebben, zijn ze vaak niet ideaal voor een specifieke applicatie. Een beroemd voorbeeld is grafeen, dat een uitstekende materiaalsterkte heeft en elektronische geleiding vertoont die kan worden beschreven met 'massaloze' relativistische elektronen [1]. Grafeen heeft een tweedimensionaal honingraadrooster; intrinsieke spin-baankoppeling kan, in principe, een topologische bandopening creëren met daarin een spin-gepolariseerd kwantumkanaal aan de rand van het kristal. De intrinsieke spin-baankoppeling in grafeen is echter te klein om dit gewilde effect waar te nemen [2, 3]. Hoewel er veel pogingen zijn gedaan om de intrinsieke spin-baankoppeling in grafeen te verbeteren, zoals door het toevoegen van zware atomen [4, 5], zijn de resultaten tot op heden niet overtuigend [6].

Een alternatieve methode om systemen te ontwerpen die aan de gewenste eisen voldoen, is het bouwen van een kunstmatig rooster ofwel een kwantumsimulator. In dit geval worden atoomachtige bouwstenen zo gepositioneerd en met hoge precisie verbonden dat een rooster met de gewenste eigenschappen wordt verkregen. Dit kan op verschillende manieren worden bereikt, zoals door middel van koude atoomsystemen [7], fotonische systemen [8] en akoestische systemen [9], elk met hun eigen voor- en nadelen. Echter al deze systemen zijn niet gebaseerd op elektronische excitatie, en simuleren daarom alleen indirect elektronische materialen.

Kunstmatige elektronenroosters

Een manier om een kunstmatig-elektronenrooster te simuleren is door kunstmatige roosters te creëren die elektronen opsluiten. Dit kan bijvoorbeeld worden bereikt door kwantum-stippen [10, 11] te koppelen. Als alternatief kan men een potentiaalpatroon creëren in dunne halfgeleiderfilms bovenop tweedimensionale kwantumputten met behulp van lithografie [12–14]. Hoewel beide methoden veelbelovende resultaten hebben opgeleverd en de potentie hebben voor productie op grote schaal, zijn ze nog niet erg reproduceerbaar en nauwkeurig. Dat is een serieuze tekortkoming want ontwerpen en meten met grote nauwkeurigheid is essentieel om de mogelijkheden van deze kunstmatige elektronische systemen op een overtuigende manier te laten zien.

Meer precieze kunstmatige elektronenroosters kunnen worden gemaakt met een

rastertunnelmicroscop. Deze microscoop kan atomen en moleculen op een metaal oppervalk met atomaire precisie positioneren, en de resulterende elektronendichtheid van het gecreëerde kwantumobject meten. De atomen of moleculen stoten ofwel elektronen in een tweedimensionaal elektronengas af, of trekken ze aan. In beide gevallen worden de "vrijeëlektronen" gevangen in een tweedimensionaal rooster, waarvan de geometrie naar wens kan worden aangepast. Deze methode is ontwikkeld door Gomes et al. in 2012 [15], met behulp van CO-moleculen op een Cu(111)-oppervlak. Het Cu(111)-oppervlak bevat een effectief tweedimensionaal elektronengas, waarop de CO moleculen als verstrooiende elementen in een driehoekig patroon worden geplaatst. Omdat de elektronen worden afgestoten door de CO moleculen, worden deze opgesloten in een honingraatgeometrie, zoals in grafen. Later is gedemonstreerd dat kunstmatige elektronenroosters ook gemaakt kunnen worden op andere materiaalplatformen, zoals lege plekken in een enkele laag chloor bovenop Cu(100) [16], en bungelende bindingen op een H-Si(100) oppervlak [17]. Het CO op Cu(111)-platform is na Gomes et al. gebruikt om vierkante geometrieën [18], quasi-kristalstructuren [19] en fractale systemen [20] in kunstmatige elektronenroosters te onderzoeken.

Muffinvormbenadering

Om kunstmatige elektronenroosters te modelleren wordt het potentiaal landschap $V(x, y, z)$, dus de onderscheidende term in de Schrödinger eigenwaarde vergelijking voor de energie, als een muffinvorm gemodelleerd. De uitkomsten van de Schrödinger vergelijking kunnen op deze manier de experimentele uitkomsten met de rastertunnelmicroscop erg goed voorspellen. De muffinvorm benadering is dus een uitermate handig hulpmiddel voor het ontwerpen en begrijpen van kunstmatige elektronen roosters. In het geval van roosters gemaakt van CO op Cu(111) wordt het kunstmatige rooster beschreven als een tweedimensionaal elektronengas met een muffinvorm potentiaal gevormd door de met de rastertunnelmicroscop gepositioneerde (CO) moleculen. De CO moleculen worden gemodelleerd als schijfvormige potentiaal plateaus. Dit geeft een potentiaallandschap dat ongeveer dezelfde vorm heeft als een omgekeerde muffinvorm (zie Figuur 1), wat zijn naam leent aan deze benadering.

Topologie en magneetvelden

In dit proefschrift proberen we het scala aan mogelijkheden voor kunstmatige elektronenroosters uit te breiden en onderzoeken we (kristal)topologie, platte banden en magnetische velden in kunstmatige roosters die gecreëerd zijn met atomistische manipulatie.

Niet-triviale topologie kan buitengewoon nuttig zijn, omdat het unieke kwantumkanalen aan de rand van het kristal biedt die door de symmetrie van het systeem worden beschermd. Dit heeft geleid tot voorstellen om topologische materialen te gebruiken voor de ontwikkeling van kwantumcomputers [22, 23]. Bovendien kan een topologische bandopening leiden tot het ontstaan van geïsoleerde topologische



Figuur 1: De omgekeerde muffinvorm van de auteur van dit proefschrift.

vlakke banden [24]. Geïsoleerde platte banden zijn over het algemeen een interessant fenomeen, omdat de kinetische energie wordt uitgedoofd, waardoor interactie-effecten de dominante bijdrage leveren. Geïsoleerde topologische vlakke banden hebben de potentie voor nieuwe natuurkunde en toepassingen vanwege het niet-lokale karakter van de topologie [25]. Daarbij is voorspeld dat een geïsoleerde platte band de drijvende factor is achter onconventionele supergeleiding, bijvoorbeeld de fascinerende verschijning van supergeleiding in magische hoek gedraaid dubbellaagsgrafeen [25, 26].

Magnetische velden doorbreken de tijdsomkeersymmetrie van een systeem en kunnen aanleiding geven tot interessante (topologische) faseovergangen, zoals in het kwantum-Hall-effect [21]. Tot nu toe zijn magnetische velden alleen indirect bestudeerd in kunstmatige roosters, door magnetische effecten te simuleren met roostervervormingen [15]. Dus, door tijdsomkering gebroken systemen zijn nog niet toegankelijk in kunstmatige roosters, waardoor het onmogelijk is om de topologie van het kwantum-Hall-effect in deze systemen direct te bestuderen.

Opbouw van het proefschrift

Dit proefschrift is als volgt opgebouwd: in **hoofdstuk 2** presenteren we de theoretische en experimentele concepten die ten grondslag liggen aan het werk dat in dit proefschrift wordt gepresenteerd. We beginnen met de beschrijving van kunstmatige roosters, hoe ze worden gemaakt, en hoe de elektronische eigenschappen van deze systemen kunnen worden gemeten. Vervolgens onderzoeken we een aantal interessante roosterkenmerken, zoals interne vrijheidsgraden en topologie. Ten slotte bespreken we hoe spin-baankoppeling kan worden ingevoerd in de Schrödinger-vergelijking door de niet-relativistische limiet van de Dirac-vergelijking te nemen.

Hoofdstuk 3 bestudeert kristaltopologie aan de hand van het Kekulé-rooster. Het Kekulé-rooster is een variatie op het honingraatrooster met twee verschillende sterk-

tes van bindingen, een binnen de zeshoeken en een tussen de naastgelegen zeshoeken. Voor dit rooster is voorspeld dat het randtoestanden heeft die worden beschermd door kristaltopologie, en afhankelijk zijn van de precieze randvoorwaarden van het rooster. We creëren vier kunstmatige roosters, met verschillende verhoudingen tussen de twee soorten bindingen en verschillende randvoorwaarden. Hiermee verkennen we het topologische fasediagram van het Kekulé-rooster. Experimenteel observeren we inderdaad gelokaliseerde randmodi voor de niet-triviale roosters. Dit is in overeenkomst met resultaten die we vinden met muffinvorm en sterk bindende modellen voor het systeem.

Hoofdstuk 4 onderzoekt de honingraatgeometrie in kunstmatige roosters. Tot nu toe zijn in deze systemen alleen de s -orbitaal banden, de banden met de laagste energie, onderzocht. We laten zien dat door de grootte de eenheidscel van het rooster te veranderen, door de CO moleculen verder uit elkaar te plaatsen, de hoger energetische p -orbitalen van het systeem in het waarneembare bereik van het CO op Cu(111)-systeem kunnen worden gebracht. Bovendien laten we zien dat door het introduceren van clusters van CO-verstrooiers in plaats van enkele moleculen, de bindingen in het systeem kunnen worden gemanipuleerd. Op deze manier verkrijgen we een systeem met gescheiden s en p banden en een vlakke band gevormd door p orbitalen. Deze unieke bandenstructuur verschilt van die van grafen en was al eerder voorspeld voor optische en roosters met koude atomen [99].

Hoofdstuk 5 neemt spin-baankoppeling op in het muffinvorm raamwerk, en onderzoekt hoe dit de bandenstructuur van het kunstmatige honingraatrooster beïnvloedt. Spin-baankoppeling is een relativistisch effect en koppelt het magnetische moment van de elektronenspin aan het magnetische moment gegenereerd door de beweging van het elektron. We gebruiken een heuristisch model om het effect van de spin-baankoppeling te integreren in muffinvormbenaderingen. Met behulp van deze methode vinden we dat intrinsieke spin-baankoppeling een kloof opent in de bandenstructuur voor zowel de s - als de p -orbitalen. Rashba spin-baankoppeling, ten gevolge van de potentiaalverandering in der richting loodrecht op het tweedimensionale systeem, kan deze bandopeningen weer sluiten, in het bijzonder voor s -orbitaal systemen. De bandkloven zijn echter veel groter en beter bestand tegen Rashba spin-baankoppeling voor de p -orbitale banden. Als we deze bandopening verder onderzoeken in het niet-periodieke rooster, vinden we in de kloof rand-gelokaliseerde toestanden, wat wijst op een kwantumspin-Hall-toestand.

Hoofdstuk 6, tot slot, onderzoekt theoretisch de invloed van magnetische velden op kwantumkralen. Kwantumkralen zijn geïsoleerde tweedimensionale kunstmatige atomen, uitermate geschikt als eerste testobject. We voorspellen dat zelfs voor een niet-spin-gepolariseerde rastertunnelmicroscopie-punt, de effecten van spin-magneetveld koppeling op de kwantumkraaltoestanden zichtbaar zouden moeten zijn. Bovendien concluderen we dat het magnetische veld koppelt aan het impulsmoment van de circulaire kwantumkraal-oplossingen. Verrassend genoeg is een soortgelijk effect ook zichtbaar voor vierkante kwantumkralen. Dit is bijzonder, omdat vierkante kwantumkralen door de gebroken circulaire symmetrie geen goed gedefiniëerd impuls-

moment hebben. De ontdekking dat vierkante kwantumkralen een effectief impuls-moment hebben is belangrijk voor kunstmatige roosters in het algemeen, omdat in deze systemen de circulaire symmetrie van individuele roosterpunten niet behouden is.

Tot slot

We hebben in dit proefschrift verschillende mogelijkheden onderzocht voor met een rastertunnelmicroscop gemaakte kunstmatige elektronenroosters. We vonden door middel van het Kekulé-rooster dat het mogelijk is om kristaltopologie te introduceren in deze systemen. In het honingraatrooster ontdekten we dat het mogelijk is om geïsoleerde p -orbitaal banden en vlakke banden gevormd door deze orbitalen te meten. Vervolgens vonden we met muffinvorm simulaties dat in deze p -banden het effect van intrinsieke spin-baankoppeling relatief groot is, wat leidt tot meer robuustheid van door spin-baan gevormde bandopeningen tegen Rashba-koppeling. Tot slot voorspelden we dat in zowel vierkante als ronde kwantumkralen de koppeling tussen spin en (effectief)impulsmoment en een loodrecht magneetveld meetbaar is.

Met een rastertunnelmicroscop gemaakte kunstmatige elektronenroosters hebben dus vele mogelijkheden om kwantumsystemen te simuleren. Er zijn echter ook tekortkomingen, zo is er in het CO op Cu(111) systeem relatief veel verbreding ten opzichte van de beschikbare energieschaal en is de constructiemethode niet geschikt voor grotere schaal. Daarnaast is de spin-baankoppeling in koper dusdanig klein dat het niet mogelijk is om in dit systeem de effecten voorspeld in hoofdstuk 5 waar te nemen. Een mogelijke oplossing is om een potentiaalpatroon creëren in dunne halfgeleiderfilms bovenop tweedimensionale kwantumputten met behulp van lithografie [12–14]. In deze systemen is een kleinere verbreding aanwezig en de productie beter schaalbaar. Daarbij is voor een dergelijk systeem een meetbare spin-baankoppeling voorspeld [124]. De uitdaging voor de toekomst is om in deze halfgeleiderfilms op kwantumputten dezelfde controle en precisie te verkrijgen als nu beschikbaar is voor met een rastertunnelmicroscop gemaakte kunstmatige elektronenroosters.

List of publications

This thesis is based on the following publications:

- ♦ S. E. Freeney*, J. J. van den Broeke*, A. J. J. H. van der Veen, I Swart & C. Morais Smith, *Edge-dependent topology in Kekulé lattices*, **Physical Review Letters**, vol. 124, no. 23 (2020)
- ♦ M. R. Slot, S. N. Kempkes, E. J. Knol, W. M. J. Van Weerdenburg, J. J. van den Broeke, D. Wegner, D. Vanmaekelbergh, A. A. Khajetoorians, C. M. Smith & I. Swart, *p-Band engineering in artificial electronic lattices*, **Physical Review X**, vol. 9, no. 1 (2019)
- ♦ T. S. Gardenier*, J. J. van den Broeke*, J. R. Moes, I. Swart, C. Delerue, M. R. Slot, C. Morais Smith & D. Vanmaekelbergh, *P orbital flat band and Dirac cone in the electronic honeycomb lattice*, **ACS Nano**, vol. 14, no. 10 (2020)
- ♦ J. J. van den Broeke, I. Swart, C. Morais Smith & D. Vanmaekelbergh, *Spin-orbit gaps in the s and p orbital bands of an artificial honeycomb lattice*, **arXiv preprint**, arXiv:2104.06912 (2021)
- ♦ J. J. van den Broeke*, T. S. Gardenier*, R. A. M. Ligthart & I. Swart, *On the influence of electron spin in artificial lattices*, in preparation.

Other publications by the author:

- ♦ S. N. Kempkes, M. R. Slot, J. J. van den Broeke, P. Capiod, W. A. Benalcazar, D. Vanmaekelbergh, D. Bercioux, I. Swart & C. Morais Smith, *Robust zero-energy modes in an electronic higher-order topological insulator*, **Nature Materials**, vol. 18, no. 12 (2019)
- ♦ J. J. van den Broeke, S. N. Kempkes, A. Quelle & C. Morais Smith *Critical Behavior of Topological Kondo Insulators*, **arXiv preprint**, arXiv:1803.03553 (2020)
- ♦ R. van Damme, B. van der Meer, J. J. van den Broeke, F. Smalenburg & L. Filion, *Phase and vacancy behaviour of hard “slanted” cubes*, **The Journal of chemical physics**, vol. 147, no. 12 (2017)

*Both authors contributed equally

Acknowledgments

The last four years were challenging, and I was very lucky to not have to do it alone. In this section I would like to thank the people that I worked with and helped me along the way.

First of all, I would like to thank my supervisors. Cristiane, thank you for giving me the opportunity to do a PhD in your group. Daniël, thank you for your unshakable confidence in the spin-orbit project, your patient support and always being available for a chat. Ingmar, I really enjoyed the many discussions we had. Thank you for your practical advise and the warm welcome into Team Kelder.

Team Kelder was an awesome group to finish my research in. Even though the pandemic made it hard to keep connected, you guys kept me on track and made the experience much more enjoyable. Saoirse, thank you for the many fun discussions, games of table soccer and taking me to aerial acrobatics. Christiaan, your klaverjas enthusiasm was contagious. Rian, it was really nice to discuss the muffin-tin code with you and make it better together. Jan, although we never worked on the same project, you were always happy to share and explain what you were doing. Marlou, your enthusiasm for science and the people around you was amazing. Pierre, thank you for the discussions on DFT, I learned a lot. Thomas and Jesper, thank you for being my paranymphs and all your encouragement and support the last years, I had a lot of fun sharing an office with you. I would also like to thank the rest of the CMI for their welcoming attitude and the positive atmosphere. It was a pleasure working together. Also a big thank you to Christophe, Dario, Wladimir, Alex, Daniel, Elze, Werner and Jan Jurre it was great working with you. Next, I would like to thank the students I supervised. Mickey, Simon and August, thank you for your many questions and enthusiasm.

Adriana, we spent a lot of time together at the ITP. Thank you for always being there to listen and come up with ideas on how to tackle any challenge. I would also like to thank my other office mates at the ITP; Scott, Bram and Carlene thank you for the lovely time! I would also like to thank the rest of the ITP members, especially, Anton, Mariya, Sander Kooi, Sander Kempkes, Rodrigo, Ozela, Lars, Mikael, Sonja, Gerwin, Jurriaan, Dirk, Tycho, Joost, Peter and Laura. I learned a lot from you, both in the field of physics and outside of it.

Maartje thank you for the many conversations we had about science; how it is, how it should be, how it definitely should not be, and how to keep your mental sanity

intact throughout the confusing process it can become. Janneke, we have been on many adventures together, from Paris to Barcelona. The last years, our traveling together has become less, and our adventures are closer to home. However, our conversations have not become less interesting and I really enjoyed the many hikes we made together. Charlotte and Jonas, a lot has changed since we met during our master thesis. It was wonderful to see each other in Dresden, and I very much hope we will soon be able to talk offline again and meet Leonore. Kaj, Rick, Ivo and Aldo it was really awesome to have regular (digital) tea breaks together. It made me feel a lot less isolated during lockdown and somehow Bonn did not seem in a different country anymore. Harm, Julius, Kyla and Lukas, thank you for the awesome Christmas dinners. Hopefully we will be able to plan one again in real life this year. Elise, Annieka, Matthijs, Femmy, Christie, Joost, Marjolein, Michiel, Roos, Sanne, Valerie, Andrew, Evelien en Nienke thank you for the many on- and offline games and the awesome weekends we have had!

I would also like to thank my family, opa, oma's, Bartho, Michèlle, dad and mom. The last two years have been a rollercoaster and as I write this we are going through one of the hardest things we have ever done. Thank you very much for your support, I love you.

Finally, I would like to thank my fiancé Lis. The journey towards a PhD was not an easy one, and I was very lucky to have you by my side. Thank you very much for your never-ending enthusiasm on your quest to explain to everyone you meet what it is that I do my research on.

Curriculum Vitae

Jette Janine van den Broeke was born in Gouda on the 13th of December 1993. She attended atheneum at the Kandinsky college in Nijmegen, where she discovered her interest in science and graduated in 2012.

She then started a double bachelor program in physics and mathematics at Utrecht University. During her bachelor studies, she was the chairman of the SONS student union of the physics department and student representative in the department of physics board in 2014. After finishing both bachelor programs cum laude with a thesis on colloidal systems of hard 'tilted' cubes under supervision of Dr. Laura Filion, she continued her education with a master's program in theoretical physics in 2015.

While studying for her master's degree at Utrecht University, she was a teaching assistant for the courses 'mathematical techniques' and 'advanced classical mechanics' in the physics bachelor's program. She wrote her master thesis on thermodynamics of Kondo topological insulators under supervision of Prof. dr. Cristiane de Morais Smith and dr. Sander Kempkes, and finished her master's degree cum laude.

In 2017 she started her PhD research under supervision of Prof. dr. Cristiane de Morais Smith and Prof. dr. Daniel Vanmaekelbergh at Utrecht University that resulted in the work presented in this thesis. During her PhD research, she was a teaching assistant for the courses 'quantum nano world', 'quantum chemistry', twice for the course 'black hole physics' and supervised three bachelor students.

